

Hadronic vacuum polarization for the muon $g - 2$ from lattice QCD: Complete short and intermediate windows

Alexei Bazavov,¹ David A. Clarke,^{2,*} Christine T. H. Davies,³ Carleton DeTar,²
 Aida X. El-Khadra,^{4,5} Elvira Gámiz,⁶ Steven Gottlieb,⁷ Anthony V. Grebe,⁸
 Leon Hostetler,⁷ William I. Jay,⁹ Hwancheol Jeong,⁷ Andreas S. Kronfeld,⁸
 Shaun Lahert,^{2,†} Jack Laiho,¹⁰ G. Peter Lepage,¹¹ Michael Lynch,^{4,5} Andrew T. Lytle,^{4,5}
 Craig McNeile,¹² Ethan T. Neil,¹³ Curtis T. Peterson,¹ James N. Simone,⁸
 Jacob W. Sitison,^{13,‡} Ruth S. Van de Water,⁸ and Alejandro Vaquero^{2,14,15}

(Fermilab Lattice, HPQCD, and MILC Collaborations)

¹*Department of Computational Mathematics, Science and Engineering, and Department of Physics and Astronomy, Michigan State University, East Lansing, Michigan 48824, USA*

²*Department of Physics and Astronomy, University of Utah, Salt Lake City, UT 84112, USA*

³*SUPA, School of Physics and Astronomy, University of Glasgow, Glasgow, G12 8QQ, United Kingdom*

⁴*Department of Physics, University of Illinois, Urbana, Illinois, 61801, USA*

⁵*Illinois Center for Advanced Studies of the Universe, University of Illinois, Urbana, Illinois, 61801, USA*

⁶*CAFPE and Departamento de Física Teórica y del Cosmos, Universidad de Granada, E-18071 Granada, Spain*

⁷*Department of Physics, Indiana University, Bloomington, Indiana 47405, USA*

⁸*Theory Division, Fermi National Accelerator Laboratory, Batavia, Illinois, 60510, USA*

⁹*Department of Physics, Colorado State University, Fort Collins, CO 80523, USA*

¹⁰*Department of Physics, Syracuse University, NY 13244, USA*

¹¹*Laboratory for Elementary-Particle Physics, Cornell University, Ithaca, NY 14853, USA*

¹²*Centre for Mathematical Sciences, University of Plymouth, Plymouth PL4 8AA, United Kingdom*

¹³*Department of Physics, University of Colorado, Boulder, Colorado 80309, USA*

¹⁴*Departamento de Física Teórica, Universidad de Zaragoza, 50009 Zaragoza, Spain*

¹⁵*Center for Astroparticles and High Energy Physics (CAPA), Calle Pedro Cerbuna 12, 50009 Zaragoza, Spain*

(Dated: November 15, 2024)

arXiv:2411.09656v1 [hep-lat] 14 Nov 2024

Abstract

We present complete results for the hadronic vacuum polarization (HVP) contribution to the muon anomalous magnetic moment a_μ in the short- and intermediate-distance window regions, which account for roughly 10% and 35% of the total HVP contribution to a_μ , respectively. In particular, we perform lattice-QCD calculations for the isospin-symmetric connected and disconnected contributions, as well as corrections due to strong isospin-breaking. For the short-distance window observables, we investigate the so-called log-enhancement effects as well as the significant oscillations associated with staggered quarks in this region. For the dominant, isospin-symmetric light-quark connected contribution, we obtain $a_\mu^{ll,SD}(\text{conn.}) = 48.116(16)(94)[96] \times 10^{-10}$ and $a_\mu^{ll,W}(\text{conn.}) = 207.06(17)(63)[66] \times 10^{-10}$. We use Bayesian model averaging combined with a global bootstrap to fully estimate the covariance matrix between the individual contributions. Our determinations of the complete window contributions are $a_\mu^{SD} = 69.01(2)(21)[21] \times 10^{-10}$ and $a_\mu^W = 236.57(20)(94)[96] \times 10^{-10}$. This work is part of our ongoing effort to compute all contributions to HVP with an overall uncertainty at the few permille level.

* clarke.davida@gmail.com

† shaun.lahert@gmail.com

‡ jacob.sitison@colorado.edu

CONTENTS

I. Introduction	4
II. Background and Simulation Details	6
A. Definitions of window observables	6
B. Physical inputs	8
C. Lattice ensembles and correlation functions	10
III. Analysis Procedure	15
A. Blinding	15
B. Lattice corrections	16
C. Continuum extrapolations	17
D. Bayesian Model Averaging	18
IV. Window observables	20
A. Light-quark connected	20
B. Strange and charm	27
C. Disconnected	31
D. Strong-isospin breaking	34
1. Connected strong-isospin breaking	35
2. Disconnected strong-isospin breaking	42
E. Perturbative QCD estimates of short-distance observables	44
V. Results	49
A. Short-distance window observables	49
B. Intermediate-distance window observables	50
VI. Summary and outlook	53
Acknowledgments	56
A. Discretization effects at short-distances	57
B. Oscillating contributions in the short-distance window	60
C. Covariance and Bayesian model averaging	62
1. Statistical covariance	63
2. Systematic covariance	63
3. Correlation matrices	65
References	65

I. INTRODUCTION

The anomalous magnetic moment of the muon, $a_\mu \equiv (g - 2)_\mu/2$, provides one of the most precise tests of the Standard Model (SM) of particle physics. It has been measured to exquisite precision in a series of experiments, most recently at Fermilab by the Muon $g - 2$ Collaboration [1, 2], with the latest results reported at a precision of 200 parts per billion (ppb). Final results from the Fermilab experiment incorporating their complete data set are anticipated to improve the current precision by close to another factor of two [2]. In addition, the Muon $g-2$ /EDM experiment at J-PARC [3, 4] will further improve our experimental knowledge of this quantity.

Experimental measurements of a_μ have attracted particular interest because of their long-standing tension with Standard Model (SM) expectations, providing an enduring hint for the possibility that this quantity is influenced by new, as-yet unknown particles. The uncertainty on the SM prediction [5, 6] is dominated by contributions from Quantum Chromodynamics (QCD), namely hadronic vacuum polarization (HVP) and hadronic light-by-light scattering (HLbL). In this paper, we focus on HVP, which is the larger contribution to a_μ and the largest source of error in its SM prediction. There are two independent approaches, a data-driven one and lattice QCD. The former uses a dispersive framework together with experimental inputs, primarily taken from measurements of e^+e^- annihilation cross sections into hadronic channels. This approach was the basis of the SM prediction of Ref. [5]. However, a recent measurement by the CMD-3 collaboration [7] of the low-energy $e^+e^- \rightarrow \pi\pi$ cross section disagrees with all previous experimental results for this important channel, which accounts for roughly 75% of $a_\mu^{\text{HVP,LO}}$ in the data-driven approach.

The second approach, lattice QCD, offers a determination of $a_\mu^{\text{HVP,LO}}$ based entirely on SM theory, without the need for experimental inputs to quantify the nonperturbative dynamics. While published lattice-QCD results for $a_\mu^{\text{HVP,LO}}$ were not precise enough at the time to be used in the SM prediction of Ref. [5], the situation has changed significantly in recent years, thanks to dedicated efforts by several lattice collaborations [8–16]. Hence, we expect that lattice-QCD results will play an important role in obtaining a new SM prediction of a_μ and in the subsequent interpretation of the experimental measurements. Especially in light of the puzzle created in the data-driven approach by the new CMD-3 $e^+e^- \rightarrow \pi\pi$ cross section measurement, continued efforts to further improve lattice-QCD calculations to match the expected precision of the $g - 2$ experiments are clearly important.

In lattice QCD, the HVP can be computed from Euclidean time integrals of correlation functions [17], where it is advantageous to study the different regions of Euclidean time separately to refine control over systematic effects. The most common division is into three time complementary regions, known as “windows” [18]: the “short-distance” contribution a_μ^{SD} , the “intermediate-distance” contribution a_μ^{W} , and the “long-distance” contribution a_μ^{LD} . By construction, the sum of these three terms gives the total HVP contribution to a_μ .

The smallest component, a_μ^{SD} , at roughly 10% of the total, is the most sensitive to lattice discretization effects. The largest component, a_μ^{LD} , roughly 55% of the total, is the most challenging, as it is sensitive to the finite lattice volume effects and suffers from large statistical errors due to well-known signal-to-noise issues in the underlying correlation functions at large Euclidean times. The intermediate window observable, a_μ^{W} , is relatively insensitive to these two extremes and hence can be obtained reasonably straightforwardly. Both a_μ^{SD} and a_μ^{W} can be obtained with good statistical precision. The evaluation of windowed HVP observables also provides more fine-grained comparisons with data-driven results, which will

be crucial if current tensions between data-driven evaluations and lattice calculations persist after the disagreements between experimental cross-section measurements are understood or resolved. In this paper, we focus on the short- and intermediate-distance window contributions, deferring a discussion of our calculation of a_μ^{LD} to a companion paper.

Besides the division into windows with different characteristic energy scales, the HVP (either the total or within a given window) can also be divided into contributions from individual quark flavors for quark-line connected and disconnected diagrams, as well as corrections due to isospin symmetry breaking (including strong isospin breaking effects due to $m_u \neq m_d$ as well as QED). We have previously presented results for the intermediate window HVP [12], in good agreement with other, existing lattice-QCD calculations [8–11, 13, 19]. However, this previous work considered only $a_\mu^{\text{ll,W}}(\text{conn.})$ (the “light-quark connected” a_μ^{W}), omitting contributions from other quark flavors, as well as those from disconnected diagrams and isospin-breaking corrections. In this work, we present results from our lattice-QCD calculations of these additional contributions, as well as a refined calculation of $a_\mu^{\text{ll,W}}(\text{conn.})$. We note, however, that a discussion of our direct lattice-QCD calculation of the QED corrections is deferred to a separate paper. Instead, in this paper, we use a combination of perturbative QCD (pQCD), phenomenological estimates and comparisons with previous direct lattice-QCD calculations of QED corrections to estimate their contributions to the short- and intermediate-distance window observables.

Our results for these individual contributions and corrections provide a more fine-grained view into the HVP at short and intermediate distances, enabling comparisons with the corresponding results from other lattice groups as available. We also obtain complete physical results for the total short- and intermediate-distance HVP.

This paper is organized as follows. First, Sec. II A provides analytic expressions for a_μ^{SD} and a_μ^{W} in terms of the Euclidean-time vector-current correlation function, as well as the definitions of the individual contributions to these observables. Next, Sec. II B defines the isospin-symmetric QCD limit employed in the majority of these calculations. The inputs for QCD with strong-isospin breaking are also described. The ensembles employed in this work and the correlation function datasets generated from them are described in Sec. II C. Section III presents a detailed description of the general analysis procedure employed in this work: our blinding strategy (Sec. III A), the systematic corrections applied to the lattice observables (Sec. III B), our approach to taking the continuum limit (Sec. III C), and the subsequent estimation of uncertainties from these systematics using Bayesian Model averaging (BMA) (Sec. III D). In Sec. IV, we present our analyses for the individual window observables; this section is broken up into subsections describing the light-connected (Sec. IV A), strange- and charm-connected (Sec. IV B), disconnected (Sec. IV C) and the strong-isospin-breaking (Sec. IV D) contributions. Perturbative QCD is used to estimate the short-distance window observables, which we compare with our lattice determinations, in Sec. IV E, while Sec. V presents our final results for the short-distance (Sec. V A) and intermediate-distance window observables (Sec. V B). Section VI concludes with a summary of our results, including comparisons with previous lattice-QCD calculations and data-driven evaluations, and an outlook in light of our ongoing efforts to obtain the total HVP at few-permille-level precision. Appendices A and B examine discretization effects important in short-distance window observables, namely the log-enhanced discretization terms that arise in the correlation functions at small Euclidean times and the oscillatory contributions to correlation functions constructed with staggered quarks. Finally, our procedure for obtaining a complete correlation matrix in the BMA framework is given in Appendix C.

II. BACKGROUND AND SIMULATION DETAILS

A. Definitions of window observables

The leading-order hadronic-vacuum-polarization contribution to the muon anomalous magnetic moment is obtained via

$$a_\mu^{\text{HVP,LO}} = 4\alpha^2 \int_0^\infty dt C(t) \tilde{K}(t), \quad (2.1)$$

where α is the fine-structure constant, the kernel \tilde{K} stems from QED, and $C(t)$ is the Euclidean-time two-point correlation function of the electromagnetic current,

$$C(t) = \frac{1}{3} \sum_{k=1}^3 \sum_{\mathbf{x}} \langle J^k(\mathbf{x}, t) J^k(0) \rangle, \quad (2.2)$$

$$J^\mu(x) = \sum_f q_f \bar{\psi}_f(x) \gamma^\mu \psi_f(x). \quad (2.3)$$

The current $J^\mu(x)$ is summed over all quark flavors $f \in \{u, d, s, c, b, t\}$ of electric charge q_f . In lattice QCD, the calculation of $C(t)$ is straightforward, although controlling all uncertainties at the needed precision level is challenging. The QED kernel is given by

$$\tilde{K}(t) = 2 \int_0^\infty \frac{dQ}{Q} K_E(Q^2) \left[Q^2 t^2 - 4 \sin^2 \left(\frac{Qt}{2} \right) \right], \quad (2.4)$$

where the energy-momentum kernel [20], $K_E(Q^2)$, depends on the muon mass:

$$K_E(Q^2) = \frac{m_\mu^2 Q^2 Z^3 (1 - Q^2 Z)}{1 + m_\mu^2}, \quad Z = \frac{(Q^4 + 4m_\mu^2 Q^2)^{1/2} - Q^2}{2m_\mu^2 Q^2}. \quad (2.5)$$

Higher-order HVP can be obtained from Eq. (2.1) by substituting a different kernel [21–25].

Lattice-QCD calculations of $a_\mu^{\text{HVP,LO}}$ separately compute the contributions from each quark flavor and from connected and disconnected Wick contractions. Additionally, these calculations are performed in the isospin-symmetric limit in pure QCD (see Sec. II B) with the effects of strong-isospin breaking and quantum electrodynamics (QED) added as corrections to obtain the complete $a_\mu^{\text{HVP,LO}}$. The complete result is the sum of the following individual contributions,

$$a_\mu^{\text{HVP,LO}} = a_\mu^{ll}(\text{conn.}) + a_\mu^{ss}(\text{conn.}) + a_\mu^{cc}(\text{conn.}) + a_\mu^{bb}(\text{conn.}) + \dots \\ + a_\mu(\text{disc.}) + \Delta a_\mu^{ud}(\text{SIB}) + \Delta a_\mu(\text{QED}). \quad (2.6)$$

The contributions listed on the first line are collectively called the connected contributions and correspond to connected Wick contractions of Eq. (2.2) for each individual quark flavor of Eq. (2.3).¹ The first contribution on the second line is from the disconnected Wick contractions of Eq. (2.2), which contains quark-flavor mixing. In this work, we calculate

¹ The light-quark charge factor is given by $q_l^2 = q_u^2 + q_d^2 = 5/9$.

only the light- and strange-disconnected contribution. The final two terms are the strong-isospin breaking and QED corrections defined by

$$\Delta a_\mu^{ud}(\text{SIB}) = a_\mu^{uu} + a_\mu^{dd} - a_\mu^{ll}, \quad (2.7)$$

$$\Delta a_\mu^f(\text{QED}) = a_\mu^{ff}(\text{QCD} + \text{QED}) - a_\mu^{ff}. \quad (2.8)$$

For the correction due to strong-isospin breaking, a_μ^{uu} , a_μ^{dd} , and a_μ^{ll} contain both the connected and disconnected contractions, which we compute separately (see Secs. II C and IV D).

By limiting the Euclidean-time region over which $C(t)$ is integrated, one obtains the so-called one- and two-sided window observables [18]:

$$a_\mu^{\text{win}_1(t_0, \Delta)} = 4\alpha^2 \int_0^\infty dt C(t) \tilde{K}(t) \mathcal{W}_1(t, t_0, \Delta), \quad (2.9a)$$

$$a_\mu^{\text{win}_2(t_0, t_1, \Delta)} = 4\alpha^2 \int_0^\infty dt C(t) \tilde{K}(t) \mathcal{W}_2(t, t_0, t_1, \Delta), \quad (2.9b)$$

where the window functions are²

$$\mathcal{W}_1(t, t_0, \Delta) = \frac{1}{2} \left[1 - \tanh \left(\frac{t - t_0}{\Delta} \right) \right]. \quad (2.10a)$$

$$\mathcal{W}_2(t, t_0, t_1, \Delta) = \frac{1}{2} \left[\tanh \left(\frac{t - t_0}{\Delta} \right) - \tanh \left(\frac{t - t_1}{\Delta} \right) \right]. \quad (2.10b)$$

The parameters t_0 and t_1 of the \mathcal{W}_i control the location of the window's boundaries, while Δ controls the sharpness of its edges. The window functions satisfy $\mathcal{W}_1(t, t_0, \Delta) + \mathcal{W}_2(t, t_0, t_1, \Delta) = \mathcal{W}_1(t, t_1, \Delta)$, $\mathcal{W}_2(t, t_0, t_1, \Delta) + \mathcal{W}_2(t, t_1, t_2, \Delta) = \mathcal{W}_2(t, t_0, t_2, \Delta)$.

In this work, we consider two such windows, the short-distance window SD (defined with $t_0 = 0.4$ fm, $\Delta = 0.15$ fm), yielding

$$a_\mu^{\text{SD}} \equiv a_\mu^{\text{win}_1(0.4, 0.15)}, \quad (2.11)$$

and the intermediate-distance window W (defined with $t_0 = 0.4$ fm, $t_1 = 1.0$ fm, $\Delta = 0.15$ fm), yielding

$$a_\mu^{\text{W}} \equiv a_\mu^{\text{win}_2(0.4, 1.0, 0.15)}, \quad (2.12)$$

with the parameters in fm. We plot the \mathcal{W}_i in Eq. (2.10) for these window regions in Fig. 1. Also shown are the light-quark, strange-quark, and charm-quark connected contributions to the integrand, $\tilde{K}(t)C(t)$ in Eq. (2.1), using the lattice correlation functions obtained on our 0.06 fm ensemble (see Sec. II C). The light-quark contribution dominates both windows, as can be seen by the scaling factor of six applied to the strange and charm integrands in the plot. After the light, the charm is the leading contribution in the short-distance window, while the strange is the leading contribution in W. The remaining contributions in Eq. (2.6) are sub-leading for these two windows and are at the sub-percent level on the complete results.

² In earlier work [12], we used a slightly different definition of the window functions. To the accuracy given there, none of the reported digits would change. Here, we use the standard definitions, namely Eq. (3.26) of Ref. [5].

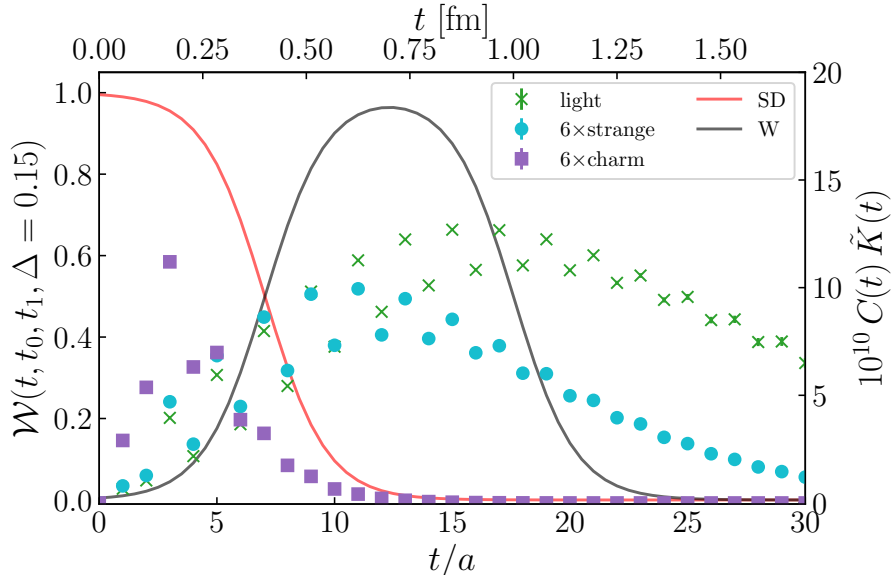


FIG. 1. The SD (red) and W (black) window functions corresponding to the parameters in Eqs. (2.11) and (2.12), overlaid with raw lattice data for the integrand of Eq. (2.1) for light- (green crosses), strange- (blue circles), and charm-connected (purple squares) contributions obtained on our ensemble with $a \approx 0.06$ fm (see Table I).

B. Physical inputs

Our lattice calculations make use of several ensembles of four-flavor gauge-field configurations generated by the MILC collaboration (details are given below in Sec. II C). With one exception, these ensembles are generated in the limit of isospin symmetry (that is, with the up- and down-quark masses set to be equal) and without dynamical QED. Converting our numerical results into physical units requires the selection of a set of physical inputs which determine the quark masses and the overall energy scale.

Our approach to scale setting follows the prescription introduced in Refs. [26, 27] and extended to charm in [28]. The energy scale is fixed by the pion decay constant f_{π^+} . The masses of the u , d , and s quarks are determined by the masses of the π^+ , K^0 , and K^+ mesons, and the c quark mass is fixed by the mass of the D_s^+ meson. In the “isospin-symmetric, pure-QCD world” matching our simulations, with equal up- and down-quark masses and without QED, we use the following inputs to define the physical point:

$$(\text{isospin-symmetric pure-QCD world}) \Rightarrow \begin{cases} f_{\pi^+} & \equiv 130.50 \text{ MeV}, \\ M_{\pi^+} & \equiv 134.977 \text{ MeV}, \\ M_K & \equiv 494.496 \text{ MeV}, \\ M_{D_s^+} & \equiv 1967.02 \text{ MeV}. \end{cases} \quad (2.13)$$

This prescription defines the physical light-quark mass as $m_l \equiv (m_u + m_d)/2$. The pion mass and decay constant values are taken from the 2016 Particle Data Group [29] directly,³

³ The 2016 values for these quantities are completely consistent with those from the 2024 Particle Data Group [30].

using $M_{\pi^+} = M_{\pi^0}$ in the pure-QCD world since M_{π^0} is not affected significantly by electromagnetic corrections or by up-down quark mass splitting. The other meson masses must have electromagnetic effects removed in order to be used to set scales in our pure-QCD simulations; to do so, we make use of the results from Ref. [31]. The kaon mass M_K listed above is the root-mean-squared (RMS) average of M_{K^0} and M_{K^+} , corresponding to the isospin-symmetric limit.⁴ Details on how the specific values given above were obtained can be found in Sec. IV of that work and references therein.

To study isospin-breaking effects, we also need a physical input for $m_d - m_u$. For this case, we replace the RMS M_K above with the individual values for the K^0 and K^+ from Ref. [31]:

$$(\text{isospin-broken pure-QCD world}) \Rightarrow \begin{cases} f_{\pi^+} & \equiv 130.50 \text{ MeV}, \\ M_{\pi^+} & \equiv 134.977 \text{ MeV}, \\ M_{K^+} & \equiv 491.405 \text{ MeV}, \\ M_{K^0} & \equiv 497.567 \text{ MeV}, \\ M_{D_s^+} & \equiv 1967.02 \text{ MeV}. \end{cases} \quad (2.14)$$

Setting the three meson masses $\{M_{\pi^+}, M_{K^+}, M_{K^0}\}$ to their physical values fixes the three light quark masses $\{m_u, m_d, m_s\}$. We implement this scheme with the equivalent set $\{M_{\pi^+}, M_K, \Delta M_K^2\}$, with

$$\Delta M_K^2 \equiv M_{K^0}^2 - M_{K^+}^2 = 6094 \text{ MeV}^2. \quad (2.15)$$

In this approach, adjusting M_{π^+} and RMS M_K to their physical values fixes m_l and m_s , and adjusting ΔM_K^2 determines the up-down mass splitting $m_d - m_u$. This implementation is convenient given the data available in the analysis below.

Particularly for the analysis of strong isospin breaking, it is helpful to define fictitious physical pion masses with both constituent quark masses set to m_u, m_d , or $m_l \equiv (m_u + m_d)/2$. In principle, this could be done from the pion and kaon mass inputs above by using the leading-order Gell-Mann–Oakes–Renner [33] (GMOR) relations, *i.e.*, leading-order χ PT, which states that the squared pion and kaon masses scale linearly with quark mass. Although this statement is locally true to good approximation, inclusion of both pions and kaons simultaneously in leading-order χ PT relations can lead to deviations due to the presence of significant next-to-leading order corrections.

Instead of assuming purely GMOR scaling, we adapt the results from the MILC Collaboration [34], which (in the same scheme as above) computes the up-down quark mass ratio to be $m_u/m_d = 0.4529(48)_{\text{stat}} \left(\begin{smallmatrix} +150 \\ -67 \end{smallmatrix} \right)_{\text{syst}}$. Following the procedures of the Flavour Lattice Averaging Group (FLAG) [35] for symmetrizing two-sided error and combining statistical and systematic errors in quadrature, this becomes $m_u/m_d = 0.4550(138)$. Then, using GMOR scaling only in the vicinity of the pion mass, we have the results

$$M_{\pi}^{uu} = M_{\pi^+} \sqrt{\frac{2}{1 + m_d/m_u}} = 106.7(1.1) \text{ MeV}, \quad (2.16)$$

⁴ Note that the arithmetic mean was used instead of the RMS mean to set M_K in our previous paper [12]. While the difference is negligibly small for the $a_{\mu}^{ll, \text{W}}(\text{conn.})$ computed there, the RMS mean is better motivated by χ PT. Our input value for M_{K^+} differs by 0.2 MeV from the FLAG separation prescription of Ref. [32], but this difference should also be negligible.

TABLE I. Ensemble parameters used in this work. The first column lists the approximate lattice spacings in fm. (In previous work, the ensemble labeled “0.04” was labeled “0.042.”) The second column gives the spatial length L of the lattices in fm. The third column lists the volumes of the lattices in number of space-time points. The fourth to seventh columns gives the sea-quark masses in lattice-spacing units. The eighth column lists the gradient-flow scale w_0/a defined in Ref. [36]. Our values come from an extensive recent analysis, including many additional ensembles. Some preliminary results were presented in Ref. [37]. The values here correspond to Wilson flow with the clover observable and do not include perturbative improvement. The w_0/a value for 0.15' fm is taken to be equivalent to the 0.15 fm result. To convert simulation results to physical units, we take $w_0 = 0.1715(9)$ fm [38].

$\approx a/\text{fm}$	L/fm	$N_s^3 \times N_t$	am_u^{sea}	am_d^{sea}	am_s^{sea}	am_c^{sea}	w_0/a
0.15'	4.85	$32^3 \times 48$	0.001524	0.003328	0.0673	0.8447	1.13227(18)
0.15	4.85	$32^3 \times 48$	0.002426	0.002426	0.0673	0.8447	1.13227(18)
0.12	5.81	$48^3 \times 64$	0.001907	0.001907	0.05252	0.6382	1.41060(28)
0.09	5.61	$64^3 \times 96$	0.00120	0.00120	0.0363	0.432	1.95148(41)
0.09*	5.61	$64^3 \times 96$	0.001326	0.001326	0.03636	0.4313	1.95021(57)
0.06	5.45	$96^3 \times 128$	0.0008	0.0008	0.022	0.260	3.01838(92)
0.04	6.12	$144^3 \times 288$	0.000569	0.000569	0.01555	0.1827	4.03242(195)

$$M_\pi^{dd} = M_{\pi^+} \sqrt{\frac{2}{1 + m_u/m_d}} = 158.3(0.8) \text{ MeV}. \quad (2.17)$$

C. Lattice ensembles and correlation functions

We employ seven of the MILC Collaboration’s four-flavor lattice-QCD configurations with dynamical up, down, strange, and charm quarks in this work (see Table I). The ensembles use the HISQ action [41] for the sea quarks, a Symanzik-improved gauge action [42–46] that includes the plaquette, the 1×2 rectangle, and the so-called bent-chair six-link term for the gluon fields as well as tadpole improvement [47] based on the plaquette. Details of the configuration generation can be found in Refs. [31, 48, 49].⁵ Our physical mass ensemble set includes five lattice spacings spanning the range $a \approx 0.15\text{--}0.04$ fm. The sea-quark masses listed in Table I are tuned to the isospin-symmetric physical point, defined in Eq. (2.13), except for the 0.15' fm ensemble, in which the sea-quark masses are tuned to the isospin-broken physical point of Eq. (2.14).⁶ Refined values of the tuned sea-quark masses were obtained from an analysis in Ref. [31], in which pseudoscalar-meson masses and decay constants were computed using 24 gauge ensembles with six lattice spacings ranging from $a \approx 0.15\text{--}0.03$ fm.

⁵ The 0.09* fm ensemble was, in-part, generated by the CalLat collaboration [50] using retuned values of the quark masses determined by MILC [28]. Of the 1000 configurations used in this work, half were generated by CalLat, and half were generated by the MILC Collaboration.

⁶ The 0.15' fm ensemble, which has light sea quarks with $m_u \neq m_d$, was used previously [51] to test for sea isospin-breaking effects, and we use it here for the same purpose and with improved statistics.

TABLE II. Pseudoscalar meson masses calculated on each of the gauge ensembles given in Table I for various combinations of valence quark masses. Results are shown in lattice units (column 5), as well as in MeV (column 4) using the values of w_0/a and w_0 (fm) from Table I to convert. The label l denotes the symmetrized light-quark mass $m_l = (m_u + m_d)/2$. On the 0.09 fm ensemble, the valence m_l is mistuned to be somewhat lighter than physical; the retuned valence mass is labeled r . The 0.09* fm ensemble includes a lighter-than-physical up-quark mass, denoted h , as described in the text. Meson masses from previous publications are marked with § ([39]), † ([40]), and ‡ ([12]). Column 2 lists the valence quark masses am_q only if they differ from the sea-quark masses listed in Table I.

$\approx a/\text{fm}$	am_q	qq'	$M_{\gamma_5 \otimes \gamma_5}/\text{MeV}$	$aM_{\gamma_5 \otimes \gamma_5}$
0.15'		uu	107.31(56)	0.082368(18)
		ll	134.73(71)	0.103420(18)
		dd	157.20(83)	0.120665(17)
		us	489.9(2.6)	0.376023(22)
		ls	493.1(2.6)	0.37847(20)
		ds	496.0(2.6)	0.380749(19)
0.15	0.001524	uu^\ddagger	107.30(56)	0.082362(11)
	0.003328	ll^\S	134.73(71)	0.103414(11)
		dd^\ddagger	157.18(83)	0.120652(11)
		ls^\ddagger	493.1(2.6)	0.37847(11)
		sc^\ddagger	1961(10)	1.50544(19)
0.12	0.001190	uu^\ddagger	107.01(56)	0.0659338(57)
	0.002625	ll^\ddagger	134.82(71)	0.0830651(63)
		dd^\ddagger	157.59(83)	0.0970979(67)
		ls^\ddagger	493.3(2.6)	0.303949(77)
		sc^\ddagger	1963(10)	1.209384(78)
0.09	0.00133	ll^\ddagger	128.40(68)	0.057184(30)
	0.00183	rr	135.17(71)	0.060202(32)
		dd	158.56(84)	0.070617(37)
		ls^\ddagger	492.8(2.6)	0.219482(70)
		sc^\ddagger	1965(10)	0.875909(63)
0.09*	0.000514	hh	84.87(45)	0.037824(12)
	0.001802	ll	134.91(71)	0.060125(16)
		dd	156.69(82)	0.069831(17)
		ls	493.8(2.6)	0.220071(66)
		sc	1968(10)	0.876681(64)
0.06		ll^\ddagger	134.90(72)	0.038842(29)
		ls^\ddagger	495.3(2.6)	0.142607(51)
		sc^\ddagger	1963(10)	0.565279(49)
0.04		ll^\ddagger	134.46(71)	0.028981(18)
		ls^\ddagger	493.2(2.6)	0.106297(39)
		sc^\ddagger	1965(10)	0.42352(13)

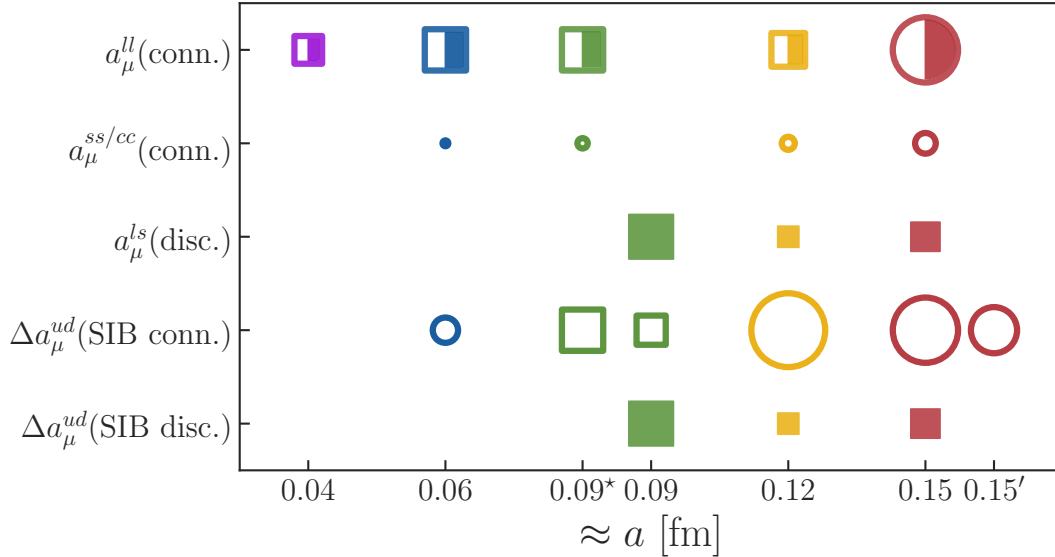


FIG. 2. Visual representation of the correlation-function datasets on the ensembles from Table I used in this work. Circles correspond to datasets computed with the truncated solver method; squares are datasets in which the low-modes of the Dirac operator are treated exactly with eigenvector methods. Filled colors are one-link vector-current datasets; unfilled colors are local-operator datasets. The area of each symbol corresponds to the statistics of each ensemble. We stress that due to the different ways these datasets were generated, only statistical comparisons within specific observables are sensible.

Table II lists the pseudoscalar meson masses, labeled by their valence-quark content qq' , obtained on the seven ensembles. On all ensembles (except 0.15' fm), the valence quarks denoted l, s, c are generated with the same masses as the sea quarks listed in Table I. We see that the sea-quark masses are tuned to within 1% of their physical values on all ensembles, except for the older 0.09 fm ensemble. On the ensembles with $a \gtrsim 0.09$ fm we include correlation functions generated at additional light valence-quark masses. The valence quarks denoted by u, d are tuned according to Eq. (2.14).⁷ To compensate for the mistuning of the light sea quarks in the 0.09 fm ensemble, a retuned light-valence quark mass (see the rr entry in Table II) is included in the analysis. Finally, the 0.09* fm data set includes hh correlators generated at a valence-quark mass where the “harmonic mean square” of the full set of taste-pion masses, defined in Ref. [8], equals the physical pion mass of Eq. (2.13). The resulting hh Goldstone pion mass is listed in Table II.

Two different discretizations of the vector current are employed, local and one-link,

$$J_k^{\text{local}}(x) = \sum_f q_f \bar{\chi}_f(x) (-)^{x_k} \chi_f(x), \quad (2.18a)$$

$$J_k^{1\text{-link}}(x) = \sum_f q_f \frac{1}{2} \bar{\chi}_f(x) \eta_k(x) \left(U_k(x) \chi_f(x + \hat{\mathbf{k}}a) + U_k^\dagger(x - \hat{\mathbf{k}}a) \chi_f(x - \hat{\mathbf{k}}a) \right), \quad (2.18b)$$

where χ_f is the field of flavor f in the HISQ action and η_k is the staggered sign factor that appears in place of Dirac matrices [41]. Local and one-link bilinears correspond to the taste

⁷ On the 0.15' fm ensemble, the u, d, s, c valence quark masses match the sea quarks, while the valence quark denoted l is adjusted so that the ll pion mass takes on the physical value listed in Eqs. (2.13) and (2.14).

TABLE III. Renormalization factors for the local and one-link vector current used in this work. Results for the local current from the form-factor method are given in the first column [52]. RI-SMOM results for the local and one-link currents are taken from [53] and are given in columns three and four. The 0.04 fm one-link result is obtained from the fit described in that work.

$\approx a/\text{fm}$	$Z_{V, \text{local}}^{\text{FF}}$	$Z_{V, \text{local}}^{\text{RI-SMOM}}$	$Z_{V, \text{one-link}}^{\text{RI-SMOM}}$
0.15	0.9881(10)	0.95932(18)	1.14017(20)
0.12	0.9922(4)	0.97255(22)	1.13784(24)
0.09	0.9940(5)	0.98445(11)	1.13428(13)
0.06	0.9950(6)	0.99090(36)	1.12518(39)
0.04	0.9949(7)	0.99203(108)	1.11811(68)

vector and taste singlet, respectively. The resulting correlators and window observables have different discretization effects (see Appendix A for a discussion of the discretization effects that arise at short distances). This is useful for constraining continuum extrapolations, as discussed in Sec. IV.

For each of the contributions in Eq. (2.6), the vector-current correlation-function datasets that are generated on these ensembles are shown in Fig. 2. In the figure, circles correspond to correlation function data constructed from propagators computed using the truncated solver method (TSM) [54, 55]. Specifically, using random-wall sources, we compute one fine-residual conjugate gradient solve and a number of loose-residual solves (N_{loose}). The size of the circle corresponds to the total number of statistics $N_{\text{conf}} \times N_{\text{loose}}$. The exact numbers for these, for each contribution, are detailed in the respective sections in Sec. III. The squares correspond to correlation function data generated using low-mode averaging (LMA) [56–58], as explained below. In order to minimize autocorrelations in our LMA calculation, we select an evenly-spaced subset of the stored configurations in each ensemble that includes, at most, every other configuration. Again, the size of the square corresponds to the total statistics, $N_{\text{conf}} \times N_{\text{src}}$, with specific numbers given in relevant subsections of Sec. III. The unfilled symbols are datasets generated using the local current, while filled symbols indicate data generated using the one-link current. In the case of the $a_{\mu}^{\text{H}}(\text{conn.})$, both currents are employed. For all our datasets, we perform extensive tests for autocorrelations, specifically both measuring the integrated autocorrelation time and also examining how the statistical errors change with binning. For the strange and charm datasets, we account for the significant autocorrelations identified in this procedure by binning with bin sizes up to ten, leading to the small numbers of independent configurations seen in Fig. 2. We see no indications of autocorrelations in any of the other data sets.

For the LMA procedure, we use color-diagonal random wall (RW) sources to approximate the high-mode remainder. Specifically, 2,000 exact eigenvector low-mode pairs enter the correlation-function generation in three important ways. First, they are used to calculate the low-mode all-to-all (A2A) contribution to the correlation function, which gives the exact low-mode result for a given lattice configuration. Second, low modes are used to deflate the conjugate gradient solver for each RW source, significantly reducing the iterations required to reach the target residual of the solver. Finally, the low-mode contribution to the RW correlation function is obtained as a byproduct of the deflation process; see Eq. (2.20b).

For the connected contribution we use

$$C_{\text{LMA}}(t) = \frac{1}{3} \sum_{k=1}^3 \langle C_{\text{RW}}^k(U, t_0, t_1) - C_{\text{RW,LL}}^k(U, t_0, t_1) + C_{\text{A2A,LL}}^k(U, t_0, t_1) \rangle_U, \quad (2.19)$$

where $t = t_1 - t_0$, $\langle \dots \rangle_U$ denotes averaging over the gauge-field ensemble, and

$$C_{\text{RW}}^k(U, t_0, t_1) = \frac{1}{4N_S^3} \sum_f q_f^2 \text{Tr} \left\{ M_f^{-1}(U) \Gamma_{t_0}^k \xi_{t_0} \xi_{t_0}^\dagger M_f^{-1}(U) \Gamma_{t_1}^k \right\}, \quad (2.20a)$$

$$C_{\text{RW,LL}}^k(U, t_0, t_1) = \frac{1}{4N_S^3} \sum_f q_f^2 \text{Tr} \left\{ M_{L,f}^{-1}(U) \Gamma_{t_0}^k \xi_{t_0} \xi_{t_0}^\dagger M_{L,f}^{-1}(U) \Gamma_{t_1}^k \right\}, \quad (2.20b)$$

$$C_{\text{A2A,LL}}^k(U, t_0, t_1) = \frac{1}{4N_S^3} \sum_f q_f^2 \text{Tr} \left\{ M_{L,f}^{-1}(U) \Gamma_{t_0}^k M_{L,f}^{-1}(U) \Gamma_{t_1}^k \right\}. \quad (2.20c)$$

Here, the trace is over color and space-time components; N_S^3 is the spatial volume; the $1/4$ is a rooting factor; ξ_t denotes a RW source at time t , the average over which is implicit; the flavor sum is over l, s for the isosymmetric case and u, d, s for the isobroken case; $M_f(U)$ is the Dirac matrix for the configuration for flavor f ; $M_{L,f}^{-1}(U) = \sum_i \frac{1}{\lambda_{i,f}(U)} v_i(U) v_i^\dagger(U)$, where $v_i(U)$ and $\lambda_{i,f}(U)$ are the eigenvectors and eigenvalues of the Dirac matrix satisfying $M_f(U) v_i(U) = \lambda_{i,f}(U) v_i(U)$; and the Γ_t matrix incorporates the staggered phases and shifts in the definition of the currents given in Eqs. (2.18a) and (2.18b) on a selected time slice t , as follows for $x = (\mathbf{x}, t)$ and $x' = (\mathbf{x}', t')$:

$$\Gamma_{t_0, \text{local}}^k(x, x') = (-)^{x_k} \delta_{\mathbf{x}, \mathbf{x}'} \delta_{t, t_0} \delta_{t_0, t'}, \quad (2.21a)$$

$$\Gamma_{t_0, 1\text{-link}}^k(x, x') = \eta_k(x) U_k(x) \delta_{\mathbf{x} + \mathbf{i}a, \mathbf{x}'} \delta_{t, t_0} \delta_{t_0, t'} + \text{h.c.} \quad (2.21b)$$

For the disconnected contribution, we use

$$C_{\text{RV}}^k(U, t_0, t_1) = -\frac{1}{16N_S^3} \sum_{f, f'} q_f q_{f'} \text{Tr} \left\{ M_f^{-1}(U) \Gamma_{t_0}^k \xi \xi^\dagger \right\} \text{Tr} \left\{ \xi \xi^\dagger M_{f'}^{-1}(U) \Gamma_{t_1}^k \right\}, \quad (2.22a)$$

$$C_{\text{RV,LL}}^k(U, t_0, t_1) = -\frac{1}{16N_S^3} \sum_{f, f'} q_f q_{f'} \text{Tr} \left\{ M_{L,f}^{-1}(U) \Gamma_{t_0}^k \xi \xi^\dagger \right\} \text{Tr} \left\{ \xi \xi^\dagger M_{L,f'}^{-1}(U) \Gamma_{t_1}^k \right\}, \quad (2.22b)$$

$$C_{\text{A2A,LL}}^k(U, t_0, t_1) = -\frac{1}{16N_S^3} \sum_{f, f'} q_f q_{f'} \text{Tr} \left\{ M_{L,f}^{-1}(U) \Gamma_{t_0}^k \right\} \text{Tr} \left\{ M_{L,f'}^{-1}(U) \Gamma_{t_1}^k \right\}, \quad (2.22c)$$

where taste-symmetry requires the one-link current. Here, the random source ξ has support over the entire lattice volume (RV). On some of the ensembles, we use the TSM method to reduce the cost of the inversions. Further details, including numbers of random sources, are discussed below and in Refs. [59, 60].

Two different schemes are employed to renormalize the currents. The first set of renormalization factors, Z_V^{FF} , are obtained from a form factor approach [52]. They were used in previous Fermilab, HPQCD, and MILC HVP calculations [12, 39] in which the local current was employed. The second approach employs the RI-SMOM scheme, and the factors, $Z_V^{\text{RI-SMOM}}$, are given in Refs. [53, 61]. The RI-SMOM scheme has a residual dependence on

the matching scale μ , even for Z_V , and we take the $Z_V^{\text{RI-SMOM}}$ values at $\mu = 2$ GeV from those works. The value of $Z_V^{\text{RI-SMOM}}$ for the one-link current at 0.04 fm was not calculated in those works; hence, we obtain it from the fit procedure described in Ref. [53]. Table III tabulates the values of all vector-current renormalization factors Z_V needed in the analysis explained in the subsequent sections.

III. ANALYSIS PROCEDURE

Our overarching analysis approach follows the strategy described in Ref. [12]. Here, we recap the main steps of our analysis strategy, with a focus on the procedures specific to this work. The window observables are obtained according to Eqs. (2.11) and (2.12) from weighted Euclidean-time integrals of the correlation functions $C(t)$. In Ref. [12], we examined the effects of the oscillating contributions, which arise in our staggered correlation functions, on intermediate-distance a_μ observables in the continuum limit. Comparing results obtained from fit reconstructions that remove the oscillating terms versus direct integration of the correlation functions, we found that the oscillating contributions have no effect on the observables after continuum limit extrapolation. Extending this study to the short-distance window observables in Appendix B, we find the same result. Hence, in this work, we use only direct integration to obtain the short- and intermediate-distance window observables.

The following subsections describe our strategies for each analysis step. First, Sec. III A provides a description of the blinding applied to each individual window observable. The lattice corrections for finite-volume effects, pion-mass mistunings and in some cases taste-breaking effects are detailed in Sec. III B. These corrections are applied only to intermediate window observables containing light-quark contributions ($a_\mu^{ll,W}(\text{conn.})$, $a_\mu^W(\text{disc.})$, $\Delta a_\mu^{ud,W}(\text{SIB})$). Subsequently, all observables are extrapolated to the continuum, which is described in Sec. III C. In the final step, the analysis variations for the corrections and continuum extrapolations are input into a BMA, as discussed in Sec. III D.

A. Blinding

As an overview, first all window observables are blinded including a multiplicative blinding factor, with some including an additional additive blind:

$$a_\mu^{(X),\text{blind}} = \alpha^{(X)} a_\mu^{(X)} + \beta^{(X)}. \quad (3.1)$$

The additive blind is present for the local current light-quark connected dataset on the 0.15 fm ensemble (see Table I), where previously used data are used in this analysis; all the other correlation function data used in the light-quark connected analysis are new. In addition, we use an overall shared additive blind for the connected $\Delta a_\mu^{ud}(\text{SIB})$ analysis to avoid cancellation of blinding factors when constructing the ratio to $a_\mu^{ll}(\text{conn.})$.

For the light-quark connected analysis (Sec. IV A), the blinding is applied to the renormalization factor Z_V , which is then squared in the observable a_μ . The factors multiplying Z_V are drawn uniformly over the range [0.8, 1.2], resulting in a multiplicative blind α in the range [0.64, 1.44]. The additive blind β for the 0.15 fm ensemble is set equal to the standard deviation of that a_μ result times a random number drawn uniformly from the range $[-1, 1]$.

The strange and charm analyses (Sec. IV B) are blinded in exactly the same way. For the disconnected analysis (Sec. IV C), α is drawn from the range $[0.8, 1.2]$, and no additive blind is used. Finally, for the SIB analysis (Sec. IV D), α is drawn from the range $[0.95, 1.05]$ (connected) and $[0.6, 1.4]$ (disconnected), and the connected observables include an additional additive blind β drawn uniformly from $[-2, 2] \times 10^{-10}$. The blinks are held in place until all individual analyses are complete. The analyses are then frozen, and the blinks are removed.

B. Lattice corrections

We perform our corrections for finite volume, pion-mass mistuning, and taste breaking by expressing the physical point as

$$a_\mu(L_\infty, M_{\pi_{\text{phys}}}) = a_\mu(L_{\text{latt.}}, M_{\pi_{\text{latt.}, \xi_1}}, \dots, M_{\pi_{\text{latt.}, \xi_{16}}}) + \Delta_{\text{FV}} + \Delta_{M_\pi} + \Delta_{\text{TB}}, \quad (3.2)$$

where the first term on the RHS corresponds to lattice data and

$$\Delta_{\text{FV}} = a_\mu(L_\infty, M_{\pi_{\text{latt.}, \xi_1}}, \dots, M_{\pi_{\text{latt.}, \xi_{16}}}) - a_\mu(L_{\text{latt.}}, M_{\pi_{\text{latt.}, \xi_1}}, \dots, M_{\pi_{\text{latt.}, \xi_{16}}}), \quad (3.3)$$

$$\Delta_{M_\pi} = a_\mu(L_\infty, M_{\pi_{\text{phys}, \xi_1}}, \dots, M_{\pi_{\text{phys}, \xi_{16}}}) - a_\mu(L_\infty, M_{\pi_{\text{latt.}, \xi_1}}, \dots, M_{\pi_{\text{latt.}, \xi_{16}}}), \quad (3.4)$$

$$\Delta_{\text{TB}} = a_\mu(L_\infty, M_{\pi_{\text{phys}}}) - a_\mu(L_\infty, M_{\pi_{\text{phys}, \xi_1}}, \dots, M_{\pi_{\text{phys}, \xi_{16}}}). \quad (3.5)$$

In particular, we correct the light-quark containing observables, where our estimates of the corrections are based on the use of effective field theory (EFT) and EFT-inspired models that capture the dominant low-energy, two-pion physics contribution to $a_\mu^{\text{HVP,LO}}$. We consider variations obtained from five different approaches: next-to-leading-order (NLO) and next-to-next-to-leading order (NNLO) chiral perturbation theory (χ PT) [8, 9, 62–65], the chiral model (CM) [66] employed in Ref. [39], the Meyer-Lellouch-Lüscher-Gounaris-Sakurai (MLLGS) approach [67–74], and the Hansen-Patella (HP) scheme [75]. These low-energy effects are heavily suppressed in the short-distance window region, which is also outside the range of validity of these EFT-based schemes. Hence, we do not include these corrections for short-distance window observables. For contributions from heavier flavors, these effects are expected to be negligible compared with the level of precision of our calculation.

The finite-volume and taste-breaking corrections used for the connected contributions are given in Figs. 3 and 4, respectively. The corrections to the disconnected contribution are obtained by multiplying their connected counterparts by $-1/10$. The pion-mass mistuning corrections are small (at the sub-permille level) where applicable due to the accurate tuning of the ensemble masses, and hence are not shown. We do not apply MLLGS to the data at 0.15 fm because the heaviest-taste two-pion pair lies above the ρ mass; see the discussion in the MLLGS section of Ref. [8].

Figures 3 and 4 show that the expected dependencies on the lattice spacing, lattice volumes, and pion masses are largely followed. Any slight deviations from the expected behavior are likely the result of error introduced by applying the models slightly outside their range of validity; the use of several EFT and EFT-inspired models accounts for this error in the BMA systematic uncertainty. Additionally, one of the largest sources of systematic uncertainty for $a_\mu^{l, \text{W}}(\text{conn.})$, $a_\mu^{\text{W}}(\text{disc.})$, and $\Delta a_\mu^{ud, \text{W}}(\text{SIB, conn.})$ results from the discrepancy between different finite-volume correction schemes—specifically between CM (and, to a lesser extent, NLO χ PT) and the other EFT and EFT-inspired models. Correlations between observables due to this systematic uncertainty are discussed in Appendix C.

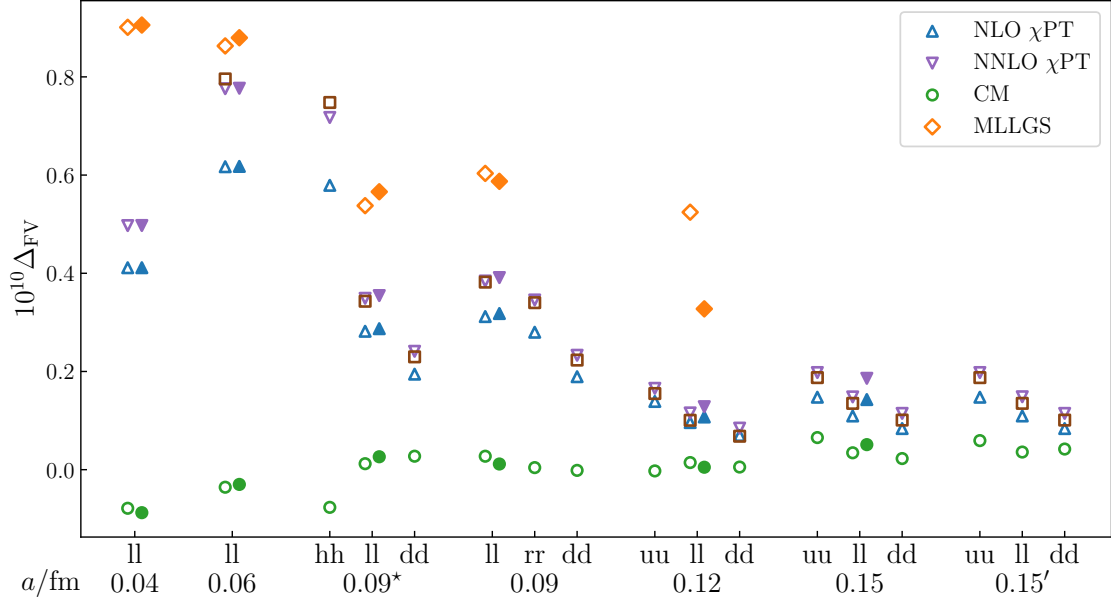


FIG. 3. Connected finite volume corrections for each ensemble and valence quark content on W. The unfilled symbols correspond to the local current and the filled to the one-link.

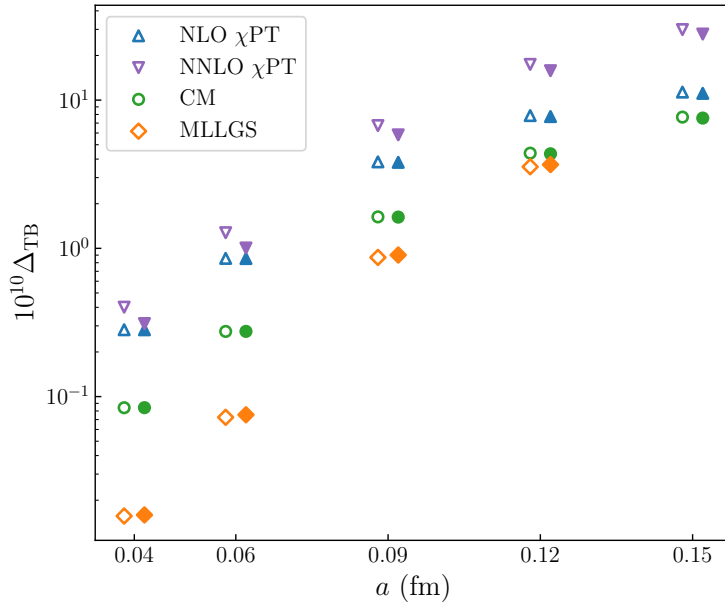


FIG. 4. Connected taste breaking corrections for each lattice spacing at the light valence quark point on W. The unfilled symbols correspond to the local current and the filled to the one-link.

C. Continuum extrapolations

For each observable, we consider variations of the continuum fit function and the data included, dropping data at certain lattice spacings when appropriate.⁸ The general form of the continuum fit function employed for almost all observables, except for $\Delta a_\mu^{ud}(\text{SIB, conn.})$

⁸ We do not perform fits where the number of degrees of freedom is negative.

(see Eq. (4.13)), is

$$a_\mu(a, M_A) = a_\mu [1 + F^{\text{disc.}}(a) + F^M(M_A)], \quad (3.6)$$

where $F^{\text{disc.}}(a)$ is adjusted as needed to describe the discretization effects of each observable. The function $F^M(M_A)$ accounts for any residual mass-mistuning effects in our extrapolations and is given by

$$F^M(M_A) = C_{\text{sea}} \sum_{A=\pi, K} \delta M_A^2, \quad \delta M_A^2 = \frac{M_{A, \text{phys.}}^2 - M_{A, \text{latt.}}^2}{M_{A, \text{phys.}}^2}, \quad (3.7)$$

unless otherwise specified in the individual analysis subsections of Sec. IV. In Ref. [12], we parameterized F^M in terms of the quark masses. The parameterization in terms of the meson masses used here makes it straightforward to match to the isospin-symmetric and isospin-broken QCD schemes defined in Sec. II B. Following the reasoning of Refs. [12, 39], we impose the Gaussian prior constraint $C_{\text{sea}} = 0.000(2)$ on this term. This choice is consistent with the prior used in Refs. [12, 39] in the quark-mass parametrization, $C_{\text{sea}}^{\text{quark}} = 0.0(3)$.

For each $a_\mu^{\text{HVP, LO}}$ observable, we use an empirical Bayes procedure to obtain guidance for the important terms in the continuum fit functions. This procedure was outlined at the end of Sec. III D of Ref. [12]. Here, we use the following functional form for $F^{\text{disc.}}(a)$ in our empirical Bayes fits:

$$F_{\text{emp}}^{\text{disc.}}(a) = c_{1l} x \log(a\Lambda) + \sum_{i=1}^4 \sum_{j=0}^4 c_{ij} x^i \alpha_s^j, \quad x \equiv (a\Lambda)^2. \quad (3.8)$$

The scale Λ is chosen to maximize the Gaussian Bayes Factor (see Eq. (28) of Ref. [76]), which is proportional to the marginal likelihood (model evidence) coefficients in Eq. (3.8). The coefficients are constrained with Gaussian priors $c_{1l}, c_{ij} = 0(1)$. Following Ref. [31] we use $\alpha_s = \alpha_V(2/a)$ and take $\alpha_V(n_f = 4, \mu = 5.0 \text{ GeV}) = 0.2530(38)$ from Ref. [77], where we evolve the coupling using the four-loop beta function [78–80]. Equation (3.8) accounts for log-enhancement effects in short-distance window observables [10, 81–83], by allowing for a leading a^2 term instead of the expected $a^2 \alpha_s$ for the local current and for a leading $a^2 \log(a)$ for the one-link current; see Appendix A for further discussion.

The continuum fit functions used in the analyses of the individual HVP observables are specified in the respective subsections of Sec. IV. They are also informed by these theoretical expectations, while the empirical Bayes analyses provide guidance for the scale Λ and the sub-leading discretization terms. In order to regulate the degrees of freedom in the continuum fits, we include a prior on the highest order terms of

$$C_{a^k} = 0(2). \quad (3.9)$$

This prior has twice the width of the priors used in the empirical Bayes analysis; hence, it does not significantly influence our continuum limit beyond assisting with stability in some cases.

D. Bayesian Model Averaging

In the final step, the uncertainties associated with the systematic corrections, needed to obtain the observables in the continuum and infinite volume limits and at the physical point,

are estimated using BMA [84, 85]. In the BMA language, the systematic corrections are referred to as “models.” This analysis approach is detailed in Ref. [12]. In the context of lattice field theory calculations, BMA using the Akaike information criterion in a frequentist context was pioneered in Refs. [86, 87]; an early use of BMA for lattice QCD was presented in Ref. [88]. The formulas for the mean and variance from the BMA are given by

$$\langle a_\mu \rangle = \sum_{n=1}^{N_M} \langle a_\mu \rangle_n \text{pr}(M_n | D), \quad (3.10)$$

$$\sigma_{a_\mu}^2 = \sum_{n=1}^{N_M} \sigma_{a_\mu, n}^2 \text{pr}(M_n | D) + \sum_{n=1}^{N_M} \langle a_\mu \rangle_n^2 \text{pr}(M_n | D) - \langle a_\mu \rangle^2, \quad (3.11)$$

where N_M is the number of models and the probability of a specific model M given the data D is defined through the Bayesian Akaike information criterion (BAIC) weight [85, 89],

$$\text{pr}(M | D) \equiv \text{pr}(M) \exp \left[-\frac{1}{2} (\chi_{\text{data}}^2(\mathbf{a}^*) + 2k + 2N_{\text{cut}}) \right]. \quad (3.12)$$

Here, χ_{data}^2 is the standard chi-squared function, *not* including the contribution of the priors, and \mathbf{a}^* is the posterior mode (*i.e.*, the best-fit point for the vector of fit parameters \mathbf{a} when optimized against the augmented chi-squared function [76]). N_{cut} is the number of data points cut from a data set—in this case, the number of ensembles omitted from a given extrapolation. The parameter k is the number of independent parameters in a given fit function. The factor $\text{pr}(M)$ is the prior probability of a given M .

For most observables, we take $\text{pr}(M) = 1/N_M$, which corresponds to the minimal *a priori* biasing of some models in favor of others. For $a_\mu^{ll, W}(\text{conn.})$ and $\Delta a_\mu^{ud}(\text{SIB, conn.})$, the flat prior $\text{pr}(M) = 1/N_M$ implicitly biases the BMA in favor of certain types of models over others due to combinatorial effects; see Secs. IV A and IV D 1 for the choices of model priors for these observables. Our procedure for obtaining complete error budgets from the respective BMA analyses is described in Ref. [12], with any additional considerations described in the relevant analysis sections below.

The probability weights defined in Eq. (3.12) can be used to assess the relative weight of specific analysis choices in the BMA. Comparison of these weights can identify if a particular correction scheme or fit-function variation is preferred or suppressed by the averaging procedure. This identification is achieved by computing the “subset probability” of the model subset S from the relative posterior probability of the variations contained in S :

$$\text{pr}(S|D) = \sum_{M_i \in S} \text{pr}(M_i|D). \quad (3.13)$$

The subset probability encapsulates the relative weight of the models in a given subset compared with the whole model space as informed by the data (see, for example, the pie charts in Figs. 6 and 8).

In order to account for correlations in the different contributions in Eq. (2.6) due to common parameter choices and common ensembles, random-sources, and datasets, we perform a global statistical and parametric bootstrap over all the analyses to generate a complete correlation matrix of the different observables computed in this work. We create five hundred bootstrap samples containing the resampled correlation function data as well as a

single Gaussian draw per sample of all the renormalization factors given in Table III, all the w_0/a contained in Table I, and w_0 in fm. We assume the renormalization factors from the RI-SMOM scheme are 100% correlated between the local and one-link current on each lattice spacing. Further, for each independent analysis, we resample any priors used in the Bayesian fits, that is, we draw the central value from the prior distributions and assign this as the new prior central value. In each of these bootstrap samples, we obtain continuum results for each model. These continuum fits are performed using the statistical part of the data covariance matrix from the original (not resampled) dataset, as the statistical part of a resampled data covariance matrix is biased [90].

For two different observables a_μ^i and a_μ^j , under the assumption of disjoint and independent model spaces for the two observables, the BMA covariance is

$$\text{Cov}[a_\mu^i, a_\mu^j] = \sum_{m=1}^{N_{M_i}} \sum_{n=1}^{N_{M_j}} \text{Cov}_{mn}[a_\mu^i, a_\mu^j] \text{pr}(M_m^i|D) \text{pr}(M_n^j|D). \quad (3.14)$$

The covariance matrix $\text{Cov}_{mn}[a_\mu^i, a_\mu^j]$ contains the statistical and parametric covariances—estimated using bootstrap—given the selection of the specific models M_m^i for a_μ^i and M_n^j for a_μ^j . In specific cases where there is significant systematic correlation due to common model space, namely using the same model for correcting for finite-volume effects in light-quark observables, we adopt a conservative approach, assuming 100% model correlation. The treatment of this correlation adds the additional term

$$\text{Cov}[a_\mu^i, a_\mu^j] = \text{Cov}^{\text{stat}}[a_\mu^i, a_\mu^j] + \sigma_{a_\mu^i}^{\text{FV}} \sigma_{a_\mu^j}^{\text{FV}}, \quad (3.15)$$

where $\text{Cov}^{\text{stat}}[a_\mu^i, a_\mu^j]$ is estimated using Eq. (3.14) and $\sigma_{a_\mu^i}^{\text{FV}}$ is the contribution to the systematic uncertainty of a_μ^i that is associated with the spread of the model-based finite-volume correction. Equation (3.15) is used to account for correlations between $a_\mu^{l,W}(\text{conn.})$, $a_\mu^W(\text{disc.})$, and $\Delta a_\mu^{ud,W}(\text{SIB, conn.})$. Details and derivations of these covariance formulas are given in Appendix C.

We crosscheck our variances obtained from the bootstrap approach against Gaussian error propagation with GVAR [91]. In addition, we verify that any finite sample-size effects are beyond our level of precision by recomputing the correlations for different bootstrap sizes and observing stability in these results.

As a final note, the results for each observable obtained from the empirical Bayes procedure, described in Sec. III C can be compared with what we obtain from the corresponding BMA analyses when varying only the continuum fit functions. We find good consistency in the central values and errors reported from the two approaches, in line with the findings of Ref. [12].

IV. WINDOW OBSERVABLES

A. Light-quark connected

The light-quark connected contribution to $a_\mu^{\text{HVP,LO}}$ is approximately 85% and 70% of the total intermediate- and short-distance windows, respectively. Hence, the uncertainty on $a_\mu^{l,W}(\text{conn.})$ and $a_\mu^{l,\text{SD}}(\text{conn.})$ is a limiting factor on the uncertainty of the complete a_μ^W and

TABLE IV. Vector-current correlator datasets used in the calculation of $a_\mu^{ll}(\text{conn.})$. The first column lists the approximate lattice spacings in fm. The ensemble parameters are contained in Table I. The second and third (fourth and fifth) columns list the number of configurations and wall-sources analyzed for the local (one-link) current. The final column lists the number of eigenvector pairs per configuration. At $a \approx 0.15$ fm, the truncated solver method was employed but eigenvectors were not.

$\approx a/\text{fm}$	Local		One-link		N_{eig}
	N_{conf}	N_{src}	N_{conf}	N_{src}	
0.15	10019	48	9759	16	(TSM)
0.12	1060	64	1060	64	2000
0.09*	993	96	993	96	2000
0.06	1009	96	900	96	2000
0.04	313	144	256	144	2000

a_μ^{SD} observables. In this work, we update our previously published result for $a_\mu^{ll,W}(\text{conn.})$, which has a relative uncertainty of 0.5% [12]. This updated analysis includes new correlation function data sets, generated using low-mode-averaging on all ensembles but the coarsest (see Sec. II C). These newly generated correlation functions come with reduced statistical noise at large Euclidean times. However, we find that the new data also have better statistical precision at intermediate distances.

One of the significant sources of systematic uncertainty in the result of Ref. [12] was the mistuned light-quark mass on the 0.09 fm ensemble. To remedy this, we have generated correlation function data on the new 0.09* fm ensemble, which has a better tuned light-quark mass, yielding a pion mass within 0.5% of the physical value (see Table II). As a result, there now are no significant pion-mass corrections needed for the entire light-quark-connected data set, when we apply the lattice corrections. Another substantial source of uncertainty in the previous calculation was the continuum extrapolation. Here, in order to constrain the continuum limit better, we include correlation functions with a second vector-current discretization, the one-link (taste-singlet) vector current (Eq. (2.18b)), on all the ensembles. In addition, we include local and one-link data sets on an ensemble with a lattice spacing of 0.04 fm, the finest to date. We currently have fewer configurations on this ensemble, relative to the other ensembles at coarser lattice spacings. Nevertheless, the statistics is sufficient to significantly improve our continuum limit extrapolations for the two window observables considered here. Visually, the improved light-quark dataset is illustrated in Fig. 2 with the specific number of configurations, sources, and eigenvectors used in these datasets given in Table IV.

With these improved data, we follow the analysis strategy outlined above in Sec. III, which is similar to the strategy detailed in Ref. [12]. We consider a broad range of analysis variations, aiming to include *all* reasonable choices, and obtain the corresponding systematic uncertainty using BMA. We renormalize the respective vector-current operators with the $Z_V^{\text{RI-SMOM}}$ renormalization factors in Table III. This choice takes advantage of the complete and precise set of local and one-link RI-SMOM renormalization factors that are available from Ref. [53].

For the intermediate window observable, we create datasets corrected for finite-volume and mass-mistuning effects from the EFT-based correction schemes described in Sec. III B.

As already mentioned above, all the correlation functions included in our analysis are generated on well-tuned ensembles, so that quark-mass mistuning corrections are sub-leading. As a result, we are now able to ground all corrections for quark-mass mistuning directly in EFT. Consequently, we no longer employ the Hansen-Patella correction scheme, as it produces only finite-volume corrections. With the addition of a second current to our data set, we perform independent continuum limit extrapolations, as well as joint ones, to quantify the systematic uncertainty due to residual discretization effects. In the BMA language, these variations are performed by excluding the data for one of the two currents from the continuum extrapolations. Another consequence of including a second current in our data set is that we no longer include taste-breaking corrected data in our Bayesian model average. We do, however, still verify that datasets corrected for taste-breaking give consistent results in the continuum. As mentioned in the preceding section, we do not apply lattice corrections to the short-distance observables, because the effects are negligible, and the EFT-based correction schemes are well outside their ranges of validity.

After first verifying that independent continuum extrapolations of the local and one-link data agree, our analysis strategy is to include joint, correlated fits to both currents simultaneously. Because the leading discretization effects in the one-link and local currents differ from each other (see Appendix A), a combined fit gives us a strong handle on the continuum extrapolation of $a_\mu^H(\text{conn.})$. In this fit, the continuum extrapolated value of a_μ^H (a_μ in Eq. (3.6)) and the mass-mistuning coefficient C_{sea} in Eq. (3.7) are shared parameters.

The form of $F^{\text{disc.}}(a)$ for each observable is informed by theoretical expectations for the two currents, as well as the empirical Bayes procedure. In particular, the one-link current has leading a^2 discretization effects (Appendix A), so we do not include any leading α_s suppression. The empirical Bayes procedure provides guidance for the highest-order discretization terms that can be resolved by our datasets. For a_μ^W , this corresponds to an a^4 term in the fit function, while for a_μ^{SD} we find that an a^6 term is resolvable. In our analysis, we therefore consider continuum limit fit functions that include terms up to a^6 and a^8 for a_μ^W and a_μ^{SD} , respectively, in order to test for stability of the extrapolated results.

The functional forms of $F^{\text{disc.}}(a)$ in Eq. (3.6) for the local and one-link currents are then given by

$$F_{\text{local}}^{\text{disc.}}(a) = C_{a^2,n}(a\Lambda)^2 \alpha_s^n + \sum_{k=2}^4 C_{a^{2k}}(a\Lambda)^{2k}, \quad \text{where } n = \{0\}, 1, 2, \quad (4.1)$$

$$F_{\text{one-link}}^{\text{disc.}}(a) = \{C_{a^2 \log(a)}(a\Lambda)^2 \log(a\Lambda)\} + \sum_{k=1}^4 C_{a^{2k}}(a\Lambda)^{2k}, \quad (4.2)$$

where the terms representing the effects of log enhancement (*i.e.*, the terms within $\{\dots\}$) are included *only* for extrapolations of the short-distance observable. Applying the empirical Bayes procedure for both currents independently and simultaneously, we find the following consistent results for Λ ,

$$\Lambda_{l,\text{SD}} = \Lambda_{l,W} = 0.6 \text{ GeV}. \quad (4.3)$$

We label fit functions with $C_{a^6} = 0$ as “quadratic,” fit functions with $C_{a^8} = 0$ as “cubic,” and fit functions with all terms listed in $F^{\text{disc.}}(a)$ as “quartic.” Given the additional data point at 0.04 fm, as well as the second current, our continuum extrapolation fit function variation basis has expanded from Ref. [12]. With the constraint that we do not perform

fits with zero degrees of freedom or less, we now include variations where we drop the two coarsest spacings, not just the single coarsest. Due to the lower statistics at 0.04 fm, we also include variations for $a_\mu^{ll,W}(\text{conn.})$ where this ensemble is dropped. Aside from the variations, discussed above, where we drop one of the two currents completely, we restrict our variations to ones in which the ensembles are dropped for both currents simultaneously.⁹

For a_μ^{SD} , as indicated in Eqs. (4.1) and (4.2), we include an extra subset of fit variations with leading a^2 for the local current and include a leading $a^2 \log(a)$ for the one-link current due to the short-distance log-enhancement effects discussed in Appendix A. We crosscheck this theoretical expectation in our empirical Bayes analysis. Specifically, for the one-link current, the data prefer a fit function that includes the log-enhanced term. Without it, the fit quality, as measured by the $\chi^2/\text{d.o.f.}$, is poor, and the continuum limits of the one-link and local current data are in tension with each other. In contrast, for the local-current a_μ^{SD} data, the empirical Bayes fits prefer a fit function without the log-enhanced term.

In summary, our Bayesian model average incorporates the following analysis variations:

- **Finite-volume and mass-mistuning correction (a_μ^{W} only):** All correction schemes discussed above: χPT (NLO and NNLO), CM, and MLLGS. We always correct both currents using the same scheme. In the case of MLLGS, we do not perform extrapolations with the coarsest, 0.15 fm, data point as discussed in Sec. III B.
- **Correction region (a_μ^{W} only):** We include a variation on the corrections where they are computed from the range [0.7, 1] fm instead of over the full W window interval. The reasoning for this is discussed in Ref. [12].
- **Continuum fits:** We perform continuum extrapolations using all fit function variations described above, including fits to the three and four finest ensembles, and four coarsest ensembles (a_μ^{W} only). Also included are fits that drop one of the two currents entirely.¹⁰

The result of applying the BMA procedure, with these variations, for $a_\mu^{ll,W}(\text{conn.})$ is shown in Fig. 5. The top-right panel illustrates the continuum extrapolations using data corrected with CM computed from the full window. The dashed lines indicate the continuum extrapolations for each data set. In total, we include six hundred forty fit results in the Bayesian model average. The resulting distribution is shown in the top left panel of Fig. 5, where it is overlaid on the BMA result (red line and bands) obtained using Eqs. (3.10) and (3.11). The middle panel shows the results from all the individual fits, ordered by the model probability, in comparison with the BMA result (red line and bands), while the bottom panel gives the associated Q values computed from χ_{aug}^2 (see Eq. B.4 of Ref. [92]). We find that fits with higher Q values tend to have the larger model probabilities.

Following Ref. [12], we also perform the Bayesian model averages on specific subsets of the analysis variations. That is, we fix one of the analysis choices but vary the rest as usual. The results of these subset averages for $a_\mu^{ll,W}(\text{conn.})$ are shown in Fig. 6 (left). The top data point

⁹ We have verified that including variations where different data points are dropped for the different currents gives a completely consistent final BMA central value and uncertainty.

¹⁰ We adjust the model priors, $\text{pr}(M)$, of these variations so that they are equal for each current subset, which accounts for the fact that there are more variations for the local-current fits, due to different powers of n in the leading $a^2 \alpha_s^n$ term.

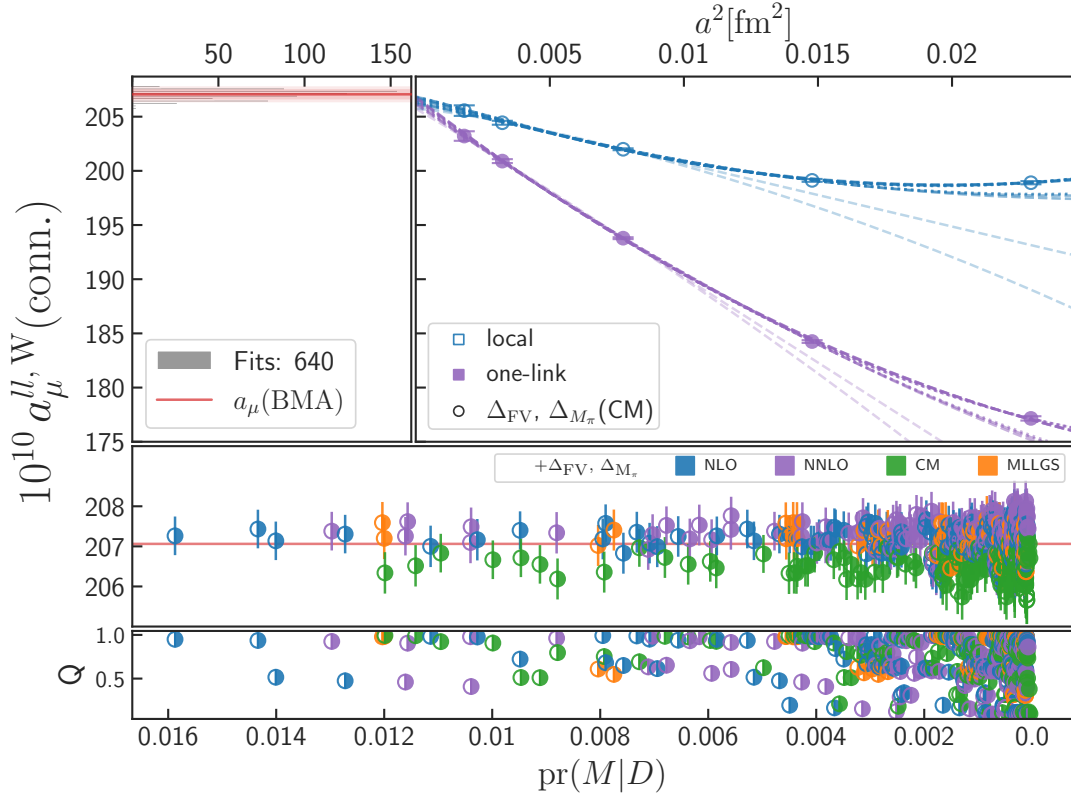


FIG. 5. Results of the BMA procedure applied to $a_\mu^{ll, W}(\text{conn.})$. *Upper left panel*: Histogram of all continuum extrapolations used in the BMA, the inner light-red band corresponds to the first term in Eq. (3.11), while the outer is the total error. *Upper right panel*: The subset of data sets and extrapolations corresponding to correcting the local (blue unfilled) and one-link (purple filled) currents with the CM. Different extrapolations correspond to variations of the fit function and ensembles included. *Lower panels*: The best fits according to the model probability, Eq. (3.12). The middle panel shows the joint-fit results, while the bottom one shows the corresponding Q values [92]. In both panels, the correction schemes employed for Δ_{FV} and Δ_{M_π} are indicated by the symbols' color, according to the legend in the middle panel.

is the BMA result from Fig. 5. The four following data points correspond to model subsets for the lattice corrections that are separately limited to each of the four schemes (NLO χ PT, NNLO χ PT, CM, MLLGS). We find tension between the CM scheme and the others, which yields a significant contribution to the systematic uncertainty in our full BMA result. The next three points correspond to model subsets that either do or do not include one of the two currents in the extrapolation, with joint fits including both. We find that these results are in strong agreement with each other, with a gain in precision from performing the joint fits. The following fourteen data points are subsets of the continuum extrapolation where the highest order discretization term is varied, and specific lattice spacings are dropped. We specify these subsets for the local current with unfilled symbols and the one-link current with filled symbols. Here, dropping our two coarsest ensembles or the finest results in the most variation. The next two data-points break the fit function basis into two subsets based on if the mass-mistuning term is included or not. The results here are consistent for these variations. Finally, we split the fit function basis into fits with different leading powers of α_s . We find the BMA does not significantly discern among the powers of α_s in the leading term

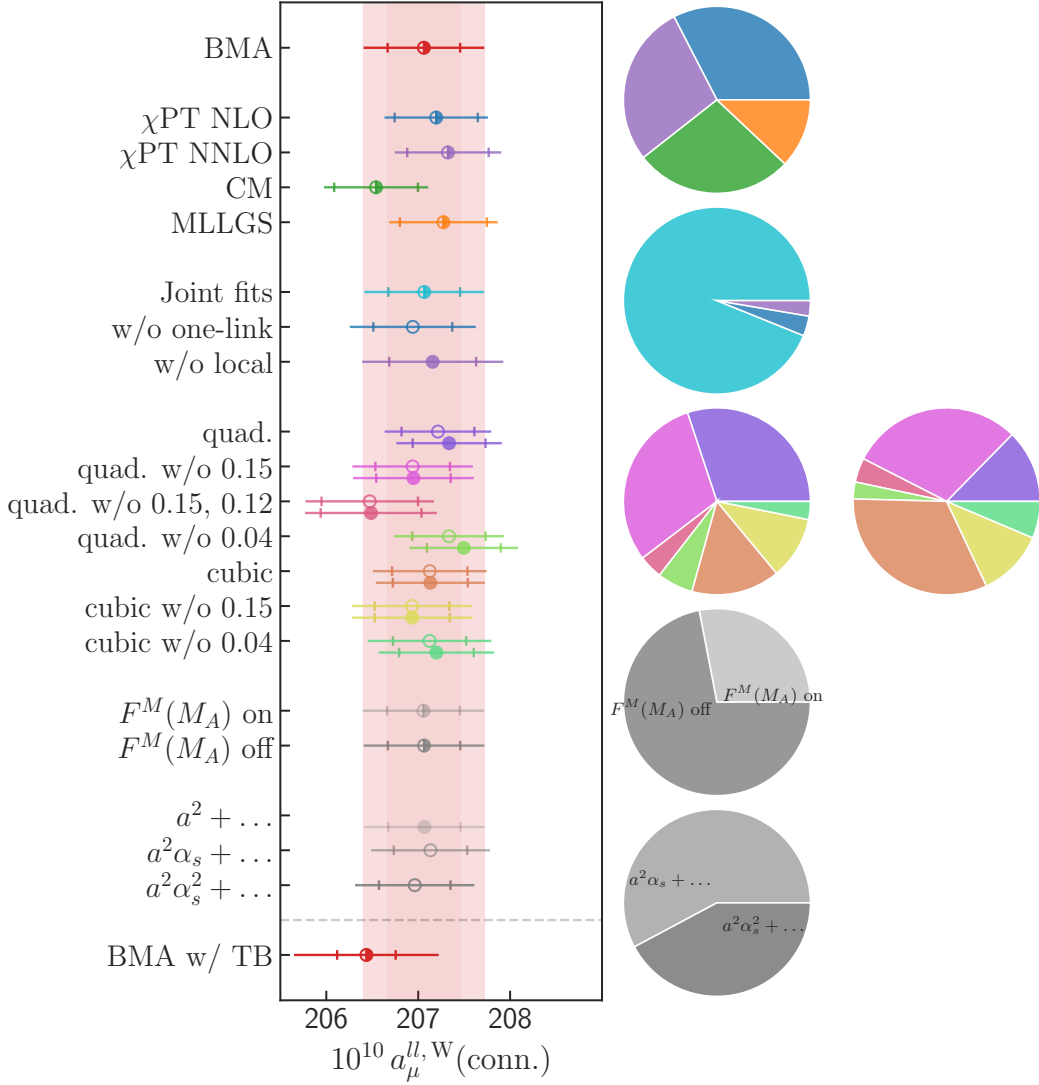


FIG. 6. Breakdown of the results from the BMA applied to $a_{\mu}^{ll,W}(\text{conn.})$. *Left panel*: From top to bottom, the first, main result (BMA) includes all data sets, schemes, and other variations. The next block of results are the schemes for finite-volume and pion mass corrections. The following three are continuum extrapolations where either neither or one of the two currents is dropped. The next fourteen are subsets with specific continuum fit functions, corresponding to quadratic and cubic, as well as omitting various subsets of the 0.15 fm, 0.12 fm or 0.04 fm ensembles. The unfilled circles correspond to the local current, the filled to the one-link current. The next two correspond to continuum fits with or without the mass-mistuning term. The penultimate three are subsets with differing leading powers of α_s in the fit function where, again, unfilled symbols are the local current and the filled symbols are one-link. Finally, below the dashed line, not included in the final BMA result, is the value one obtains if the model space is doubled by adding the original variations but with the corresponding taste-breaking corrections. The inner error bars on the data points correspond to the first term in Eq. (3.11), while the outer is the total error. *Right panels*: Pie charts showing the contributions to the BMA corresponding to the breakdowns in the left panel. The percentages are computed from Eq. (3.13) for the particular subsets. In the case of the continuum fit function subsets, which are broken up into local and one-link current variations, the left pie-chart corresponds to the local current and the right to the one-link.

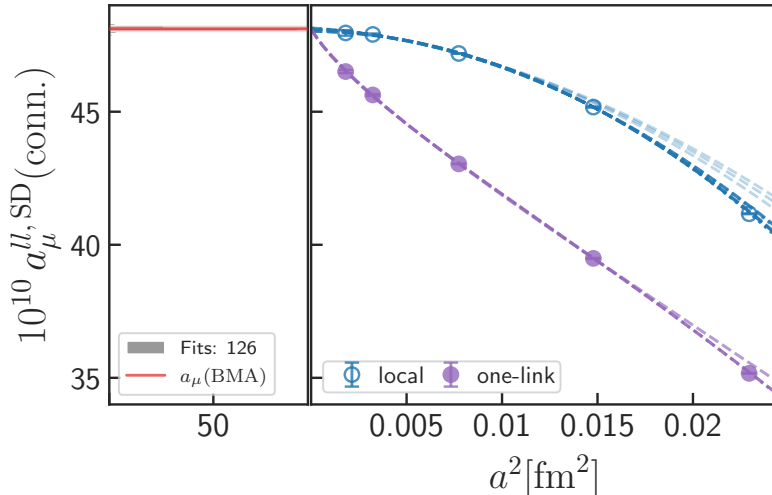


FIG. 7. Results of the BMA procedure applied to $a_\mu^{ll,SD}(\text{conn.})$. *Left panel:* Histogram of all continuum extrapolations used in the BMA, the light-red band is the BMA result. *Right panel:* The subset of data sets and extrapolations corresponding to the two different currents.

for the local current (unfilled circles). Below the dashed line we include the result obtained by performing all the variations described above and, in addition, including corresponding variations for each model including taste-breaking corrections, *i.e.*, increasing the size of the model space by a factor of two. We find this result is consistent with our final BMA result.

The relative probabilities of these subsets, as defined in Eq. (3.13), are shown in Fig. 6 (right). The top pie chart shows that the correction schemes have roughly equal weight in the BMA, with MLLGS being smaller than the others. This is due to the fact that the number of models with MLLGS corrections is smaller as we do not include variations where the coarsest data point is included, as discussed above. The second pie chart from the top shows the subset probabilities for performing either joint extrapolations or dropping one of the two currents. We see a strong preference for performing the joint extrapolations, largely due to the penalty incurred from dropping the five data points, which corresponds to the full current that is dropped. The third and fourth pie charts, on the same row, indicate that quadratic continuum fit functions are preferred for the local current whereas cubic fit functions are preferred by the one-link current, likely due to the significantly larger discretization effects in the one-link current. In the following pie charts, we observe a preference for continuum fits where the mass-mistuning term is switched off, again due to the penalty incurred in the BAIC for the additional fit parameter. Finally, in the last pie chart, we see a slight preference for a leading power of α_s for the local current.

The result of applying the BMA to $a_\mu^{ll,SD}(\text{conn.})$ is shown in Fig. 7. Here, we plot all the joint continuum extrapolations to the two current dataset. In total, there are one hundred twenty-six models in our BMA corresponding solely to continuum fit function variations. As expected, the short-distance window has much larger discretization effects than W. In particular, the one-link current has a leading a^2 discretization effect, which leads to a logarithmic enhancement, as discussed in Appendix A. Due to these large discretization effects, some fit functions without higher order terms are heavily suppressed in the Bayesian model average. This can be seen in the second and third pie-charts in Fig. 8 where the quadratic fit function is insufficient in capturing the curvature over all five ensembles. In this window, we find significant improvement when performing joint fits as opposed to fits where one of

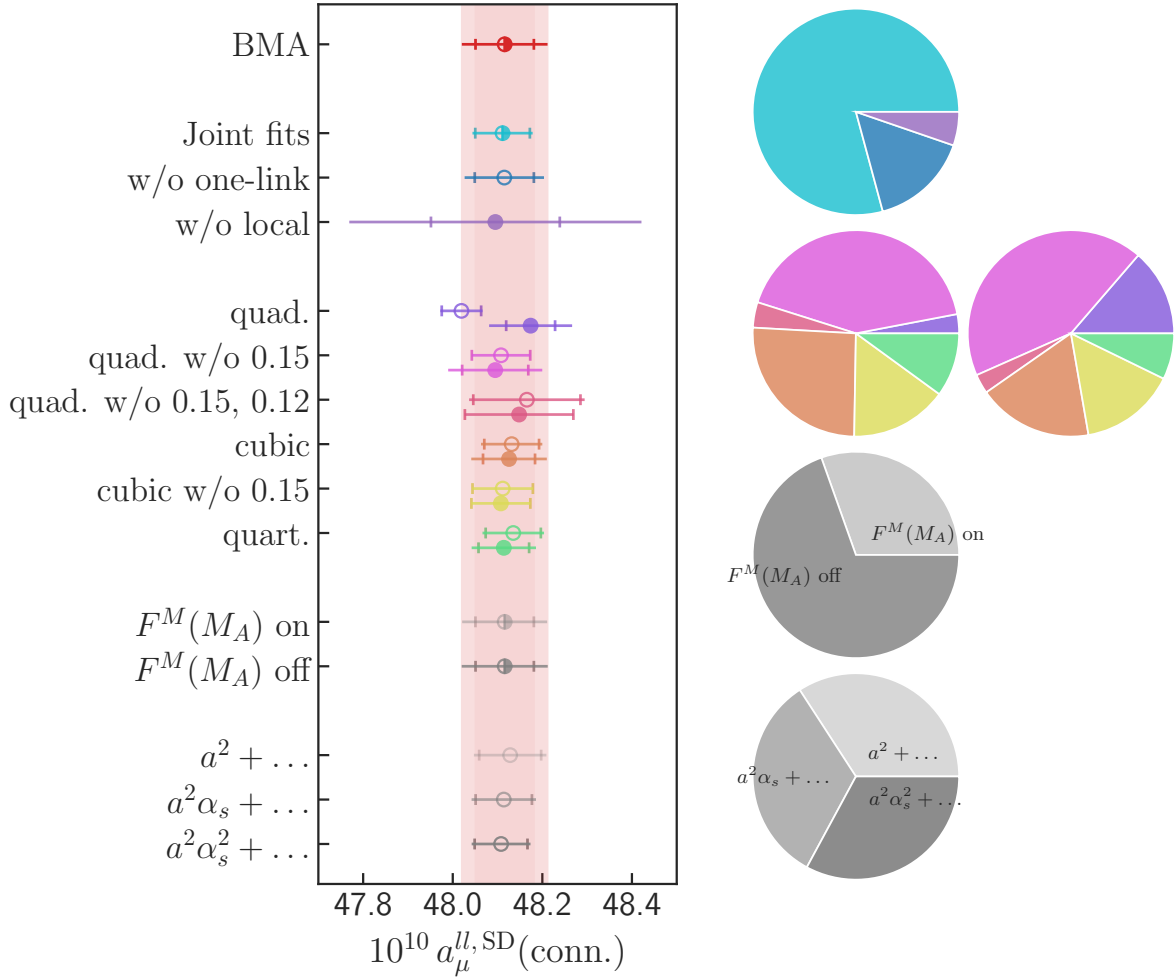


FIG. 8. Breakdown of the results from the BMA applied to $a_\mu^{ll,SD}(\text{conn.})$ (see caption of Fig. 6 for a description of the figure).

the two currents is dropped. The differing leading discretization effects seem to constrain the continuum result significantly. On the other hand, the fits to just the one-link current result in a very large uncertainty due to the leading $a^2 \log(a)$ dependence. All other fit function variations are reasonably consistent with each other. However, we do observe a large increase in uncertainties when dropping the two coarsest spacings. Finally, we find that the BMA shows no preference for the power of α_s in the leading term of the local current fit function. Other than slightly larger errors in the leading a^2 fits, we see almost exactly equal results and subset probabilities.

Our final determinations of $a_\mu^{ll,SD}(\text{conn.})$ and $a_\mu^{ll,W}(\text{conn.})$ are given in Sec. V, specifically Eqs. (5.1) and (5.9), with complete error budgets given in Tables VIII and IX. We compare these results with previous determinations in Figs. 24 and 25, respectively.

B. Strange and charm

As discussed in Sec. II A, the strange- and charm-quark connected contributions to $a_\mu^{\text{HVP,LO}}$ are the next-largest after the light-quark connected in the short- and intermediate-

TABLE V. Vector-current correlator datasets used in the calculation of the $a_\mu^{ss}(\text{conn.})$ and $a_\mu^{cc}(\text{conn.})$ contributions to the SD and W windows. The first column lists the approximate lattice spacings in fm. The parameters for these ensembles are contained in Table I. The second column lists the number of independent configurations analyzed after binning, as discussed in Sec. II C. The third column lists the number of random-wall source solves per configuration.

$\approx a/\text{fm}$	N_{conf}	N_{src}
0.15	1001	48
0.12	298	64
0.09*	252	48
0.06	158	24

distance windows. Specifically, as can be seen in Fig. 1, the charm contribution is the second largest in the SD window while the strange contribution is the second largest in the W window. In fact, almost all the charm contribution is contained in SD, with W containing only a contribution from the long-distance tail of the charm-quark vector-current correlation function. Fortunately, the strange and charm correlation functions do not suffer from the same signal-to-noise issues in the tail as the light-quark contribution does. Additionally, the effects of finite volume and taste-breaking are negligible at the level of precision we require. Hence, the analysis of these two contributions is much simplified compared with observables that contain light quarks.

Our strange and charm datasets are obtained using the local current and have equivalent statistics, with the specific numbers of configurations and sources used in the analysis given in Table V. All ensembles have tuned masses within 0.5% of the physical light, strange, and charm mesons in Sec. II B, as can be seen from Table II. The strange and charm local vector currents are renormalized with both sets of factors ($Z_{V,\text{local}}^{\text{FF}}$, $Z_{V,\text{local}}^{\text{RI-SMOM}}$) given in Table III. The two renormalizations have different discretization errors but should yield consistent results in the continuum limit. Because discretization errors can be a more significant source of uncertainty for the heavier flavors, we use both renormalization schemes in our strange and charm analysis to improve control over the continuum limit extrapolation. The observables $a_\mu^{ss,\text{SD}}(\text{conn.})$, $a_\mu^{ss,\text{W}}(\text{conn.})$, $a_\mu^{cc,\text{SD}}(\text{conn.})$, and $a_\mu^{cc,\text{W}}(\text{conn.})$ are computed on each ensemble. We perform continuum extrapolations with the local continuum fit function $F_{\text{local}}^{\text{disc.}}$ (Eq. (4.1)) in Eq. (3.6). For the charm extrapolations, we modify the mass mistuning term $F^M(M_A)$ (Eq. (3.7)) with

$$F_{\text{charm}}^M(M_A) = F^M(M_A) + C_{\text{charm}} \frac{M_{D_s, \text{phys.}} - M_{D_s, \text{latt.}}}{M_{D_s, \text{phys.}}} \quad (4.4)$$

to account for mistuning of the charm-quark mass. The values of the D_s mass on each ensemble are given in Table II. We use a Gaussian prior of $C_{\text{charm}} = 0(1)$, following Ref. [61]. From our empirical Bayes procedure we find

$$\Lambda_{ss,\text{SD}} = \Lambda_{ss,\text{W}} = 0.65 \text{ GeV}, \quad (4.5)$$

$$\Lambda_{cc,\text{SD}} = \Lambda_{cc,\text{W}} = 1.3 \text{ GeV}. \quad (4.6)$$

We also find that the charm data are sensitive to higher order discretization terms (a^6 , a^8) while strange data are not. As before, we limit our continuum fit variations to ones in

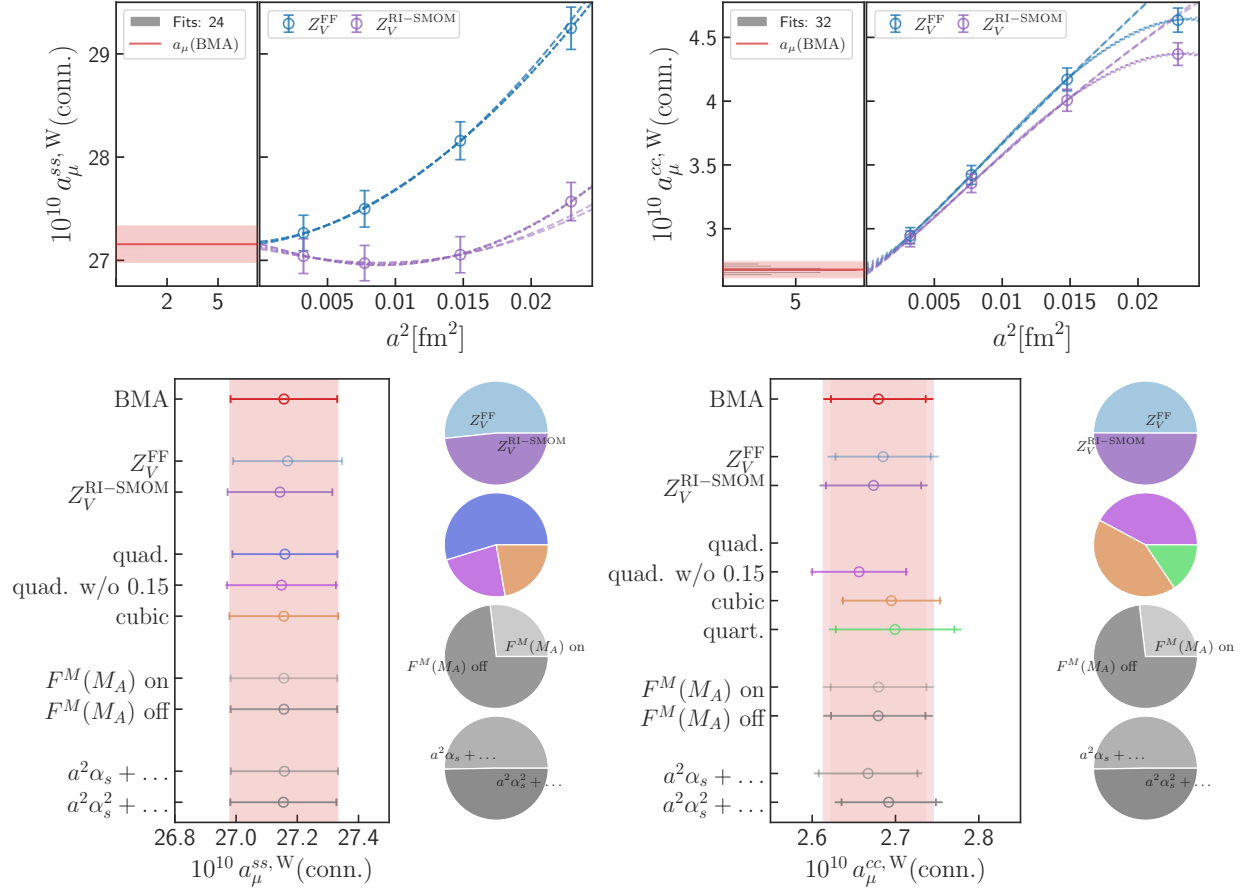


FIG. 9. Results of the BMA procedure applied to $a_\mu^{ss,W}(\text{conn.})$ (left) and $a_\mu^{cc,W}(\text{conn.})$ (right), respectively. *Upper plots, right panels*: All continuum extrapolations used in the BMA for the respective observables. *Upper plots, left panels*: Histogram of all continuum results. The red line and bands are the corresponding BMA result, where the inner light-red band corresponds to the first term in Eq. (3.11), while the outer is the total error. *Lower plots, left panels*: Breakdown of BMA result into model subsets. From top to bottom, the main BMA result, containing all variations. After, the two data subsets using the two local-current renormalization factors in Table III. The next group are subsets using specific continuum fit functions: quadratic, quadratic without the 0.15 fm data point, or cubic. The quadratic data point for $a_\mu^{cc,W}(\text{conn.})$ is outside the range of the x-axis. For this contribution, we also include a quartic variation. The final two data points are subsets with differing leading powers of α_s in the fit function. The inner error bar on the data points corresponds to the first term in Eq. (3.11), while the outer is the total error. *Lower plots, right panels*: Pie charts show the relative contributions to the BMA corresponding to the breakdowns in the left panel. The percentages are computed by summing over Eq. (3.12) for the particular subsets, as in Eq. (3.13).

which the degrees of freedom are non-negative, using the prior of Eq. (3.9) when necessary to regulate the degrees of freedom.

The results of these continuum extrapolations are shown in Fig. 9 for $a_\mu^{ss,W}(\text{conn.})$ (top left) and $a_\mu^{cc,W}(\text{conn.})$ (top right). For $a_\mu^{ss,W}(\text{conn.})$, in the right panel, twelve continuum fit variations are performed for the two choices of renormalization factor given in Table III.

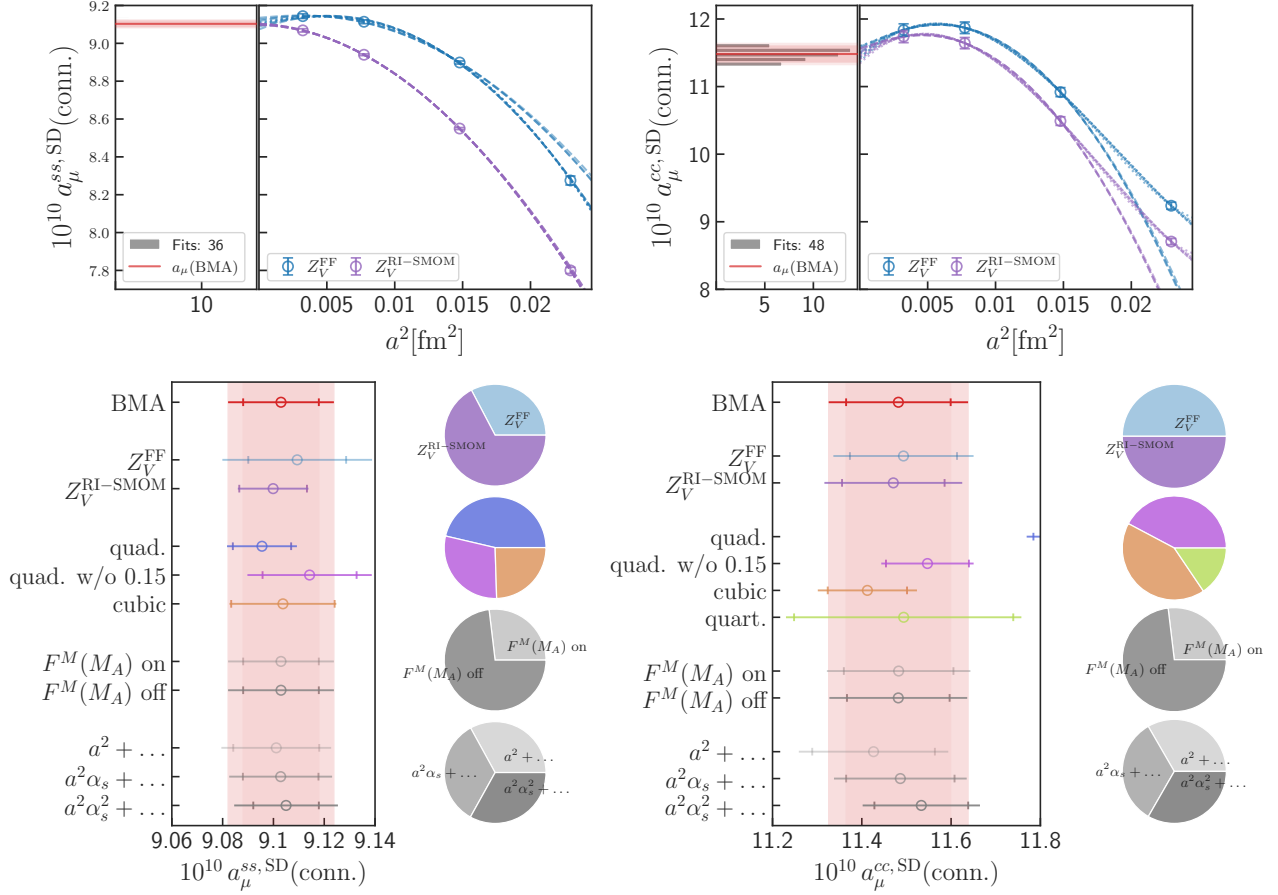


FIG. 10. Results of the BMA procedure applied to $a_\mu^{ss,SD}(\text{conn.})$ and $a_\mu^{cc,SD}(\text{conn.})$, respectively. See caption of Fig. 9 for a description of each plot.

The histogram of the fit central values is shown in the left panel with the BMA mean and errors, Eqs. (3.10) and (3.11), given by the red line and inner- (first term in Eq. (3.11)) and outer-bands (total error). Here, the error is dominated by the first term in Eq. (3.11); hence, only the inner band is visible. In the bottom left plot of Fig. 9, the models are broken up into labeled BMA subsets. We find these subsets are all consistent with our full BMA result (red). For $a_\mu^{cc,W}(\text{conn.})$, Fig. 9 (top right), we have sixteen fit variations (four additional variations from including the C_{a^2} term). We observe that the charm data have additional curvature compared with $a_\mu^{ss,W}(\text{conn.})$ over the range of lattice spacings we compute. And indeed, we find that fit variations with just quadratic terms are not enough to capture this curvature. This can be seen in Fig. 9 (bottom right), where the quadratic models subset value appears off the plot. From the corresponding pie chart on the right, we observe that BMA suppresses the contribution from this subset, indicating very poor fit quality. Aside from this, all other model variation subsets are in good agreement with our BMA result. The consistency of the quartic subset of fits with everything else indicates that we have stability with respect to adding higher order terms.

Continuum extrapolation results for $a_\mu^{ss,SD}(\text{conn.})$ and $a_\mu^{cc,SD}(\text{conn.})$ are shown in Fig. 10, (top left) and (top right), respectively. The total fit variations are increased for both strange and charm over the W case due to the inclusion of variations with a leading a^2 term, as in the

TABLE VI. One-link current correlator datasets used in the calculation of the disconnected contribution to a_μ^{SD} and a_μ^{W} . The first column lists the approximate lattice spacings in fm. The parameters for these ensembles are contained in Table I. The disconnected correlator data for the coarsest two ensembles are the result of combining two data sets, each analyzed at the outset by separate groups of authors. The second column lists the number of independent configurations analyzed by each group, respectively. The third column lists the number of volume random sources per configuration, while the fourth column gives the number of eigenvectors. One data set employs eigenvectors; the other, indicated by the –, does not.

$\approx a/\text{fm}$	N_{conf}	N_{src}	N_{eig}
0.15	645, 1047	256, 256	350, –
0.12	150, 562	500, 256	300, –
0.09	705	1000	1000

case of the light quark, to test for any log-enhancement effects. As before, we find additional curvature in the charm contribution over the strange. In Fig. 10 (bottom), the breakdown of these extrapolations into labeled BMA subsets is given. We find that for $a_\mu^{ss,\text{SD}}(\text{conn.})$ (left) we have consistent results for all model subset variations, with the quadratic fits to the full dataset being preferred by the BMA. We also see no preference for the power of α_s . For $a_\mu^{cc,\text{SD}}(\text{conn.})$ (right), as in the case of $a_\mu^{cc,\text{W}}(\text{conn.})$, we find that quadratic fits are insufficient to capture the curvature of the full dataset. Outside this particular set of fits, we observe some spread in the remaining variations, though all are statistically consistent with each other and encapsulated by the BMA uncertainty.

Our final determinations of $a_\mu^{ss,\text{SD}}(\text{conn.})$, $a_\mu^{cc,\text{SD}}(\text{conn.})$, $a_\mu^{ss,\text{W}}(\text{conn.})$ and $a_\mu^{cc,\text{W}}(\text{conn.})$ are given in Sec. V, specifically Eqs. (5.2), (5.3), (5.10), and (5.11), with complete error budgets given in Tables VIII and IX. We compare these results with previous determinations in Figs. 24 and 25, respectively.

C. Disconnected

For the disconnected contribution, our dataset spans only our three coarsest lattice spacings (see Fig. 2), which leads to two technical complications. First, MLLGS is not usable at the coarsest spacing (see Sec. III B), so we exclude it from our set of correction schemes. Second, being limited to three spacings constrains the continuum-limit-extrapolation variations, which we usually take to be at least quadratic and hence have three parameters at minimum. A taste-singlet current is necessarily employed, hence we use the one-link discretization, Eq. (2.18b), along with the renormalization factor $Z_{V,\text{one-link}}^{\text{RI-SMOM}}$ from Table III. We also use no mass-mistuning term, as we found the extra parameter to destabilize fits with only three data points. Ensembles and corresponding statistics are given in Table VI.

For $a_\mu^{\text{W}}(\text{disc.})$, we perform FV, M_π , and TB corrections as described in Eqs. (3.3)–(3.5) of Sec. III B. To avoid mixing models, we do not employ the HP scheme for FV corrections. We therefore consider only the CM scheme along with NLO and NNLO χPT . The empirical Bayes procedure described in Sec. III yields

$$\Lambda_{\text{disc.,W}} = 0.9 \text{ GeV}. \quad (4.7)$$

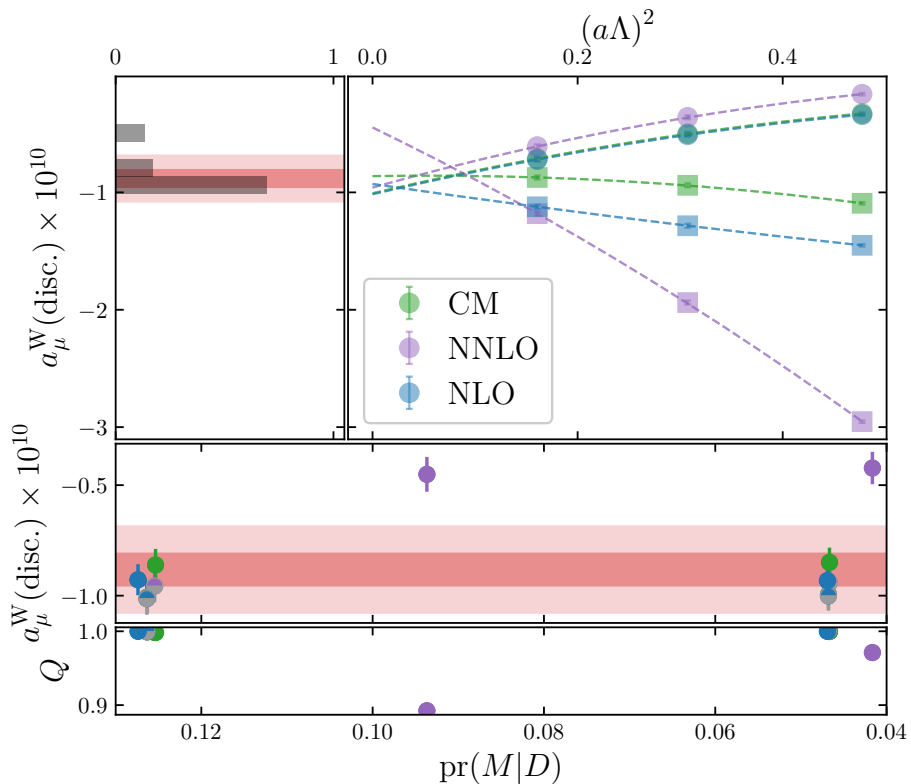


FIG. 11. Results of the BMA procedure applied to the disconnected contribution in the intermediate window with 12 models in total. The final BMA result is shown in light red, where the inner and outer bands correspond to the error coming from the first term in Eq. (3.11) and the total error, respectively. *Upper left panel*: Histogram of $a_\mu^{\text{W}}(\text{disc.})$, weighted by $\text{pr}(M|D)$. These results come from the bootstrap, carrying out fits in each sample. *Upper right panel*: Continuum-limit extrapolations. Data without TB corrections are indicated with circles, while data with TB corrections are indicated with squares. *Middle panel*: Results of the continuum fits for individual models going into the BMA, plotted against their model weight. Models without TB corrections are gray in the lower half of their symbols. *Lower panel*: Goodness of fit Q computed from χ_{aug}^2 plotted against the model weight.

We observe that our dataset cannot significantly resolve terms beyond the leading a^2 for $a_\mu^{\text{W}}(\text{disc.})$. Hence, our continuum fits Eq. (3.6) utilize

$$F_{\text{discon.}}^{\text{disc.}}(a) = \sum_{k=1}^3 C_{a^{2k}} (a\Lambda)^{2k}, \quad (4.8)$$

and we introduce the prior Eq. (3.9) on all higher order discretization terms.

We do not include any lattice corrections in the short-distance window, following the reasoning at the end of Sec. III B. We find that the data in this window are highly non-monotonic, which makes it challenging to assign reasonable priors. Hence, we use Eq. (4.8) with $k = 1$ and $k = 2$. When $k = 1$ we carry out “solves,” *i.e.*, zero degree of freedom parameterizations, to the finest two and coarsest two points, along with a fit to all three.

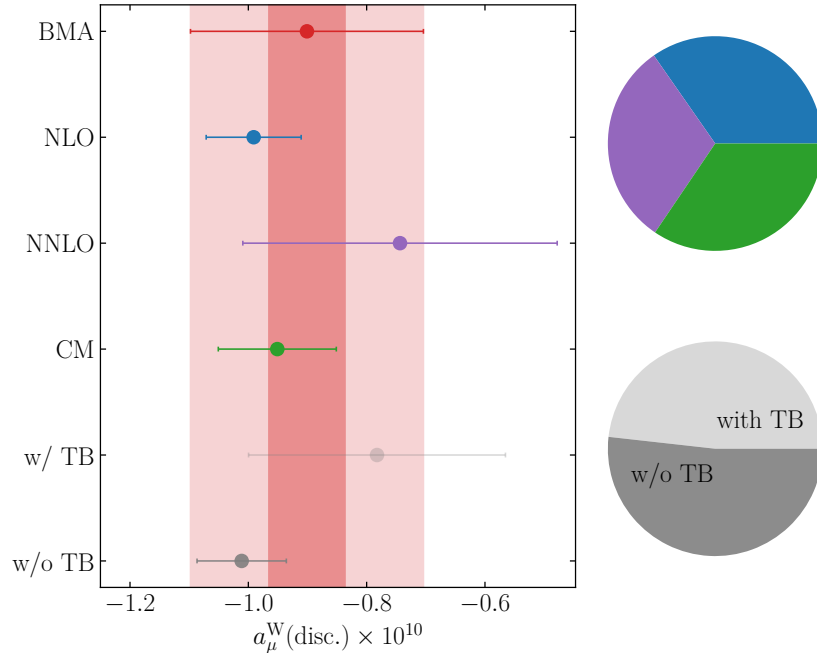


FIG. 12. Breakdown of the results from the BMA applied to $a_\mu^W(\text{disc.})$. This breakdown is done in the same manner as Fig. 6.

When $k = 2$ we solve for all three. Rather than using BMA, we take the difference between extreme results as a conservative systematic uncertainty, while the spread of the central value over the bootstrap bins is used for the statistical uncertainty.

Our BMA procedure applied to $a_\mu^W(\text{disc.})$ is shown in Fig. 11. The BMA runs over the models, NLO, NNLO, and CM, and for each model, over quadratic and cubic Ansätze, with and without taste breaking, which yields a total of 12 models. We see that most extrapolations are in good agreement, except for NNLO with TB. These extrapolations tend to increase the model spread, and correspondingly, we see that our final uncertainty has a considerable systematic component, represented in light red.

Ultimately, the influence of our NNLO points with TB is attenuated by the fact that they represent only two of twelve models along with a slightly smaller model weight, represented both in the histogram of Fig. 11 and in the gray pie chart of Fig. 12.

Our procedure for computing $a_\mu^{\text{SD}}(\text{disc.})$ is illustrated in Fig. 13.¹¹ The extreme values used to estimate our systematic error come from the linear solve to the coarsest two spacings and the quadratic solve to all three, which can be seen in the left plot. The motivation for this conservative estimate lies in the interplay between the SD window function and the behavior of the disconnected correlator. In particular, as t/a crosses the SD window boundary, the disconnected correlator sharply varies from positive to negative. As a result, due to the ensembles used in this work, there are significant discretization effects. This

¹¹ As mentioned earlier, we do not treat the extrapolation of $a_\mu^{\text{SD}}(\text{disc.})$ as an expansion about the continuum value. Therefore, we are unable to enforce any sensible priors on the discretization terms, and hence, the fits are insensitive to the choice of Λ . Nevertheless, we take $\Lambda_{\text{disc.,W}}$ from Eq. (4.7) as our preferred choice to scale the abscissa in this figure, keeping it consistent with Fig. 11.

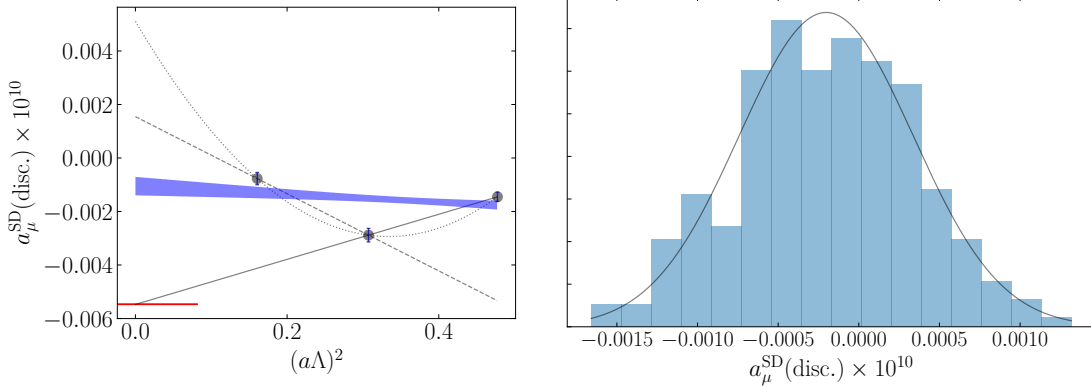


FIG. 13. Results for $a_\mu^{\text{SD}}(\text{disc.})$. *Left panel*: Three solves and a linear fit in the original data set. The midpoint between the extreme results in the continuum limit is taken as an estimate of our central value, and half the spread between the extreme results is taken as an estimate of the systematic error. The red line gives the pQCD prediction, Eq. (4.23). *Right panel*: Histogram of bootstrap results for the central value. A Gaussian with mean and standard deviation taken to be the median and half the difference between the limits of the middle 68% region of the histogram is shown in black for comparison.

is further complicated due to the presence of the oscillating terms in staggered correlation functions; whether there is an “up-” or “down-” oscillation at the window boundary varies for each lattice. This is likely the source of the observed nonmonotonicity in $a_\mu^{\text{SD}}(\text{disc.})$, and without understanding in detail how this interplay is resolved at finer spacings, it is difficult to model the continuum behavior.

The pQCD prediction of Eq. (4.23) is consistent within this large systematic. In the right plot, we see the spread of midpoints coming from the procedure in the left plot carried out in each bootstrap sample. For this observable, the systematic uncertainty dwarfs the statistical uncertainty. Calculations at finer lattice spacings are needed to clarify the continuum-limit behavior of this observable.

Our final determinations of $a_\mu^{\text{SD}}(\text{disc.})$ and $a_\mu^{\text{W}}(\text{disc.})$ are given in Sec. V, specifically Eqs. (5.4) and (5.12), with complete error budgets given in Tables VIII and IX. We compare these results with previous determinations in Figs. 24 and 25, respectively.

D. Strong-isospin breaking

The strong-isospin breaking (SIB) correction can be broken up into connected and disconnected contributions:

$$\Delta a_\mu^{ud}(\text{SIB}) = \Delta a_\mu^{ud}(\text{SIB, conn.}) + \Delta a_\mu^{ud}(\text{SIB, disc.}). \quad (4.9)$$

These observables come from different datasets, as shown in Fig. 2. Specific numbers of configurations and sources are given in Table VII. The connected SIB-correction dataset is generated using the local vector current, whereas the disconnected-contribution dataset uses the one-link (taste-singlet) current; the local (one-link) vector currents are renormalized with $Z_{V, \text{local}}^{\text{FF}}$ ($Z_{V, \text{one-link}}^{\text{RI-SMOM}}$) given in Table III. The differences in these datasets lead to different

TABLE VII. Vector-current correlator datasets used in the calculation of $\Delta a_\mu^{ud}(\text{SIB})$. The first column lists the approximate lattice spacings in fm. The ensemble parameters are contained in Table I. The second through fourth (sixth through eighth) columns list the valence quark flavors, the number of configurations and wall-sources (volume-sources) analyzed for the local (one-link) current used in the $\Delta a_\mu^{ud}(\text{SIB, conn.})$ ($\Delta a_\mu^{ud}(\text{SIB, disc.})$) analysis, respectively. The fifth column lists the number of eigenvector pairs per configuration where applicable for the local current. Here, † indicates that the truncated solver method was employed, and no eigenvectors were used.

$\approx a/\text{fm}$	qq	Connected (local)			Disconnected (one-link)		
		N_{conf}	$N_{\text{src}}^{\text{wall}}$	N_{eig}	qq	N_{conf}	$N_{\text{src}}^{\text{volume}}$
0.15'	$uu/ll/dd$	4949	48†	–	–	–	–
0.15	$uu/ll/dd$	10019	48†	–	ud	1047	256†
					ll	1692	
0.12	$uu/ll/dd$	9637	64†	–	ud/ll	712	500†
0.09	$ll/rr/dd$	1000	48	2000	ud/ll	705	1000†
0.09*	$hh/ll/dd$	993	96	2000	–	–	–
0.06	ll	2858	24†	–	–	–	–

analysis strategies for each observable. Here, we describe each of these analyses in both W and SD windows. The SIB correction is a low-energy effect with about 90% coming from $t \geq 1$ fm, 10% from the W window, and almost nothing from the SD window.

Our final determinations of $\Delta a_\mu^{ud,SD}(\text{SIB, conn.})$, $\Delta a_\mu^{ud,SD}(\text{SIB, disc.})$, $\Delta a_\mu^{ud,W}(\text{SIB, conn.})$, and $\Delta a_\mu^{ud,W}(\text{SIB, disc.})$ are given in Sec. V—specifically Eqs. (5.5), (5.6), (5.13), and (5.14), respectively—with complete error budgets for the W and SD observables in Tables VIII and IX, respectively. A comparison of $\Delta a_\mu^{ud,W}(\text{SIB, conn.})$ and $\Delta a_\mu^{ud,W}(\text{SIB, disc.})$ with previous results from other groups is given in Fig. 26.

1. Connected strong-isospin breaking

The connected SIB dataset is obtained using the local current (see Table VII). These data span four lattice spacings in [0.06, 0.15] fm across six ensembles and are evaluated at various isospin-symmetric light-pion masses; these masses are given in Table II. The data on the 0.15 fm, 0.15' fm, and 0.12 fm ensembles are tuned near the physical uu , ll , and dd values, as defined in Sec. II B. The 0.09 fm ensemble includes the mistuned (unitary) and retuned light mass values discussed in Ref. [12] (labeled ll and rr , respectively) as well as a physical dd point. The 0.09* fm ensemble includes nearly-physical ll and dd values and a point at the harmonic-mean-square mass hh defined in Sec. II C. The unphysical-mass points on the 0.09 fm ensembles help constrain the mass dependence of the chiral-continuum extrapolation. The 0.06 fm ensemble is evaluated only at a nearly physical ll point, which helps constrain the lattice-spacing dependence of the chiral-continuum extrapolation.

We compute $a_\mu^{l_q l_q}(\text{conn.})$ at each lattice spacing and available valence quark content qq in both the W and SD regions. The notation “ $a_\mu^{l_q l_q}$ ” denotes the light-quark contribution a_μ^{ll} (*i.e.*, including the light-quark charge factor defined in Sec. II A) evaluated at the qq meson mass. For $\Delta a_\mu^{ud,W}(\text{SIB})$, these data are corrected for finite-volume effects; we do not apply finite-volume corrections to $\Delta a_\mu^{ud,SD}(\text{SIB})$ for the reasons discussed in Sec. III B. We then

perform a chiral-continuum fit to these data for each window. The results of the fit are then used to extrapolate to the continuum and the physical uu , ll , and dd meson masses defined in Sec. II B. These values are then used to compute the SIB correction according to Eq. (2.7), where

$$a_\mu^{uu}(\text{conn.}) = \frac{q_u^2}{q_l^2} a_\mu^{l_u l_u}(\text{conn.}), \quad (4.10)$$

$$a_\mu^{dd}(\text{conn.}) = \frac{q_d^2}{q_l^2} a_\mu^{l_d l_d}(\text{conn.}). \quad (4.11)$$

In Eq. (2.7), the value of $a_\mu^{ll}(\text{conn.})$ comes from the SIB analysis rather than the value obtained in Sec. IV A. This allows us to preserve its correlations with $a_\mu^{uu}(\text{conn.})$ and $a_\mu^{dd}(\text{conn.})$, which are not directly available from the analysis in Sec. IV A. We choose to do a joint fit to the lattice-spacing and pion-mass dependencies here, as opposed to computing $\Delta a_\mu^{ud}(\text{SIB, conn.})$ at finite lattice spacing and taking the continuum limit (cf. Sec. IV D 2). This allows us to take advantage of the data available on the finer ensembles 0.06 fm, 0.09 fm, and 0.09* fm where the set of all three physical masses $\{uu, ll, dd\}$ is not complete.

The form of the chiral-continuum fit Ansätze is a modified version of the one used to perform data-driven M_π mistuning corrections in our previous intermediate windows calculation [12] and is given by

$$a_\mu^{l_q l_q}(a, M_\pi, M_A) = a_\mu^{l_q l_q}(a, M_\pi)[1 + F^M(M_A)], \quad (4.12)$$

where we take

$$a_\mu^{l_q l_q}(a, M_\pi) = c_{-1}(a)h(M_\pi/\Lambda) + c_0(a) + c_1(a)(M_\pi/\Lambda)^2, \quad (4.13)$$

$$c_i(a) = \sum_{j=0}^{n_i} c_{ij} (a_s^{\delta_{1j}})^\nu (a\Lambda)^{2j}, \quad i \in \{-1, 0, 1\}. \quad (4.14)$$

The term $F^M(M_A)$ is given by Eq. (3.7), and $\Lambda = 0.65$ GeV as in Eq. (4.3). The variations of the fit form above included in the BMA are as follows:

- Powers of M_π^2 : The pion mass dependence in Eq. (4.13) is varied through the choice of the function $h(x)$, which is taken to be one from the set $\{0, x^{-2}, \log x^2, x^4\}$ for a_μ^W observables and $\{0, \log x^2, x^4\}$ for a_μ^{SD} observables. At short distances, the mass dependence is expected to mild; indeed, we find that the term $h(x) = x^{-2}$ doesn't describe our data. The forms of these variations are inspired by chiral perturbation theory [93, 94]; see Ref. [12] for further discussion. In addition to the variations used in Ref. [12], we include the $h(x) = 0$ variation. Other forms of the M_π dependence were also considered, namely other two-term variations including either M_π^{-2} and M_π^0 terms or $\log M_\pi^2$ and M_π^0 terms, *i.e.*, with $h(x)$ in $\{x^{-2}, \log x^2\}$ but no M_π^2 ($i = 1$) term. These variations have negligible weight in the BMA due to a poor goodness of fit and thus are not included in the final analysis.
- Order in a^2 : The a^2 dependence is controlled by the parameters $\{n_i\}$, which are the upper limits of the sums in Eq. (4.14). We take $n_0 = 0, 1, 2, 3$ and $n_{i \neq 0} = 0, 1, 2$ with

the additional constraints that $\min(\{n_i\}) \geq 1$, and no fits with a negative number of degrees of freedom are included.¹²

- α_s dependence of the leading order a^2 term: The dependence on the strong coupling α_s is controlled by the parameter ν in Eq. (4.14), which sets the power of the α_s prefactor in the a^2 terms in the fit. For $\Delta a_\mu^{ud,W}(\text{SIB})$, $\nu = 0, 1, 2$ variations are included, while for $\Delta a_\mu^{ud,SD}(\text{SIB})$, only the $\nu = 0$ variation is included for reasons discussed in Appendix A.
- Sea-mass corrections: The form of the sea-mass correction $F^M(M_A)$ is the same as in Eq. (3.7). For the 0.15' fm ensemble, which has distinct up and down sea quark masses, an additional term is included to correct ΔM_K^2 defined in Eq. (2.15). Specifically,

$$F_{0.15' \text{ fm}}^M(M_A) = C_{\text{sea}} \sum_{A=\pi,K,\Delta K} \delta M_A^2, \quad \delta M_{\Delta K}^2 = \frac{\Delta M_{K,\text{phys.}}^2 - \Delta M_{K,\text{latt.}}^2}{\Delta M_{K,\text{phys.}}^2}. \quad (4.15)$$

Variations with and without the sea-mass correction term are included.

- Finite-volume corrections: In W, four of the finite-volume models introduced in Sec. III are included, namely NLO and NNLO χ PT, CM, and HP schemes. For reasons discussed in Sec. III B, the MLLGS model is not usable at the 0.15 fm points and thus is not applied here. In SD, no finite-volume models are included for reasons discussed in Sec. III B. Unlike many of the other observables, taste-breaking corrections in part cancel when computing $\Delta a_\mu^{ud}(\text{SIB})$ and hence have virtually no impact on the continuum limit. Thus, no variations in taste-breaking corrections are included here. Furthermore, this means there are no complications introduced by the mixing of finite-volume and taste-breaking models for this observable, which is why the HP model is used here but not elsewhere.
- Data subsets: In addition to using the full range of lattice spacings over [0.06, 0.15] fm, we also include variations that exclude the coarsest ensembles at 0.15 fm and the finest ensemble at 0.06 fm. The former variation is considered since it reduces discretization effects in the chiral-continuum extrapolation. The latter is considered since the 0.06 fm ensemble includes only the ll point and thus does not help constrain the M_π dependence in the chiral-continuum extrapolation; in practice, the presence of the 0.06 fm point does not affect the continuum value of $\Delta a_\mu^{ud}(\text{SIB, conn.})$. In fits that cut away data, the maximum order of the a^2 dependence is reduced to avoid fits with a negative number of degrees of freedom. Hence, the constraints listed above become $n_0 = 0, 1, 2$ and $n_{i \neq 0} = 0, 1$ for fits over the range [0.06, 0.12] fm and $n_i = 0, 1, 2$ for fits over the range [0.09, 0.15] fm.¹³

Similarly to Sec. IV A, we impose a Gaussian prior constraint $C_{\text{sea}} = 0.000(2)$ on the sea-mass correction; all other parameters are unconstrained. Because of combinatorial effects

¹² A naive frequentist degree-of-freedom counting would indicate some fits with sea-mass corrections have a negative number of degrees of freedom; however, the tight prior on C_{sea} (see Sec. IV A) leads to a positive number of Bayesian degrees of freedom for these fits.

¹³ The fits on only [0.06, 0.12] fm remove uu , ll , and dd data at 0.15 fm, so the maximum $n_{i \neq 0}$ is reduced. The fits on only [0.09, 0.15] fm remove ll data and thus do not have a reduced range of $n_{i \neq 0}$ values.

introduced by the degree-of-freedom counting discussed above, there would be *a priori* model biasing introduced by a naive, flat model-prior probability $\text{pr}(M) = 1/N_M$ in Eq. (3.12). For example, there are more possible fit variations for each of $h(x)$ in $\{x^{-2}, \log x^2, x^4\}$ than those with $h(x) = 0$ because in the latter case there are no additional variations from the $c_{-1}(a)$ polynomial. This discrepancy biases the final BMA result by disfavoring the $h(x) = 0$ variations. To account for such biases, the model-prior probabilities have been chosen to approximately eliminate this bias over the data subset and M_π dependence variations. Specifically, denoting a model fit to data subset s with M_π dependence h as $M_{s,h}$, we take

$$\text{pr}(M_{s,h}) = \frac{1}{N_{\text{subsets}}} \frac{1}{N_{M_\pi}} \frac{1}{N_s} \frac{1}{N_h}, \quad (4.16)$$

where N_{subsets} is the number of data subset variations in the model space (three here), N_{M_π} is the number of different M_π variations (four on W , three on SD), N_s is the number of models fit to the data subset s , and N_h is the number of models with the M_π dependence h .

The results of the BMA procedure with the variations to $\Delta a_\mu^{ud,W}(\text{SIB, conn.})$ listed above are shown in Fig. 14. The top panel shows the best-fit chiral-continuum extrapolations evaluated at the physical $M_\pi^{uu}, M_\pi^{ll}, M_\pi^{dd}$ masses versus the lattice spacing; extrapolation curves are shown relative to the center value of the physical ll curve $a_\mu^{ll}(a, M_\pi^{ll})$. The bottom panels summarize the results of all fits as a weighted histogram (left panel) and versus their respective model probabilities (right panel) compared with the BMA result (red line and bands).

Similarly to previous sections, we perform Bayesian model averages over subsets of the model space, holding a single model choice fixed while varying the others. The results of this procedure for $\Delta a_\mu^{ud,W}(\text{SIB, conn.})$ are shown in Fig. 15. The individual model subset averages are shown on the left and the relative probabilities of these subsets, as defined in Eq. (3.13), are shown on the right. The full BMA result is shown on the top of the left panels and in the corresponding red line and bands. The four following points on the left and top pie chart on the right correspond to the four finite-volume schemes (NLO and NNLO χ PT, CM, and HP). As noted above and shown in Fig. 3, the tension between the CM scheme and the other schemes leads to a significant source of systematic error for this observable. The next three points and corresponding pie chart shows the three data subset variations. We see that the results for $\Delta a_\mu^{ud,W}(\text{SIB, conn.})$ are fairly insensitive to data cuts, with the full data set being favored by the BMA due the N_{cut} penalty in Eq. (3.12). The next seven points and two pie charts correspond to variations in the lattice-spacing dependence (first three points and pie chart) and M_π dependence (next four points and pie chart) in the chiral-continuum fit Ansätze. The next two points and corresponding pie chart show the effect of including the sea-mass correction or not. Again, this correction has a small impact on the final BMA results. The last three points and corresponding pie chart shows the α_s dependence variations. While the results vary slightly with different powers of α_s , none of these variants is favored over the others by the BMA.

As a cross-check, we can compare the model-based corrections for Δ_{M_π} defined in Sec. III B with a data-driven estimate that can be obtained from the $\Delta a_\mu^{ud,W}(\text{SIB, conn.})$ BMA. Specifically, we perform a Bayesian model average for the difference between the lattice results and fit results at the physical pion masses for each ensemble and pion flavor qq on W ; for simplicity, we use the same model space as described above, except for the data-subset variations where only the full dataset $[0.06, 0.15]$ fm is used. We do not perform this comparison at hh on 0.09^* fm where the mass shift is too large to be reliably estimated

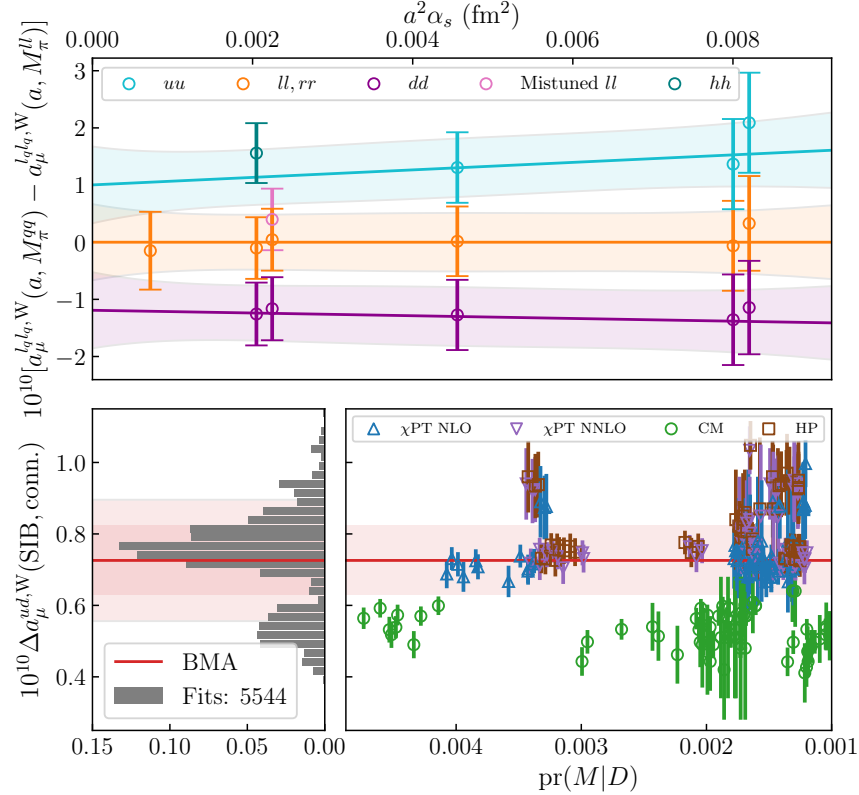


FIG. 14. Results of the BMA procedure applied to $\Delta a_\mu^{ud,W}(\text{SIB, conn.})$. *Upper panel*: The chiral-continuum fit with the maximum model probability, as well as the corresponding data, relative to the central value of the extrapolation curve evaluated at the physical ll point. The curves are extrapolations evaluated at physical pion masses for $a_\mu^{uu}(\text{conn.})$, $a_\mu^{ll}(\text{conn.})$, and $a_\mu^{dd}(\text{conn.})$ (light-cyan, -orange, and -purple bands, respectively); the data match this coloring except for the mistuned ll point at 0.09 fm (pink) and the hh point at 0.09* fm (teal). Data from the 0.09 fm and 0.15' fm ensembles include a small, rightward offset for visual clarity. The symbol shapes indicate that the data are corrected with the CM finite-volume scheme (see description of the lower right panel). *Lower left panel*: Model probability-weighted histogram of all continuum $\Delta a_\mu^{ud,W}(\text{SIB, conn.})$ extrapolations used in the BMA. *Lower right panel*: Individual model predictions of $\Delta a_\mu^{ud,W}(\text{SIB, conn.})$ versus the corresponding model probability defined in Eq. (3.12). Note that the model probabilities decrease in going from left to right. The colors and symbols indicate the finite-volume scheme of each fit. Models with $\text{pr}(M|D) < 10^{-3}$ are not shown. In the lower panels, the BMA result is shown in light-red, where the inner and outer bands correspond to the error coming from the first term in Eq. (3.11) and the total error, respectively.

by the EFT and EFT-inspired models or at 0.15' fm where the model-based results are nearly identical to those for the 0.15 fm ensemble, which dominates the fits statistically at this lattice spacing. The results of this comparison are given in Fig. 16, which shows that the model-based and data-driven results are in agreement.

The results of the BMA overall fit variations to $\Delta a_\mu^{ud,SD}(\text{SIB, conn.})$ are shown in Fig. 17 with the model subspace averaging procedure, which is a subset of that discussed above for W, shown in Fig. 18. As expected, the SD SIB correction is much smaller than that of W, shown in Fig. 18. As expected, the SD SIB correction is much smaller than that of W due to the significantly weaker mass dependence in SD. As seen in the bottom panels

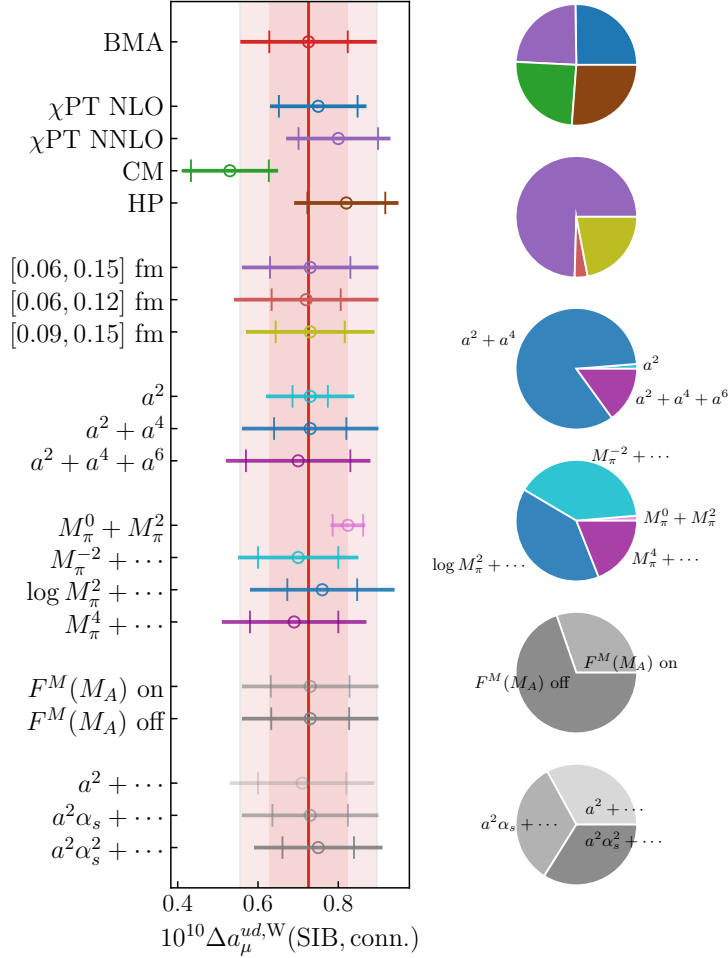


FIG. 15. Breakdown of the BMA procedure applied to $\Delta a_\mu^{ud,W}(\text{SIB, conn.})$. *Left panel*: From top to bottom, the first point is the full BMA result, including all model variations. The next block of four points show the result of varying the finite-volume correction schemes. The next three points show the result of varying the data subsets. The next two blocks of results come from variations in the chiral-continuum extrapolation, namely the lattice-spacing and the pion-mass dependencies, respectively. In the former case, the set of models is partitioned by the highest-order term in the extrapolation; in the latter case, by the variations described in the text. The next two show results of fit variations that include or do not include the sea-mass correction $F^M(M_A)$. The final three show the result of varying powers of α_s in the a^2 term of the fit function. The inner error bars on the data points correspond to the first term in Eq. (3.11), while the outer are the total errors. *Right panels*: Pie charts showing the contributions to the BMA corresponding to the partitions in the left panel. The percentages are computed according to Eq. (3.13).

of Fig. 17 and the left panel of Fig. 18, there are two outlier fits with nonnegligible model probability that significantly inflate the systematic error.¹⁴ Since the contribution of these fits to the total error is small when $\Delta a_\mu^{ud,SD}(\text{SIB, conn.})$ is added to other observables, we retain these fits in order to give a conservative error estimate for $\Delta a_\mu^{ud,SD}(\text{SIB, conn.})$.

¹⁴ These fits are cubics in a^2 with $h(x) = x^4 M_\pi$ -dependence and are fit to all the data with and without the sea-mass corrections.

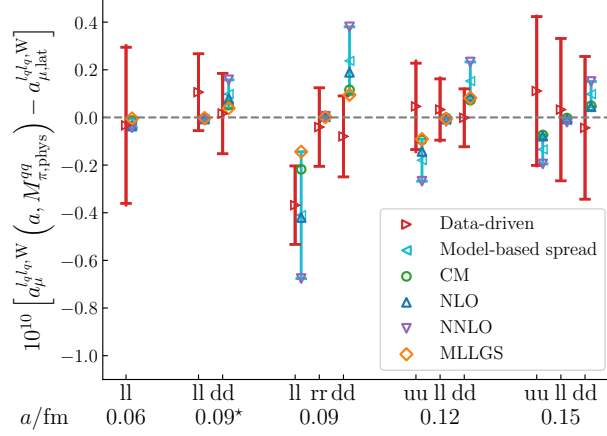


FIG. 16. Comparison of various model-based and the data-driven corrections with the light-quark connected a_μ^W resulting from adjustments to the value of M_π for each ensemble and valence quark content. Individual EFT and EFT-inspired models are denoted by open symbols; the cyan error bars denote the full spread of the model-based result; the red error bars are the data-driven determinations from the BMA. The model-based results shown with a small, rightward offset for visual clarity.

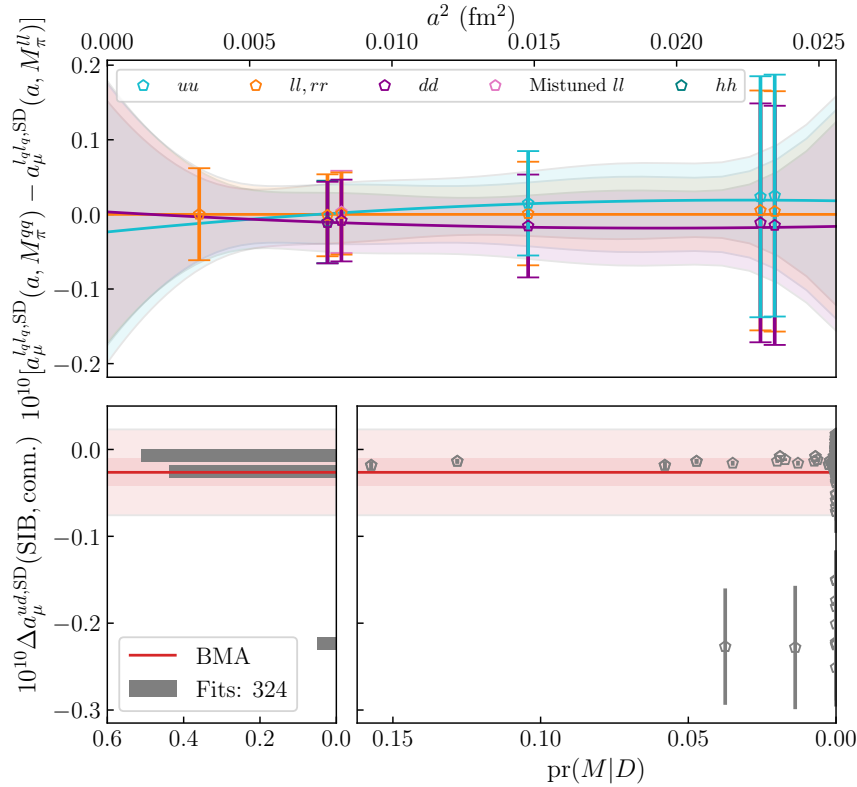


FIG. 17. Results of the BMA procedure applied to $\Delta a_\mu^{ud,SD}(\text{SIB, conn.})$. See caption of Fig. 14 for a description of the figure. Note that no finite-volume correction is applied to $\Delta a_\mu^{ud,SD}(\text{SIB, conn.})$, and hence there is no differentiation with colors or symbols in the lower right panel.

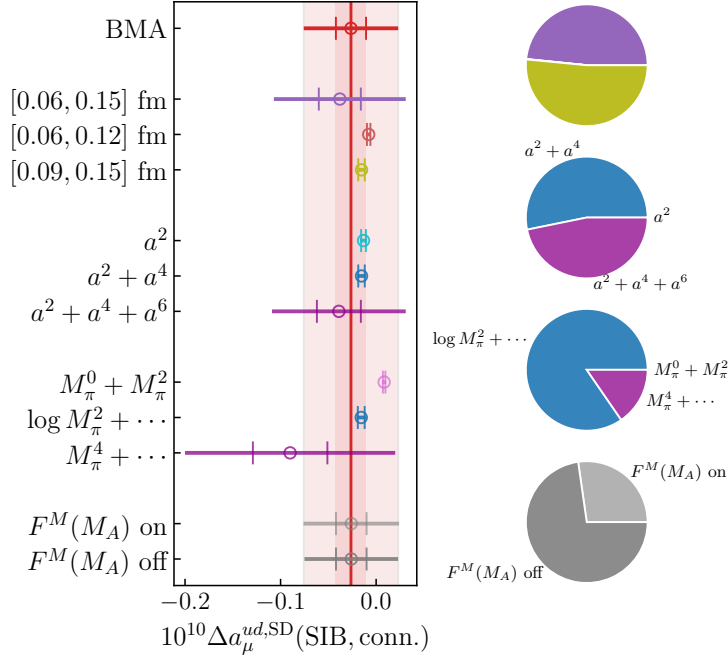


FIG. 18. Breakdown of the BMA procedure applied to $\Delta a_\mu^{ud,SD}(\text{SIB, conn.})$. See caption of Fig. 15 for a description of the figure.

2. Disconnected strong-isospin breaking

The disconnected SIB dataset is obtained using the one-link current (see Table VII). These data span three lattice spacings—0.09 fm, 0.12 fm, and 0.15 fm—and are evaluated for light quarks l and s in the isospin-symmetric limit and for light quarks u , d , and s with isospin breaking. The quark masses are those used to produce Table II.

As in Eq. (2.7), we compute $\Delta a_\mu^{ud}(\text{disc.}) = a_\mu^{ud}(\text{disc.}) - a_\mu^{ll}(\text{disc.})$ at each lattice spacing in both W and SD. At finite lattice spacing, model-based finite-volume and taste-breaking corrections to $\Delta a_\mu^{ud}(\text{disc.})$ cancel to leading order in the light quark mass splitting $m_d - m_u$ and hence are beyond the present scope of leading-order strong-isospin breaking effects. We perform a continuum fit to these data in each window. The continuum fit Ansätze are of the same form as Eq. (3.6), which is analogous to Eq. (4.12) with the M_π dependence removed. Here, $F^{\text{disc.}}$ is given by

$$F_{\text{SIB}}^{\text{disc.}}(a) = \sum_{j=1}^n c_j (\alpha_s^{\delta_{1j}})^\nu (a\Lambda)^{2j}, \quad (4.17)$$

$F^M(M_A)$ is given by Eq. (3.7), and $\Lambda = 0.9$ GeV as in Eq. (4.7). Included in the BMA are the following variations of the fit form:

- Order in a^2 : The a^2 dependence is controlled by the parameter n , which is the upper limit of the sum in Eq. (4.17). We take $n = 1, 2$ with the additional constraint that no fits with a negative number of degrees of freedom are included. In SD, we find that log enhancement of the one-link current (see Appendix A) leads to a functional dependence of the form $a^2 \log a$ in the data. Thus for SD, we also include variations of the form $a^2 \log a$, $a^2 \log a + a^2$, and $a^2 \log a + a^4$.

- α_s dependence of the leading order a^2 term: The α_s -dependence variations of other observables using one-link current data are determined using a combination of the results from Appendix A and empirical Bayes analyses; however, since for Δa_μ^{ud} (SIB, disc.) we extrapolate the difference of two values of the disconnected contribution to a_μ , these arguments cannot be applied directly. Instead, we determine the α_s -dependence variations for Δa_μ^{ud} (SIB, disc.) empirically based on results from the BMA, selecting those variations with favorable model weights. We find a reasonable yet conservative set of variations are $\nu = 0, 1, 2$ in W and $\nu = 0$ only in SD.
- Mass-mistuning corrections: The form of the mass-mistuning correction $F^M(M_A)$ is the same as from Sec. IV A. Variations with and without the mass correction term are included.
- Data subsets: In addition to using the full range of lattice spacings over $[0.09, 0.15]$ fm, we also include variations that exclude the coarsest ensemble at 0.15 fm and the finest ensemble at 0.09 fm. The former is included to reduce discretization effects in the chiral-continuum extrapolation. The latter is included to inflate the systematic error, which is similar to what is done in the a_μ^{SD} (disc.) analysis; this error inflation reflects the modeling uncertainty associated with the limited amount of disconnected data available. As discussed in Sec. IV D 1, fits in which data have been cut away do not include the $n = 2$ variation.

The parameter priors are analogous to those discussed in Sec. IV D 1; the bias introduced by using flat model priors $\text{pr}(M) = 1/N_M$ is small for these observables.

The results of the BMA procedure with the variations to $\Delta a_\mu^{ud,W}$ (SIB, disc.) listed above are shown in Fig. 19. The top panels show the results of all continuum extrapolations, with a weighted histogram of the continuum results in the left panel and all the extrapolation fits versus the lattice spacing in the right panel. The opacities of the continuum extrapolations are proportional to the respective model weights; for fits with mass-mistuning corrections, the mass-corrected data points are also shown but are difficult to see due to the smallness of these corrections and the light opacity of these variations. The bottom panel shows the continuum results of the fits versus their respective model probabilities. In the upper left and bottom panels, the BMA result is shown by the red line and bands. The final BMA error of $\Delta a_\mu^{ud,W}$ (SIB, disc.) is dominated by the first term in Eq. (3.11) as shown by the inner red band.

Again, we perform Bayesian model averages over subsets of the model space where a single model choice has been held fixed. The results of this procedure for $\Delta a_\mu^{ud,W}$ (SIB, disc.) are shown in Fig. 20. The individual model subset averages are shown on the left and the relative probabilities of these subsets, as defined in Eq. (3.13), are shown on the right. The full BMA result is shown on the top of the left panels and in the corresponding red line and bands. The following three points and corresponding pie chart show the three data subset variations. We see that the full data set is favored by the BMA due the N_{cut} penalty in Eq. (3.12). The next two points and pie chart correspond to the different lattice spacing dependence. The next two points and corresponding pie chart show the effect of including the mass-mistuning correction or not, which behaves similarly to those in Fig. 15. The last three points and corresponding pie chart show the α_s dependence variations. As for $\Delta a_\mu^{ud,W}$ (SIB, conn.), none of these variants are favored over the others by the BMA.

The results of the BMA overall fit variations to $\Delta a_\mu^{ud,SD}$ (SIB, disc.) are shown in Fig. 21 with the model subspace averaging procedure shown in Fig. 22. The set of variations in

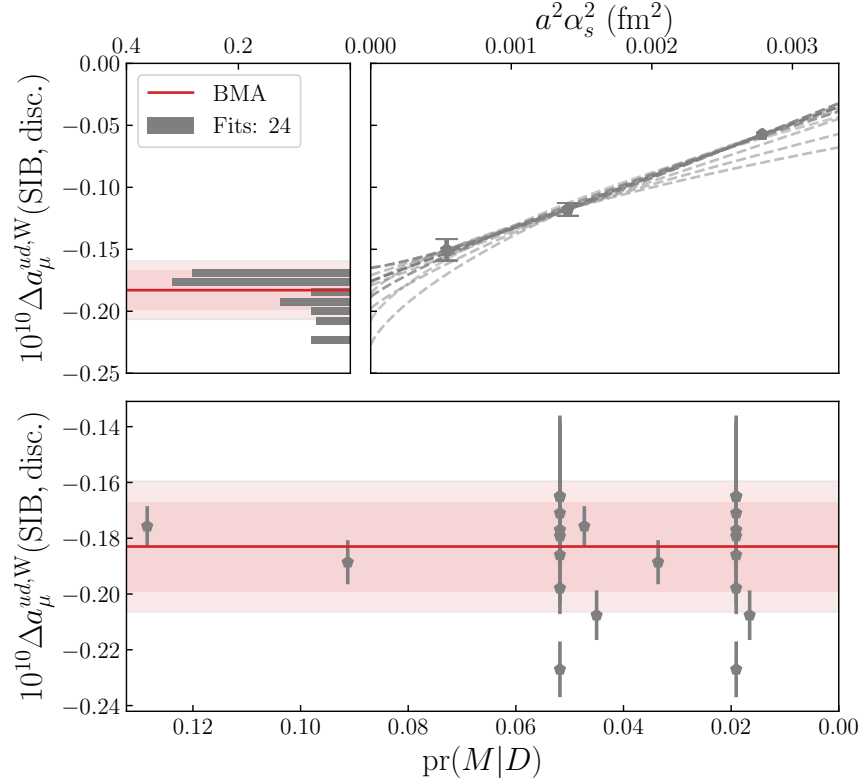


FIG. 19. Results of the BMA procedure applied to $\Delta a_\mu^{ud,W}(\text{SIB}, \text{disc.})$. *Upper left panel*: Model probability-weighted histogram of all continuum $\Delta a_\mu^{ud,W}(\text{SIB}, \text{disc.})$ extrapolations used in the BMA. *Upper right panel*: Extrapolation curves and corresponding data for all model variations included, with opacities proportional to the respective model probabilities. The data are corrected for mass-mistuning where applicable, but this is a small effect. *Lower panel*: Individual model predictions of $\Delta a_\mu^{ud,W}(\text{SIB}, \text{disc.})$ versus the corresponding model probability defined in Eq. (3.12). Note that the model probabilities decrease in going from left to right. In the upper left and lower panels, the BMA result is shown in light-red, where the inner and outer bands correspond to the error coming from the first term in Eq. (3.11) and the total error, respectively.

Fig. 22 is a subset of those in Fig. 20 for W except for the lattice spacing dependence variations, which now also include the fits with $a^2 \log a$ terms. Again, the SD SIB correction is much smaller than the corresponding W value due to the weaker mass dependence in SD. For this observable, the systematic error is significantly increased by the coarse data subset $[0.12, 0.15]$ fm. Even with this error inflation procedure, the resultant uncertainty on $\Delta a_\mu^{ud,SD}(\text{SIB}, \text{disc.})$ is small compared with that of other observables.

E. Perturbative QCD estimates of short-distance observables

As a consistency check on our short-distance window results, we compare our lattice determinations with predictions from perturbative QCD (pQCD). Specifically, we use the $\mathcal{O}(\alpha_s^4)$ determination of the R ratio, $R(s)$, from the software package `rhad` [95]. Results produced from this code have been used to supplement other short-distance (or high-energy) lattice determinations of $a_\mu^{\text{HVP,LO}}$ [10, 14, 96]. pQCD results for $R(s)$ can be converted to

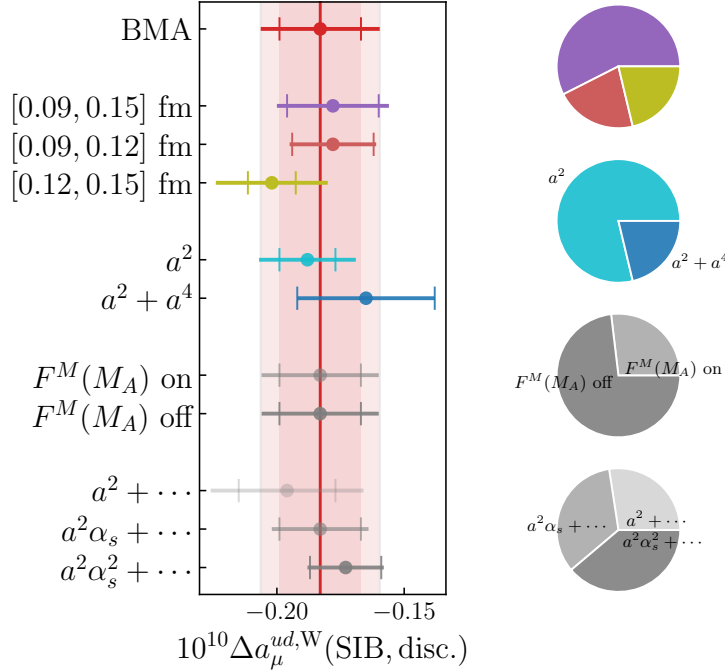


FIG. 20. Breakdown of the BMA procedure applied to $\Delta a_\mu^{ud,W}(\text{SIB, disc.})$. *Left panel*: From top to bottom, the first point is the full BMA result including all model variations. The next block of three points show the effect of varying the data subset. The next two points are from varying the lattice spacing dependence in the continuum extrapolation, as distinguished by the highest order term in the extrapolation. The next two come from fit variations that include or exclude, respectively, the mass-mistuning correction $F^M(M_A)$. The final three show the effect of varying the powers of α_s in the a^2 term of the fit function. The inner error bars on the data points correspond to the first term in Eq. (3.11), while the outer are the total errors. *Right panels*: Pie charts showing the contributions to the BMA corresponding to the breakdowns in the left panel. The percentages are computed according to Eq. (3.13).

the Euclidean time domain using a Laplace transform,

$$C(t) = \frac{1}{12\pi^2} \int_0^\infty dE E^2 R(E^2) e^{-Et}. \quad (4.18)$$

Alternatively, $C(t)$ is the Fourier transform of the vector correlator in momentum space [97]; see Ref. [13] for a comparison with lattice-QCD calculations. With either approach, the resulting $C(t)$ can then be used to compute window observables via Eq. (2.9).

Comparisons of pQCD calculations with hadronic results (from lattice or e^+e^- data) rely on quark-hadron duality. The Laplace transform smears out the peaked structure of $R(s)$ [98, 99], so this duality is expected to hold rather accurately for a_μ and related windows.

For the connected contributions, we pursue an approach employed in Ref. [13] for the light-quark case. Specifically, we extrapolate our lattice results to the continuum for a flexible window $\mathcal{W}_2(t, t', 0.4, 0.15)$. The contribution from the complementary short-distance window, $\mathcal{W}_1(t, t', 0.15)$, is then computed using the pQCD determination of $C(t)$ via $R(s)$ from `rhad` [95]. The sum of the lattice and perturbative results are then computed as a function of t' . As in Ref. [13], we monitor the combined result for stability out to the edge of the standard short-distance window, $t' = 0.4$ fm. In addition to studying the light-quark

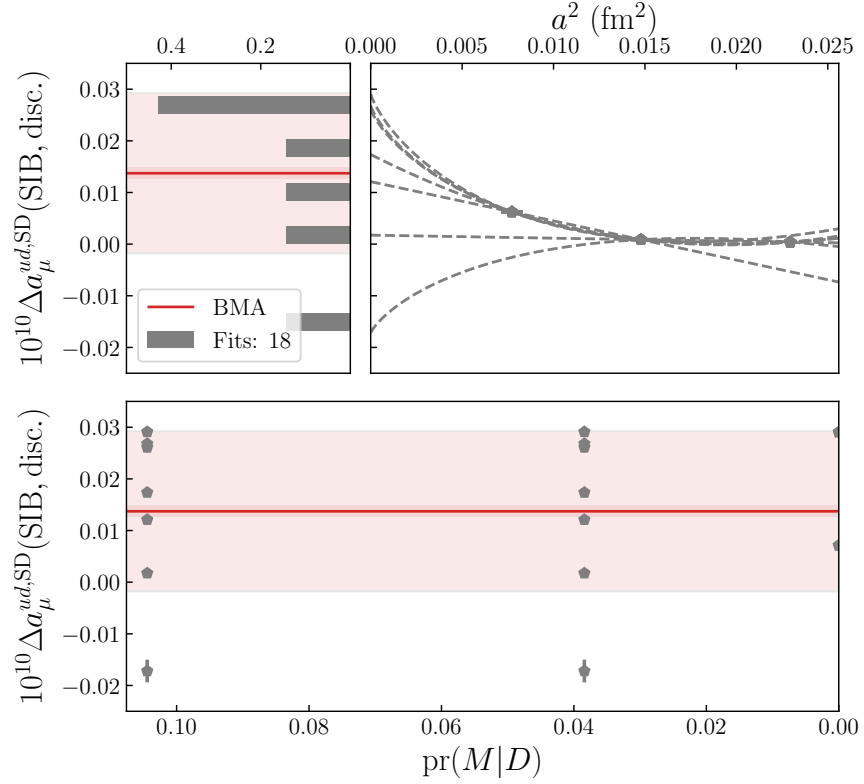


FIG. 21. Results of the BMA procedure applied to $\Delta a_\mu^{ud,SD}(\text{SIB, disc.})$. See caption of Fig. 19 for a description of the figure.

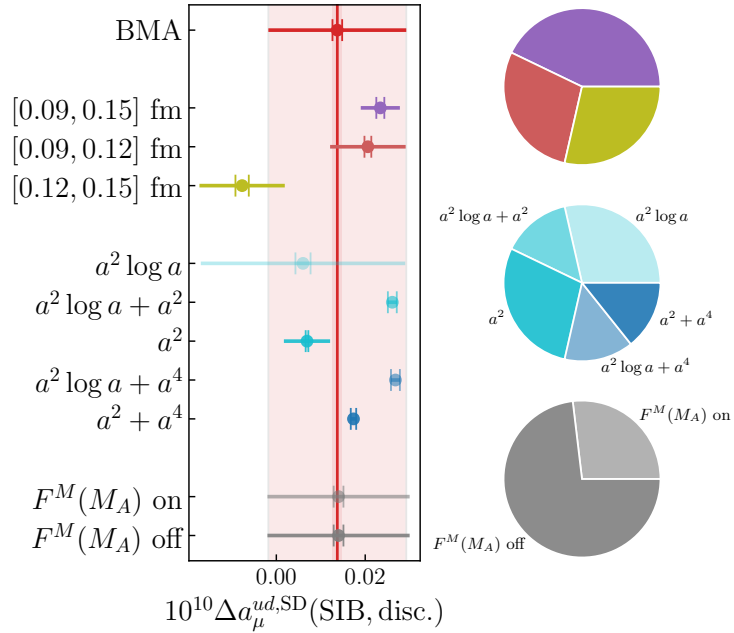


FIG. 22. Breakdown of the BMA procedure applied to $\Delta a_\mu^{ud,SD}(\text{SIB, disc.})$. See caption of Fig. 20 for a description of the figure.

contribution in this way, we also examine the cases of strange and charm.

The `rhad` software package requires as inputs a threshold and quark masses for the loops, which we choose as follows. For the connected light and strange contributions, the lower threshold is taken to be $2\bar{m}_q$, where \bar{m}_q is the $\overline{\text{MS}}$ mass at $\mu = \bar{m}_q$, taken from Ref. [35] (which leans heavily on Ref. [100]). The light and strange propagators in the loops are taken to be massless. For the charm quark, we employ both available options in the software, namely either using the pole mass or the running $\overline{\text{MS}}$ mass $\bar{m}_c(\sqrt{s})$. The charm threshold is then taken to be $2m_c$. We also evaluate the light-strange disconnected contribution (called “singlet” in `rhad`) in pQCD. Here, we use massless light quarks and a massive strange quark. The QED contribution is computed for the massless light and strange quarks, and the $\Delta a_\mu^{ud,SD}$ (SIB) contribution is negligible and, thus, ignored.

Results for the perturbative replacement procedure described above are shown in Fig. 23 for the light, strange, and charm contributions, respectively. For this test, it suffices to use only the local vector current and a single fit to the data. A full BMA as in Secs. IV A and IV B would be unnecessarily arduous, so we choose a representative fit from amongst the fits with the highest BMA weights in the full $a_\mu^{ll,SD}(\text{conn.})$, $a_\mu^{ss,SD}(\text{conn.})$, and $a_\mu^{cc,SD}(\text{conn.})$ analysis. We find that, for the light and strange contributions, the massless perturbative result is consistent with the lattice result, and we have stability out to the end of the short-distance window as in Ref. [13]. For charm, where the quark-mass scheme is relevant, such stability is not observed. We find that when using the pole mass for the charm quark, the perturbative result is marginally smaller than the lattice result, and we see only partial stability out to $t' = 0.1$ fm. Using the $\overline{\text{MS}}$ mass and allowing the mass to run, we obtain a perturbative result that is significantly larger than the lattice result. The authors of Ref. [95] recommend using the pole mass near threshold and switching to the $\overline{\text{MS}}$ mass at larger energies. In theory, tuning can be performed to match the lattice results by playing with a switch-over energy, but we did not find this exercise illuminating.

We note that the authors of Ref. [10] used the running $\overline{\text{MS}}$ mass approach to obtain a result for the bottom contribution to the short-distance window of

$$a_\mu^{bb,SD,pQCD,ETMC}(\text{conn.}) = 0.32 \times 10^{-10}. \quad (4.19)$$

This result is in good agreement with previous lattice determinations of this quantity for the full integrand [101],

$$a_\mu^{bb,\text{latt},HPQCD}(\text{conn.}) = 0.300(15) \times 10^{-10}, \quad (4.20)$$

with the difference between the short-distance and full integrand contribution for bottom expected to be in the third digit. For completeness, we give the pQCD result for this contribution using the pole mass for the bottom quark from Ref. [95],

$$a_\mu^{bb,SD,pQCD,pole\ mass}(\text{conn.}) = 0.28 \times 10^{-10}. \quad (4.21)$$

As in the case of charm-quark, we observe that the two perturbative determinations bound the lattice result. Additionally, we use the pQCD estimate for bottom contribution to the intermediate window from the following difference,

$$a_\mu^{bb,W}(\text{conn.}) = a_\mu^{bb,pQCD}(\text{conn.}) - a_\mu^{bb,SD,pQCD}(\text{conn.}) = 0.004 \times 10^{-10}. \quad (4.22)$$

using the pole mass.

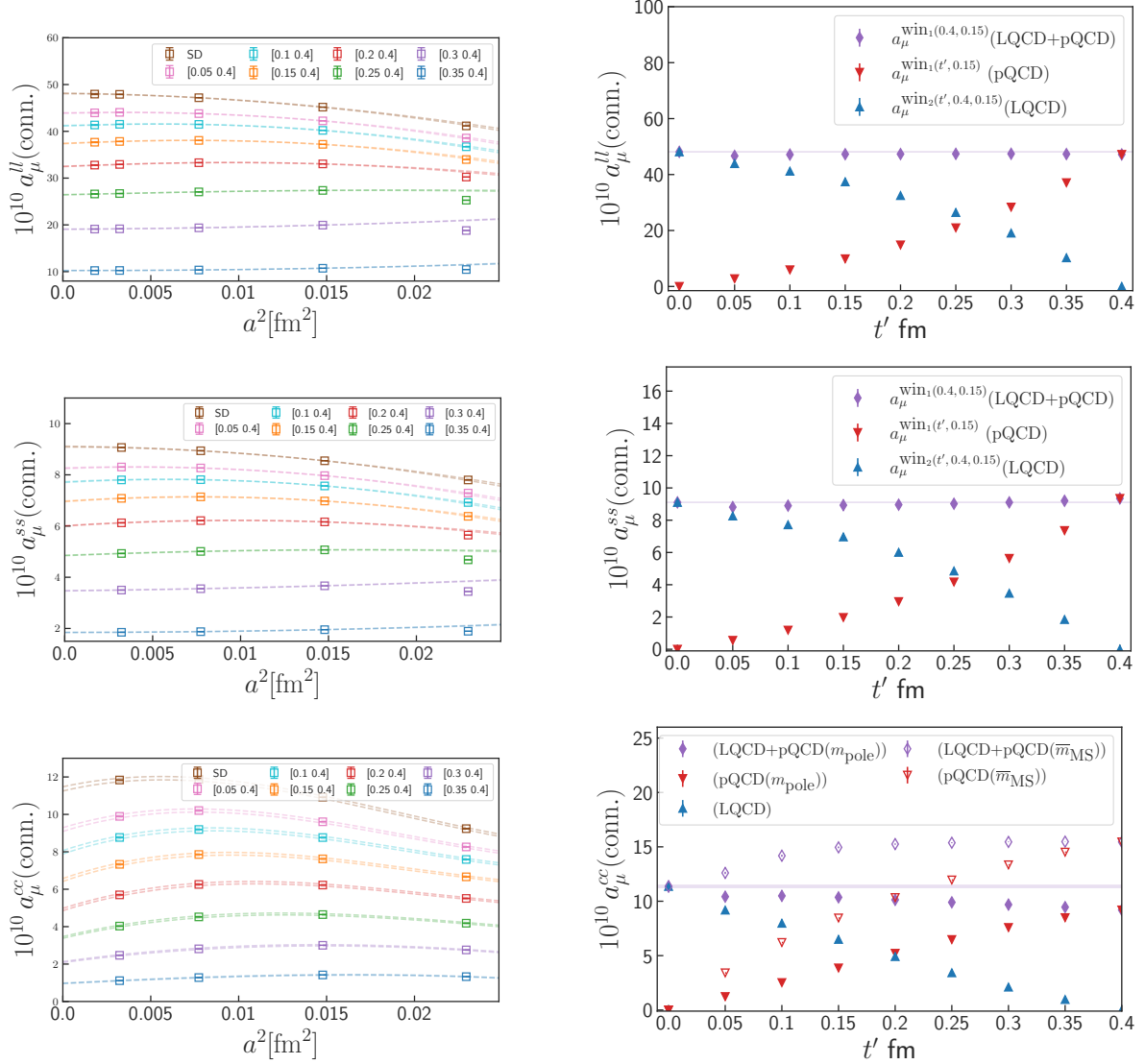


FIG. 23. Stability analysis for the light- (top), strange- (middle), and charm-quark (bottom) contributions to the short-distance window. *Left panels:* Results of continuum extrapolations for the short-distance sub-windows with the lattice data. *Right panels:* Combinations of lattice and perturbative QCD results from the sub-windows totaling the full short-distance window as a function of t' .

For the disconnected contribution, we obtain a pQCD result of

$$a_\mu^{\text{pQCD}}(\text{disc.}) = -0.00547 \times 10^{-10}. \quad (4.23)$$

As discussed in Sec. IV C, this result does not enter the analysis. We compare it with our result for $a_\mu^{\text{SD}}(\text{disc.})$ in Fig. 13.

Finally, we compute the $\mathcal{O}(\alpha\alpha_s)$ QED corrections to the massless light and strange contributions in the short-distance window,

$$\Delta a_\mu^{ll, \text{SD}}(\text{QED}, \text{conn.}) = 0.0265 \times 10^{-10}, \quad (4.24)$$

$$\Delta a_\mu^{ss, \text{SD}}(\text{QED}, \text{conn.}) = 0.0016 \times 10^{-10}. \quad (4.25)$$

TABLE VIII. Approximate absolute error budgets (in units of 10^{-10}) for the uncertainties reported in Eqs. (5.1)–(5.6).

Contribution	stat.	$a \rightarrow 0$	w_0 (fm), w_0/a	Z_V	m_u/m_d	Total
$a_\mu^{ll,SD}$ (conn.)	0.016	0.067	0.011	0.065	—	0.096
$a_\mu^{ss,SD}$ (conn.)	0.003	0.012	0.006	0.015	—	0.021
$a_\mu^{cc,SD}$ (conn.)	0.00	0.12	0.09	0.03	—	0.16
a_μ^{SD} (disc.)	0.0006	0.0053	0.0000	0.0000	—	0.0054
$\Delta a_\mu^{ud,SD}$ (SIB, conn.)	0.004	0.047	0.002	0.015	0.002	0.049
$\Delta a_\mu^{ud,SD}$ (SIB, disc.)	0.000	0.015	0.001	0.000	—	0.016

Higher order contributions, including the QED correction to the disconnected diagram, which enter at $\mathcal{O}(\alpha\alpha_s^3)$, are neglected in this estimate [95].

V. RESULTS

A. Short-distance window observables

Our final determinations for the individual contributions to $a_\mu^{\text{HVP,LO}}$ in the short-distance window are

$$a_\mu^{ll,SD}(\text{conn.}) = 48.116(16)(94)[96] \times 10^{-10}, \quad (5.1)$$

$$a_\mu^{ss,SD}(\text{conn.}) = 9.103(3)(21)[21] \times 10^{-10}, \quad (5.2)$$

$$a_\mu^{cc,SD}(\text{conn.}) = 11.48(0)(16)[16] \times 10^{-10}, \quad (5.3)$$

$$a_\mu^{SD}(\text{disc.}) = -0.0002(6)(53)[55] \times 10^{-10}, \quad (5.4)$$

$$\Delta a_\mu^{ud,SD}(\text{SIB, conn.}) = -0.026(4)(49)[49] \times 10^{-10}, \quad (5.5)$$

$$\Delta a_\mu^{ud,SD}(\text{SIB, disc.}) = 0.014(0)(16)[16] \times 10^{-10}. \quad (5.6)$$

The breakdown of uncertainties is given in Table VIII. We compare with previous lattice determinations in Fig. 24. For the light-quark connected contribution, we obtain a result with a relative error of 0.2%. The benefit of the HISQ local current mitigating the log-enhancement effects associated with short-distance $a_\mu^{\text{HVP,LO}}$ observables (see Appendix A) is apparent. This is the most precise determination of this quantity to date and is in reasonable agreement with all previous determinations (left side of Fig. 24). Indeed, the strengths of the local current are apparent in the heavier flavor contributions, $a_\mu^{ss,SD}(\text{conn.})$ and $a_\mu^{cc,SD}(\text{conn.})$, also, with our determinations being the most precise to date. We note that our calculation of $a_\mu^{ll,SD}(\text{conn.})$ differs from the data-driven evaluation of Ref.[102] by 2.4σ .

The particulars of the disconnected contribution in the short-distance window are such that the quantity is nearly zero with difficult to determine systematic effects associated with the short-distance window boundary, the behavior of the disconnected correlation function, and staggered oscillating effects. As such, we estimate this quantity with a conservative approach and obtain a result consistent and competitive with previous determinations in both central value and uncertainties. Our results for the strong-isospin-breaking contribution to a_μ^{SD} [Eqs. (5.5) and (5.6)] are both consistent with zero, as expected. We are the first to put forth a lattice calculation of this quantity.

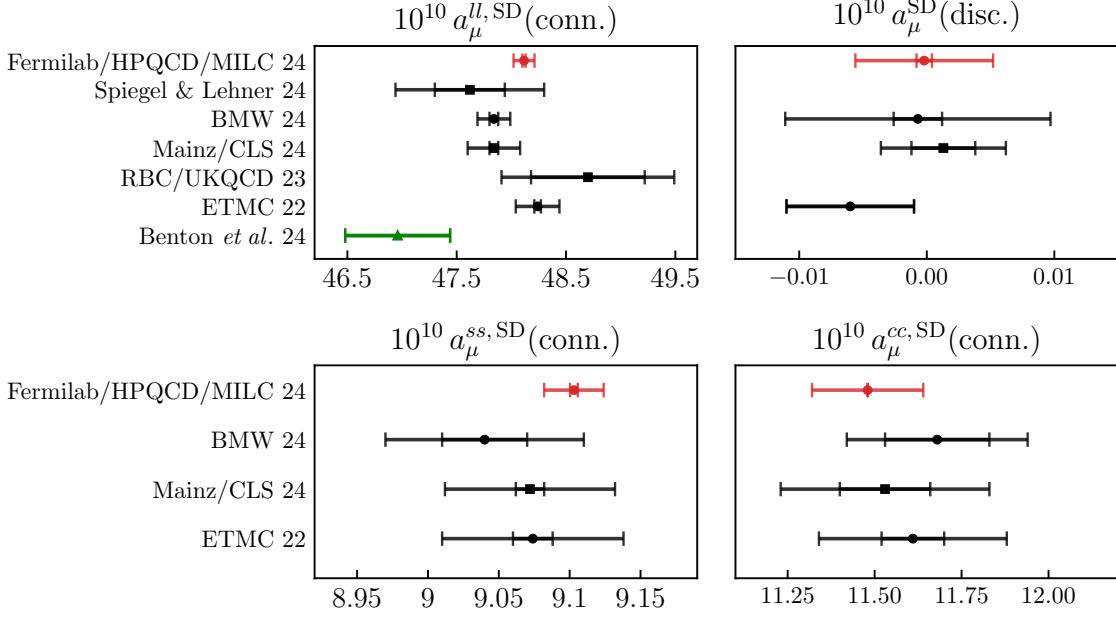


FIG. 24. Comparison of our lattice determinations for $a_\mu^{ll,SD}(\text{conn.})$, $a_\mu^{ss,SD}(\text{conn.})$, $a_\mu^{SD}(\text{disc.})$, and $a_\mu^{cc,SD}(\text{conn.})$ (red circles) labeled “Fermilab/HPQCD/MILC 24” with $n_f = 2 + 1 + 1$ (black circles) and $n_f = 2 + 1$ (black squares) lattice-QCD calculations by Spiegel & Lehner 24 [16], BMW 24 [14], Mainz/CLS 24 [103], RBC/UKQCD 23 [13] and ETMC 22 [10]. The inner error bar shown for our result is from Monte Carlo statistics. Also shown is a data-driven evaluation of $a_\mu^{ll,SD}(\text{conn.})$ using e^+e^- cross section data (green triangle) by Benton *et al.* 24 [102].

For the bottom-quark connected and QED contributions to a_μ^{SD} we consider existing lattice and phenomenological results in our estimates. In particular, for $a_\mu^{bb,SD}(\text{conn.})$, we take the previous HPQCD determination [101] and subtract from it the estimate of $a_\mu^{bb,W}(\text{conn.})$ in Eq. (4.22). This yields

$$a_\mu^{bb,SD}(\text{conn.}) = 0.296(15), \quad (5.7)$$

which we include in our complete result assuming 100% correlation given the shared HISQ ensembles in that work. This is likely a vast overestimate of the true correlation.

For the QED correction to this window observable, we take the estimates of Eqs. (4.24) and (4.25), to which we assign a 100% error, yielding

$$\Delta a_\mu^{SD}(\text{QED}) = 0.028(28) \times 10^{-10}. \quad (5.8)$$

B. Intermediate-distance window observables

Our final determinations for the individual contributions to $a_\mu^{\text{HVP,LO}}$, in the intermediate-distance window, are

$$a_\mu^{ll,W}(\text{conn.}) = 207.06(17)(63)[66] \times 10^{-10}, \quad (5.9)$$

TABLE IX. Approximate absolute error budgets (in units of 10^{-10}) for the uncertainties reported in Eqs. (5.9)–(5.14).

Contribution	stat.	$a \rightarrow 0, \Delta_{\text{TB}}$	$\Delta_{\text{FV}}, \Delta_{M\pi}$	w_0 (fm), w_0/a	Z_V	m_u/m_d	Total
$a_\mu^{ll, \text{W}}$ (conn.)	0.17	0.28	0.33	0.44	0.17	—	0.66
$a_\mu^{ss, \text{W}}$ (conn.)	0.02	0.03	—	0.17	0.04	—	0.18
$a_\mu^{cc, \text{W}}$ (conn.)	0.000	0.032	—	0.058	0.007	—	0.066
a_μ^{W} (disc.)	0.07	0.18	0.03	0.00	0.00	—	0.20
$\Delta a_\mu^{ud, \text{W}}$ (SIB, conn.)	0.09	0.08	0.12	0.00	0.03	0.02	0.17
$\Delta a_\mu^{ud, \text{W}}$ (SIB, disc.)	0.015	0.017	—	0.004	0.000	—	0.023

$$a_\mu^{ss, \text{W}}(\text{conn.}) = 27.16(2)(18)[18] \times 10^{-10}, \quad (5.10)$$

$$a_\mu^{cc, \text{W}}(\text{conn.}) = 2.679(0)(66)[66] \times 10^{-10}, \quad (5.11)$$

$$a_\mu^{\text{W}}(\text{disc.}) = -0.88(7)(18)[20] \times 10^{-10}, \quad (5.12)$$

$$\Delta a_\mu^{ud, \text{W}}(\text{SIB, conn.}) = 0.73(9)(15)[17] \times 10^{-10}, \quad (5.13)$$

$$\Delta a_\mu^{ud, \text{W}}(\text{SIB, disc.}) = -0.183(15)(18)[23] \times 10^{-10}. \quad (5.14)$$

The respective error budgets for these contributions are given in Table IX. We compare these results with previous determinations in Figs. 25 and 26. We obtain $a_\mu^{ll, \text{W}}(\text{conn.})$ with a relative error of 0.32%, a significant improvement over our previous result’s 0.5% precision [12]. Our previous leading uncertainty, from the continuum limit, is decreased from 0.34% \rightarrow 0.12%. This significant improvement is a result of the introduction of a second vector-current discretization and a finer lattice spacing at 0.04 fm. For similar reasons, our uncertainty from Monte-Carlo statistics is decreased by 0.19% \rightarrow 0.09%. Our scale-setting procedures have not changed since our earlier work [12], so the uncertainty from this source is unchanged, 0.21%, and is now leading. Likewise, the systematic uncertainty from the finite-volume correction is largely unchanged as it is determined through the same approach. In Fig. 25, we observe complete consistency with our previous determination as well all the other lattice determinations [8–11, 13, 14, 19, 104]. However, our calculation of $a_\mu^{ll, \text{W}}(\text{conn.})$ differs from the data-driven evaluation of Ref. [102] by 6.2σ .

For the heavy-flavor contributions, $a_\mu^{ss, \text{W}}(\text{conn.})$ and $a_\mu^{cc, \text{W}}(\text{conn.})$, we find the uncertainties, as broken down in Table IX, are dominated by scale-setting, specifically the value of w_0 in physical units. For $a_\mu^{ss, \text{W}}(\text{conn.})$, we find consistency with all previous determinations, except for some slight tension with the Mainz/CLS 22 result [11]. For $a_\mu^{cc, \text{W}}(\text{conn.})$, we see some tension with the most recent determinations of this quantity, while we observe good agreement with the BMW 21 result. Discretization errors are a significant source of uncertainty in our calculation of $a_\mu^{cc, \text{W}}(\text{conn.})$, and we plan to update our calculation by including data at $a \approx 0.04$ fm, which will allow us to test and refine our continuum extrapolations.

Our evaluation of the disconnected contribution to a_μ^{W} , given in Eq. (5.12), is consistent with all previous determinations (right of Fig. 25) albeit with a larger error than the most recent determinations. We find the systematic uncertainty due to variations in continuum extrapolations completely dominates all other uncertainty sources. This calculation includes data at lattice spacings $a \gtrsim 0.09$ fm, and we expect that adding data from $a \approx 0.06$ fm ensemble would yield a significant reduction in the uncertainty.

For the strong-isospin breaking corrections to a_μ^{W} , we obtain a result for the connected

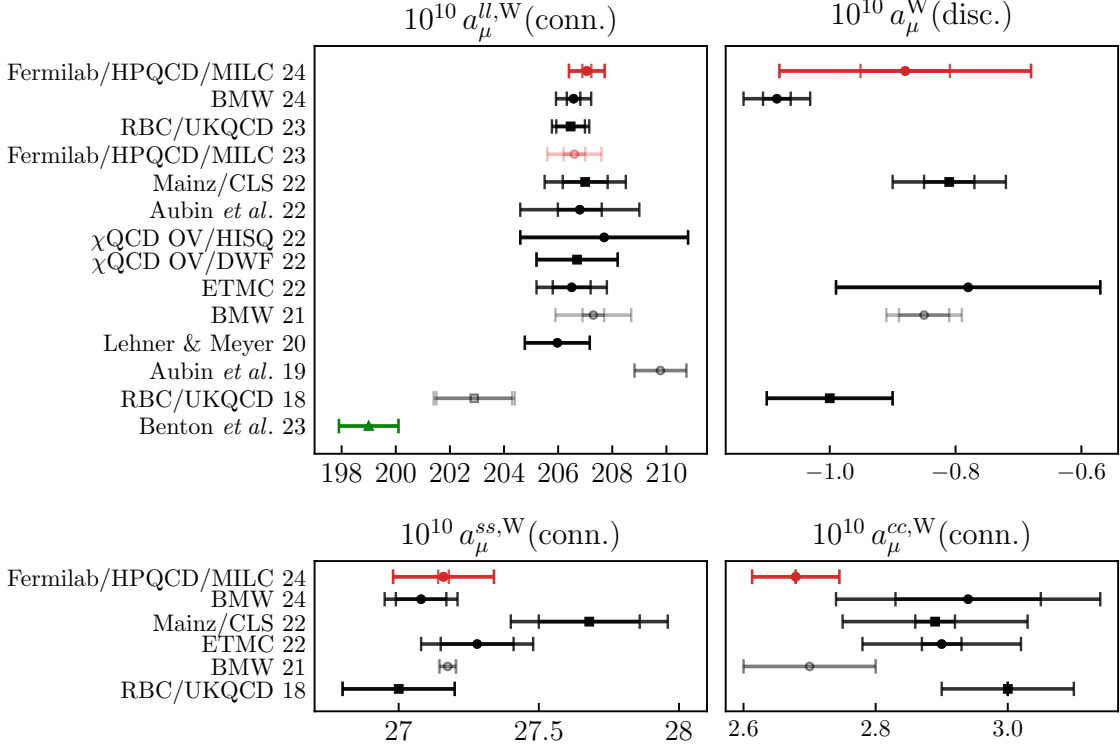


FIG. 25. Comparison of our lattice determinations for $a_\mu^{ll,W}(\text{conn.})$, $a_\mu^W(\text{disc.})$, $a_\mu^{ss,W}(\text{conn.})$, and $a_\mu^{cc,W}(\text{conn.})$ (red circles) labeled “Fermilab/HPQCD/MILC 24” with $n_f = 2 + 1 + 1$ (black circles) and $n_f = 2 + 1$ (black squares) lattice-QCD calculations by BMW 24 [14], RBC/UKQCD 23 [13], Mainz/CLS 22 [11], Aubin *et al.* 22 [9], χ QCD 22 [19], ETMC 22 [10] and Lehner & Meyer 20 [104]. Our previous result, Fermilab/HPQCD/MILC 23, is shown in light red. BMW 21 [8], Aubin *et al.* 19 [65] and RBC/UKQCD 18 [18], shown in gray, have been superseded. The inner error bar shown for our result is from Monte Carlo statistics. Also shown is a data-driven evaluation of $a_\mu^{ll,W}(\text{conn.})$ using e^+e^- cross section data (green triangle) by Benton *et al.* 23 [102, 105].

contribution, Eq. (5.13), that is consistent with the single previous result from BMW 21 (Fig. 26 bottom right), albeit with larger errors. For the disconnected contribution, Eq. (5.14), we see some tension with the BMW result (bottom left). We do find the combination of the two contributions is consistent with BMW 21 while being in mild tension with the RBC/UKQCD 18 estimate (top of Fig. 26).

For the bottom-quark connected contribution to the intermediate window observable, $a_\mu^{bb,W}(\text{conn.})$, which is almost negligible at our current level of precision, we use the perturbative estimate from Eq. (4.22). We assign a 100% error to account for the tensions found in Sec. IV E stemming from the quark-mass scheme in pQCD, yielding

$$a_\mu^{bb,W}(\text{conn.}) = 0.004(4). \quad (5.15)$$

Our ongoing, direct lattice-QCD calculation of the QED corrections to a_μ^W will be presented in a separate paper. Meanwhile, we consider inputs from phenomenology and comparisons of previous lattice-QCD calculations [8, 11, 18, 102, 106, 107] to provide an estimate of $\Delta a_\mu^W(\text{QED})$. The phenomenological estimate in Ref. [106] uses a data-driven

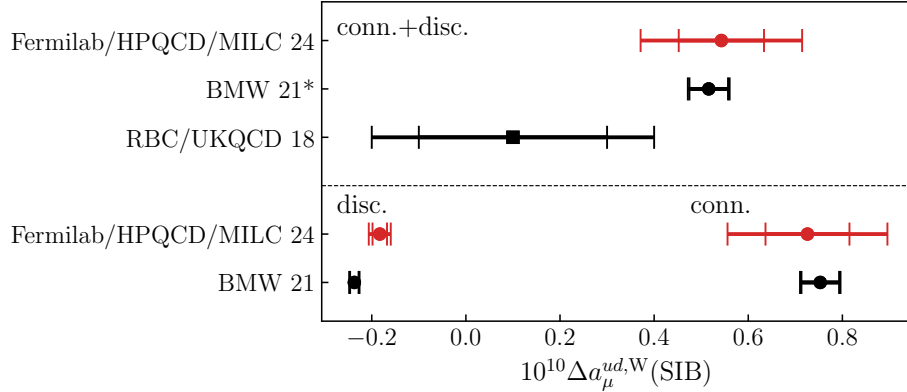


FIG. 26. Comparison of our lattice determinations of $\Delta a_\mu^{ud,W}(\text{SIB, conn.})$ and $\Delta a_\mu^{ud,W}(\text{SIB, disc.})$ (red circles) labeled “Fermilab/HPQCD/MILC 24” with $n_f = 2+1$ (black squares) and $n_f = 2+1+1$ (black circles) lattice-QCD calculations by RBC/UKQCD 18 [18] and BMW 21 [8], respectively. The “BMW 21*” value is computed assuming the connected and disconnected contributions are uncorrelated. The inner error bars are from Monte Carlo statistics.

evaluation based on exclusive-channel e^+e^- cross section measurements to quote a value of $+2.3(9) \times 10^{-10}$, which can be regarded as a conservative bound on the scale of the effect. The phenomenological analysis of QED and strong-isospin-breaking effects in Ref. [107] is consistent with the lattice-QCD calculations of Refs. [8, 11, 18], where Ref. [107] presented some indications of cancellations between QED and strong-isospin-breaking effects. Coupled with the expectation that QED effects are expected to be smaller in windowed quantities, we allow for a range of $\pm 0.2 \times 10^{-10}$. Following Ref. [107], we do not apply a correction to the central value of $\Delta a_\mu^W(\text{QED})$ and take the above range as the uncertainty, yielding

$$\Delta a_\mu^W(\text{QED}) = 0.0(2) \times 10^{-10}. \quad (5.16)$$

VI. SUMMARY AND OUTLOOK

In this paper, we present complete results for the short- and intermediate-distance window observables a_μ^{SD} and a_μ^W from our ongoing project to compute $a_\mu^{\text{HVP,LO}}$ in lattice QCD at few permille-level precision. The two observables together comprise about 45% of the total HVP. We first compute the individual contributions to these observables, defined in Eqs. (2.6)–(2.8). This includes the contributions from quark-line connected contractions $a_\mu^{ll,\text{SD}}(\text{conn.})$, $a_\mu^{ll,W}(\text{conn.})$, $a_\mu^{ss,\text{SD}}(\text{conn.})$, $a_\mu^{ss,W}(\text{conn.})$, $a_\mu^{cc,\text{SD}}(\text{conn.})$, $a_\mu^{cc,W}(\text{conn.})$; quark-line-disconnected contractions $a_\mu^{\text{SD}}(\text{disc.})$, $a_\mu^W(\text{disc.})$; and isospin-breaking corrections $\Delta a_\mu^{ud,\text{SD}}(\text{SIB})$, and $\Delta a_\mu^{ud,W}(\text{SIB})$. Each contribution is obtained at the physical point and in the continuum and infinite volume limits, after a comprehensive systematic error analysis which employs BMA to obtain the total statistical and systematic uncertainties as well as estimates of the approximate breakdown of the error budgets. Our final results for the individual contributions to the short- and intermediate-distance observables are summarized in Eqs. (5.1)–(5.6) and Eqs. (5.9)–(5.14), respectively. The bottom-quark connected and QED contributions are not computed directly in this work. Instead, we use a mix of previous lattice QCD results and phenomenological estimates to obtain the results listed in

TABLE X. Approximate relative error budgets (in %) for the total a_μ^{SD} and a_μ^{W} .

Contrib. stat.	$a \rightarrow 0, \Delta_{\text{TB}}$	$\Delta_{\text{FV}}, \Delta_{M_\pi}$	w_0 (fm), w_0/a	Z_V	$a_\mu^{bb}(\text{conn.})$	$\Delta a_\mu(\text{QED})$	m_u/m_d	Total
δa_μ^{SD}	0.02	0.22	—	0.15	0.15	0.02	0.04	0.31
δa_μ^{W}	0.09	0.14	0.15	0.31	0.10	0.00	0.09	0.41

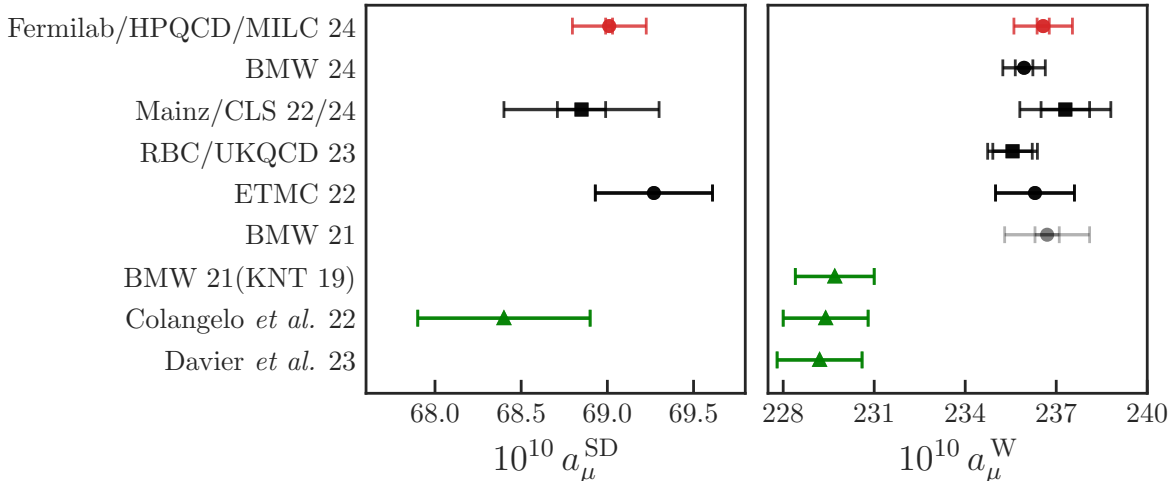


FIG. 27. Comparison of our lattice determination of the total a_μ^{SD} and a_μ^{W} (red circles) labeled “Fermilab/HPQCD/MILC 24” with $n_f = 2 + 1 + 1$ (black circles) and $n_f = 2 + 1$ (black squares) lattice-QCD calculations by BMW 24 [14], Mainz/CLS 22/24 [11, 103], RBC/UKQCD 23 [13] (W only) and ETMC 22 [10]. The previous a_μ^{W} result of BMW 21 [8] is shown in gray. Also shown are data-driven evaluations of a_μ^{SD} and a_μ^{W} using e^+e^- cross section data (green triangles) by Colangelo *et al.* 22 [108], BMW 21 (using the KNT19 dataset) [8], and Davier *et al.* 23 [109].

Eqs. (5.7) and (5.8) and Eqs. (5.15) and (5.16), respectively. Finally, we employ a generalized BMA procedure (see Appendix C) to compute the statistical and systematic correlations between the individual contributions listed in Tables XII and XIII. Summing up the individual contributions with these correlations, we obtain the following results for the complete determinations of a_μ^{SD} and a_μ^{W} , respectively:

$$a_\mu^{\text{SD}} = 69.01(2)(21)[21] \times 10^{-10} \quad a_\mu^{\text{W}} = 236.57(20)(94)[96] \times 10^{-10}. \quad (6.1)$$

The approximate systematic error breakdown for each observable is shown in Table X. With a relative uncertainty of 0.31%, our calculation of a_μ^{SD} is the most precise to date. Our a_μ^{W} result includes an updated calculation of the light-quark connected contribution ($a_\mu^{ll, \text{W}}(\text{conn.})$), which is significantly more precise than our previous result [12], thanks to including correlation function data at a lattice spacing of $a \approx 0.04$ fm, the finest to date, as well as improved statistics and the addition of a second vector-current discretization. Compared with all other lattice-QCD calculations, it also currently has the smallest statistical uncertainty.

As illustrated in Fig. 27, our a_μ^{SD} and a_μ^{W} results are in good agreement with previous lattice-QCD calculations [8, 10, 11, 13, 14, 103]. This can also be seen in the detailed comparisons between our and previous results for the individual a_μ^{SD} (a_μ^{W}) contributions shown in Fig. 24 (Figs. 25 and 26). We note that the sum of a_μ^{SD} and a_μ^{W} in Eq. (6.1) is consistent with the evaluation in Ref. [40] of the one-sided window observable $a_\mu^{\text{win}_1(1,0.15)}$

(see Eq. (2.9a)). A more detailed comparison, which will include the correlations between window observables, will be given in our companion paper on the long-distance contribution to HVP.

Comparing our results with the (pre-2023) data-driven evaluations of Ref. [108], also shown in Fig. 27, we see that our a_μ^{SD} determination is consistent with Ref. [108] at 1.1σ , while our a_μ^{W} result differs from Ref. [108] by 4.2σ . These observations are in line with similar comparisons shown in Refs. [8, 10, 13, 14, 102, 105, 109, 110], and indicate that the difference between lattice QCD and (pre-2023) data-driven evaluations stems from the low-energy region, which is dominated by the two-pion channel in the data-driven method or, correspondingly, by the light-quark-connected contribution in lattice-QCD calculations. This is also where the new cross section measurement by the CMD-3 collaboration [7] disagrees with the measurements included in the pre-2023 KNT19 [111] and DHMZ19 [112] compilations. The CMD-3 measurement of the two-pion cross section implies a higher value for a_μ^{W} that is compatible with lattice-QCD determinations [14, 102, 105]. To gain further insights from such comparisons, it is important first to understand or resolve the differences between the experimental measurements.

Our calculation of a_μ^{SD} benefits from the fact that the local vector-current used to generate the connected correlation functions is protected from log-enhanced contributions (see Appendix A), enabling precise control over continuum-limit extrapolations. Still, as can be seen in the error budgets for a_μ^{SD} in Tables VIII and X, continuum limit extrapolations are the dominant source of uncertainty, where $a_\mu^{\text{cc,SD}}(\text{conn.})$ contributes the largest error. We note that the strange- and charm-connected contributions are computed on ensembles with lattice-spacings $a \gtrsim 0.06$ fm. We are in the process of generating strange- and charm-connected correlation functions on the ensemble at the finest lattice spacing of $a \approx 0.04$ fm, which will refine our calculation of the corresponding contributions.

Examining the systematic error budgets for a_μ^{W} in Tables IX and X, we see that the dominant sources of uncertainty are due to scale setting and finite-volume corrections, while the uncertainties due to continuum extrapolations are significant, but currently sub-leading for all contributions, except for $a_\mu^{\text{W}}(\text{disc.})$. These are also dominant or important sources of error in the long-distance window observables, and will be addressed in our ongoing and planned computations. In particular, we note that the disconnected contributions are computed on ensembles with lattice-spacings $a \gtrsim 0.09$ fm. We plan to extend this analysis to a finer lattice spacing of $a \approx 0.06$ fm. We are in the process of computing the Ω -baryon mass [113] on the MILC HISQ ensembles, which we expect to yield a determination of the scale in physical units with reduced uncertainty. This is a key component in our calculations of the long-distance and full window observables, which are more sensitive to the scale setting uncertainty. A companion paper describing our calculation of the light-quark connected contribution to a_μ^{LD} and $a_\mu^{\text{HVP,LO}}$ is in progress.

At 3.1‰ and 4.1‰, respectively, our results for the total a_μ^{SD} and a_μ^{W} are already close to our precision goal for $a_\mu^{\text{HVP,LO}}$. However, considerable exascale computing resources are needed to reach this precision for the full $a_\mu^{\text{HVP,LO}}$. In particular, we plan to continue to generate correlation functions on our finest ensemble ($a \approx 0.04$ fm) to complete the data set. This will improve statistical and systematic errors (due to discretization errors) for all observables. The finite-volume corrections will be quantified more precisely in a direct finite-volume study, for which we are analyzing a new gauge-field ensemble with a spatial extent of $L = 11$ fm at a lattice spacing of $a \approx 0.09$ fm.

We note that the a_μ^{SD} and a_μ^{W} results presented here rely on phenomenological estimates

of the QED corrections. The results from our ongoing direct lattice-QCD calculation are deferred to a separate paper. While this calculation uses quenched QED, we are also working on computations of the disconnected and sea-quark QED corrections, which make use of our LMA set-up (see Sec. II C). In general, less is known about the QED corrections [8, 11, 18] compared with other contributions, especially in the long-distance region. While their contributions to $a_\mu^{\text{HVP,LO}}$ are small, they are relevant at the desired few permille precision level.

Finally, the well-known signal-to-noise problem is a limiting factor specific to HVP observables at long Euclidean time distances. Here, a recent pilot study [114] showed that spectral reconstructions of the vector current correlation function at large Euclidean times obtained from direct computation of the two-pion contributions can address this problem also for the case of staggered fermions. We plan to extend this study to finer lattice spacings, where the statistical gains will have a larger impact on the continuum extrapolated results.

ACKNOWLEDGMENTS

We thank Claude Bernard, Urs Heller, Paul Mackenzie, Bob Sugar, and Doug Toussaint for their scientific leadership and collaboration. In particular, we are grateful to Bob and Paul for their tireless efforts to obtain computational resources, to Claude for guidance on chiral perturbation theory, to Doug for his invaluable expertise in creating so many of our gauge-field ensembles, and to Urs for essential contributions to previous projects that formed the basis for this work. Computations for this work were carried out in part with computing and long-term storage resources provided by the USQCD Collaboration, the National Energy Research Scientific Computing Center (Cori), the Argonne Leadership Computing Facility (Mira) under the INCITE program, and the Oak Ridge Leadership Computing Facility (Summit) under the Innovative and Novel Computational Impact on Theory and Experiment (INCITE) and the ASCR Leadership Computing Challenge (ALCC) programs, which are funded by the Office of Science of the U.S. Department of Energy. This work used the Extreme Science and Engineering Discovery Environment (XSEDE) supercomputer Stampede 2 at the Texas Advanced Computing Center (TACC) through allocation TG-MCA93S002. The XSEDE program is supported by the National Science Foundation under grant number ACI-1548562. Computations on the Big Red II+, Big Red 3, and Big Red 200 supercomputers were supported in part by Lilly Endowment, Inc., through its support for the Indiana University Pervasive Technology Institute. The parallel file system employed by Big Red II+ was supported by the National Science Foundation under Grant No. CNS-0521433. This work utilized the RMACC Summit supercomputer, which is supported by the National Science Foundation (awards ACI-1532235 and ACI-1532236), the University of Colorado Boulder, and Colorado State University. The Summit supercomputer is a joint effort of the University of Colorado Boulder and Colorado State University. Some of the computations were done using the Blue Waters sustained-petascale computer, which was supported by the National Science Foundation (awards OCI-0725070 and ACI-1238993) and the state of Illinois. Blue Waters was a joint effort of the University of Illinois at Urbana-Champaign and its National Center for Supercomputing Applications. We also used the Cambridge Service for Data Driven Discovery (CSD3), part of which is operated by the University of Cambridge Research Computing Service on behalf of the Science and Technology Facilities Council (STFC) DiRAC HPC Facility. The DiRAC component of CSD3 was funded by BEIS capital funding via STFC capital grants ST/P002307/1 and

ST/R002452/1 and STFC operations grant ST/R00689X/1.

This work was supported in part by the U.S. Department of Energy, Office of Science, under Awards No. DE-SC0010005 (E.T.N. and J.W.S.), No. DE-SC0010120 (S.G.), No. DE-SC0015655 (A.X.K., S.L., M.L., A.T.L.), the “High Energy Physics Computing Traineeship for Lattice Gauge Theory” No. DE-SC0024053 (J.W.S.), and the Funding Opportunity Announcement Scientific Discovery through Advanced Computing: High Energy Physics, LAB 22-2580 (D.A.C., L.H., M.L., S.L.); by the Exascale Computing Project (17-SC-20-SC), a collaborative effort of the U.S. Department of Energy Office of Science and the National Nuclear Security Administration (H.J.); by the National Science Foundation under Grants Nos. PHY20-13064 and PHY23-10571 (C.D., D.A.C., S.L., A.V.), PHY23-09946 (A.B., C.T.P.), and Grant No. 2139536 for Characteristic Science Applications for the Leadership Class Computing Facility (L.H., H.J.) by the Simons Foundation under their Simons Fellows in Theoretical Physics program (A.X.K.); by the Universities Research Association Visiting Scholarship awards 20-S-12 and 21-S-05 (S.L.); by MICIU/AEI/10.13039/501100011033 and FEDER (EU) under Grant PID2022-140440NB-C21 (E.G.); by Consejería de Universidad, Investigación e Innovación and Gobierno de España and EU – NextGenerationEU, under Grant AST22 8.4 (E.G.); by AEI (Spain) under Grant No. RYC2020-030244-I / AEI / 10.13039/501100011033 (A.V.); and by U.K. Science and Technology Facilities Council under Grant ST/T000945/1 (C.T.H.D). A.X.K. is grateful to the Pauli Center for Theoretical Studies and the ETH Zürich for support and hospitality. This document was prepared by the Fermilab Lattice, HPQCD, and MILC Collaborations using the resources of the Fermi National Accelerator Laboratory (Fermilab), a U.S. Department of Energy, Office of Science, HEP User Facility. Fermilab is managed by Fermi Research Alliance, LLC (FRA), acting under Contract No. DE-AC02-07CH11359.

Appendix A: Discretization effects at short-distances

Discretization effects in the short-distance window—and therefore in any window starting at $t = 0$ —require a careful examination, because they explicitly include the first few time slices in $C(t)$. For $a \ll t$ still, the Symanzik effective theory suggests [10, 81–83]

$$C_{\text{lat}}(t) = C(t) \left[1 + b_2 \frac{a^2}{t^2} + \dots \right]. \quad (\text{A1})$$

If t is shorter than any hadronic or quark Compton wavelength, the correlator behaves as $C(t) \sim t^{-3}$ (by power counting), so the lattice artifact term has enhanced sensitivity to short times.

For present purposes, it is enough to consider a sharp cutoff on the window,

$$a_{\mu \text{ lat}}^{\text{SD}} = 4\alpha^2 \int_a^T \tilde{K}(t) C_{\text{lat}}(t) dt. \quad (\text{A2})$$

At short times, the QED kernel $\tilde{K} \sim t^4$, so in the end

$$a_{\mu \text{ lat}}^{\text{SD}} - a_{\mu}^{\text{SD}} \sim b_2 a^2 \log(T/a), \quad (\text{A3})$$

while the omitted terms (in this simple argument) are all of order a^2 .

This feature can be made more concrete by working out the lowest-order contribution to the vector-vector correlator in perturbation theory,

$$C_V(t) = N_c a^3 \frac{1}{3} \sum_i \sum_{\mathbf{x}} V_i(\mathbf{x}) S(\mathbf{x}, 0) V_i(0) S(0, \mathbf{y}), \quad (\text{A4})$$

where N_c is the number of colors (3), $x = (\mathbf{x}, t)$, V_i is the vector current, and the position-space quark propagator $S(x, y)$ is obtained by Fourier transforming in the time variable. Below, the combination

$$\Sigma_4[C_V] = a \sum_{t/a=0}^{\infty} t^4 C_V(t) \quad (\text{A5})$$

is evaluated for unimproved [115, 116] and improved staggered fermions [117], the latter being relevant to the asqtad and HISQ actions.

The details are tedious, so we do not show the full calculation but build up the result in steps. The correlator is obtained by writing the quark propagator as a function of (t, \mathbf{p}) , sewing two propagators together, and using the sum over \mathbf{x} (integration over d^3x in the continuum) to set the three-momentum of the two quarks equal and opposite. The first step picks up poles in the propagator, and the second is just a trace over Dirac matrices. In the continuum, the result is

$$C_V(t) = N_c \int \frac{d^3p}{(2\pi)^3} \frac{e^{-2|t|E}}{E^2} (m_0^2 + \frac{1}{3}\mathbf{p}^2 + E^2), \quad (\text{A6})$$

where $E^2 = m_0^2 + \mathbf{p}^2$. It is possible to simplify this expression further, but it is written this way as a reminder of terms coming from the mass, γ_i , and γ_0 terms in the numerators of the quark propagators. The time dependence is isolated, so it is convenient to integrate over time first,

$$\int_0^{\infty} t^4 e^{-2tE} dt = \frac{3}{4E^5}, \quad (\text{A7})$$

and then integrate over d^3p to obtain $\Sigma_4[C_V]$.

With staggered quarks, a similar structure emerges albeit with several technical changes. The momentum integration is over the half-Brioullin zone, $\mathcal{B}_0 = \{\mathbf{p} | -\pi/2 \leq p_i a < \pi/2\}$, as a consequence of how a Dirac-matrix structure emerges in momentum space [118]. Because of doubling, if there is a pole at $p_0 = iE$, there is also one at $p_0 = iE + \pi$, leading to an oscillating contribution multiplying $(-1)^{|t|/a}$. The relation between energy and momentum is more complicated, and in the integrand $\sinh Ea$ and $\sin p_i a$ appear. The result for the *local* current is

$$C_V(t) = 4N_c \int_{\mathcal{B}_0} \frac{d^3p}{(2\pi)^3} \frac{a^2 e^{-2|t|E}}{\cosh^2(Ea) \sinh^2(Ea)} [m_0^2 + \frac{1}{3}\mathbf{S}^2 + \sinh^2(Ea)/a^2 + (-1)^{|t|/a} (m_0^2 + \frac{1}{3}\mathbf{S}^2 - \sinh^2(Ea)/a^2)], \quad (\text{A8})$$

where $aS_i(p) = \sin(p_i a)$, $\sinh^2(Ea) = a^2(\mathbf{S}^2 + m_0^2)$ comes from finding the pole, and the factor of 4 corresponds to the four tastes in the loop. Note how the structure is similar to Eq. (A6) while the sign of the energy term in the oscillating contribution changes. The *one-link* current is the same except that m_0^2 and $\sinh^2(Ea)$ are multiplied by $\frac{1}{3} \sum_i \cos(p_i a)^2 = 1 - \frac{1}{3}a^2\mathbf{S}^2$, and $a^2\frac{1}{3}[2\sum_i S_i^4 - (\mathbf{S}^2)^2]$ is added to $\frac{1}{3}\mathbf{S}^2$.

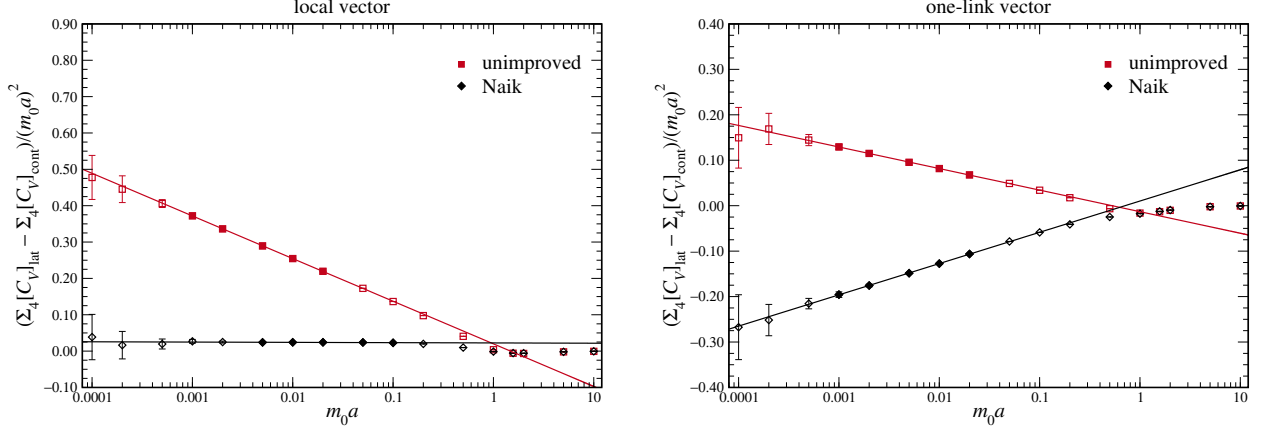


FIG. 28. Lattice artifact versus $m_0 a$ for the local (left) and one-link (right) vector correlator. Red points show the unimproved action and black, the Naik-improved case. The solid points are fit to the form $d + b \log m_0 a$, yielding the lines. The approximate equality of unimproved and improved results for $m_0 a > 1$ is not understood but also not important.

For improved staggered actions (asqtad and HISQ), the propagator has three poles in the upper half plane with real part close to zero, another three in the upper half plane with real part close to π , and then complex conjugate poles in the lower half plane. They solve

$$\sinh(Ea) \left[1 - \frac{1}{6} \sinh^2(Ea)\right] = a \widetilde{\mathcal{S}h}(\mathbf{p}) \equiv a \left[\widetilde{\mathcal{S}}^2(\mathbf{p}) + m_0^2\right]^{1/2}, \quad (\text{A9})$$

where $a \widetilde{\mathcal{S}}_i(\mathbf{p}) = \sin(p_i a) \left[1 + \frac{1}{6} \sin^2(p_i a)\right]$. As in any solution to a cubic equation, the expressions for the energies, which can be labeled 0, +, and -, involve (hyper)trigonometric functions and their inverses. The most notable feature here is that the residue of one of the solutions, -, has opposite sign from the other two. The result for the *local* current is then

$$C_V(t) = 4N_c \sum_{r,s} \int_{\mathcal{B}_0} \frac{d^3 p}{(2\pi)^3} \frac{e^{-|t|(E_r + E_s)}}{\widetilde{\mathcal{C}h}_r \widetilde{\mathcal{C}h}_s \widetilde{\mathcal{S}h}} \left[s_r s_s m_0^2 + \frac{1}{3} s_r s_s \widetilde{\mathcal{S}}^2 + \widetilde{\mathcal{S}h}^2 + e^{i\pi t/a} \left(s_r s_s m_0^2 + \frac{1}{3} s_r s_s \widetilde{\mathcal{S}}^2 - \widetilde{\mathcal{S}h}^2 \right) \right], \quad (\text{A10})$$

where r, s range over 0, +, -, $\widetilde{\mathcal{C}h}_r = \cosh(E_r a) \left[1 - \frac{1}{2} \sinh^2(E_r a)\right]$, and $s_- = -1$ while the others are +1. The *one-link* current is the same except that m_0^2 and $\widetilde{\mathcal{S}h}^2$ are multiplied by $\frac{1}{3} \sum_i \cos(p_i a)^2 = 1 - \frac{1}{3} a^2 \mathcal{S}^2$, and $a^2 \frac{1}{3} \left(2 \sum_i S_i^2 \widetilde{\mathcal{S}}_i^2 - \mathcal{S}^2 \widetilde{\mathcal{S}}^2\right)$ is added to $\frac{1}{3} \widetilde{\mathcal{S}}^2$.

In Eqs. (A8) and (A10), the time dependence is again isolated. Summing the exponentials over t yields

$$a \sum_{t/a=0}^{\infty} t^4 e^{-2tE} = a^5 \frac{\cosh(Ea) \left\{1 + \frac{1}{2} \cosh^2(Ea)\right\}}{2 \sinh^5(Ea)}, \quad (\text{A11})$$

$$a \sum_{t/a=0}^{\infty} t^4 e^{-2tE} (-1)^{t/a} = a^5 \frac{\sinh(Ea) \left\{1 - \frac{1}{2} \sinh^2(Ea)\right\}}{2 \cosh^5(Ea)}. \quad (\text{A12})$$

The right-hand sides differ from the continuum by terms of order a^6 .

Combining Eqs. (A11) and (A12) with Eqs. (A8) and (A10) and dividing by 4 provides $\Sigma_4[C_V]_{\text{lat}}$, while combining Eq. (A7) with Eq. (A6) provides $\Sigma_4[C_V]_{\text{cont}}$. Figure 28 shows the quantities

$$\frac{1}{(m_0 a)^2} (\Sigma_4[C_J]_{\text{lat}} - \Sigma_4[C_J]_{\text{cont}}) \quad (\text{A13})$$

for the local (left) and one-link (right) vector correlators. This quantity is designed to behave as $d + b \log m_0 a$ as $a \rightarrow 0$, so a log-enhanced discretization effect appears as a significant slope on a log-linear plot. Such effects are clearly present for the unimproved local current and the one-link current in any case. The Naik term clearly removes the log-enhancement for the local current: the slope b is much smaller than for the other cases and consistent with zero.

Appendix B: Oscillating contributions in the short-distance window

Correlation functions constructed from staggered-quark operators, which are local in time, contain temporal oscillations from states of opposite parity. In the case at hand, the oscillating states are 1^{+-} states, which are heavier than the 1^{--} states, so their contribution to the correlator dies out after a few timeslices. This is observed in the $a_\mu^{\text{HVP,LO}}$ integrands for the different connected contributions we compute in this work; see Fig. 1. Depending on the relative sizes of the oscillating and non-oscillating states' energies and their couplings to the local-time staggered-quark operator, the oscillations can be quite pronounced relative to the size of the correlation function. In particular, we observe the charm integrand in Fig. 1 to have much larger relative oscillation sizes than the light or strange. The oscillating contribution to the integrand and hence a_μ is, however, a discretization effect, with the expectation that contribution in the continuum limit is zero.

In Ref. [12], we examined this expectation for the case of a_μ^{W} and $a_\mu^{\text{W}2} = a_\mu^{\text{win}_2(1.5,1.9,0.15)}$. Our analysis procedure to remove the oscillating contribution involved fitting the light-quark connected correlation functions in the respective window regions. These fits then enabled a high-precision, high-fidelity reconstruction of the correlation function. Using the reconstruction, the observables were then computed with and without the oscillating contribution. In that work, we found a non-zero correlated difference for a_μ^{W} between the oscillating and non-oscillating result on our coarsest two ensembles. On our two finest ensembles, the difference was statistically zero. We also found that the difference approached zero faster than the leading discretization effects in our continuum extrapolation fit function, namely $a^2 \alpha_s$. For $a_\mu^{\text{W}2}$, as expected, we found that the difference was zero on all ensembles, as the oscillating state contributions had largely died off in the later time region. In our final Bayesian model averaged result of Ref. [12], we include model variations of $a_\mu^{\text{HVP,LO}}$ observables computed without the oscillating contribution, which we found to be consistent with the result that included oscillations.

For the short-distance window, it is not sensible to fit the earliest timeslices, so fit reconstructions of $a_\mu^{ll, \text{SD}}(\text{conn.})$, $a_\mu^{ss, \text{SD}}(\text{conn.})$, $a_\mu^{cc, \text{SD}}(\text{conn.})$ cannot be included in the BMA. Instead, we construct a modified version of Eq. (A3) from Ref. [12],

$$C'_{\text{no osc.}}(t) = \begin{cases} \sum_n^{N_{\text{states}}} Z_n^2 e^{-E_n t} & \text{if } t/a > 1, \\ C(t) & \text{if } t/a \leq 1. \end{cases} \quad (\text{B1})$$

TABLE XI. Correlated differences between a_μ observables computed from the raw correlation functions and values computed from the fit reconstruction.

$\approx a$ (fm)	$\Delta a_\mu^{ll,SD}(\text{conn.})$	$\Delta a_\mu^{ss,SD}(\text{conn.})$	$\Delta a_\mu^{cc,SD}(\text{conn.})$
0.15	0.00055(52)	$-7.7(8.9) \times 10^{-8}$	$7(12) \times 10^{-10}$
0.12	0.000053(56)	$-9(10) \times 10^{-8}$	$1(13) \times 10^{-10}$
0.09	$-0.000012(56)$	$-0.0006(286)$	$1.8(3.4) \times 10^{-8}$
0.06	$4(34) \times 10^{-6}$	$4.9(7.0) \times 10^{-6}$	$-3.7(4.2) \times 10^{-8}$
0.04	$-0.0018(60)$		$-0(15) \times 10^{-5}$
0.03			0.00007(31)

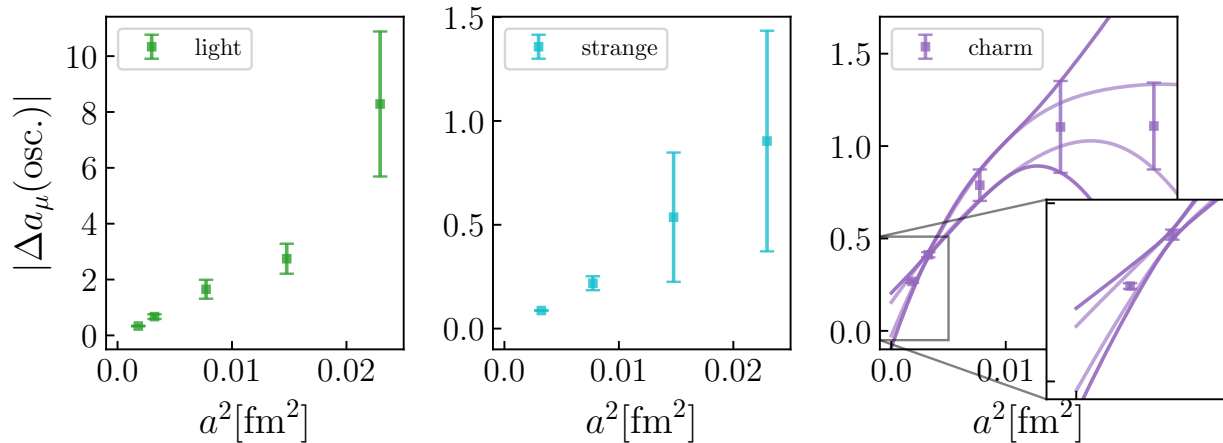


FIG. 29. Plot of the correlated difference $\Delta a_\mu(\text{osc.})$ between a_μ computed from the raw correlation function and the modified non-oscillating correlation function of Eq. (B1) versus a^2 .

The parameters Z_n and E_n come from a fit to the correlator using the Ansätze function in Eq. (A2) of Ref. [12]. We perform these fits for each flavor on all ensembles using $t_{\min}/a = 2$. We choose t_{\max} to be roughly 0.7 fm (the RHS of the SD window boundary plus 2Δ). We use $4 + 4$ states in our fits in all cases, except where increasing(decreasing) the number of non(-oscillating) states gave a smaller correlated difference between a_μ computed from the raw data and a_μ computed from the fit reconstruction with the oscillating contribution. For the light, strange, and charm fits, we select the lowest energy state prior from the PDG values of the ρ , ϕ and J/ψ meson masses, respectively. The other prior selections follow from Ref. [12]. The fit qualities, as measured by the $\chi^2/\text{d.o.f.}$, were all between 0.3 and 1.3. The correlated differences between the a_μ observables constructed from the raw correlator versus the correlator in (A2) in Ref. [12] are given in Table XI. We find that they are all zero within uncertainties, indicating very good reproduction of the raw correlation function from the fit.

The results from plugging

$$\Delta C_{\text{osc}}(t) = C(t) - C'_{\text{no osc.}}(t) \quad (\text{B2})$$

into Eq. (2.9) for the short-distance window to obtain $|\Delta a_\mu(\text{osc.})|$ are shown in Fig. 29 for $a_\mu^{ll,SD}(\text{conn.})$, $a_\mu^{ss,SD}(\text{conn.})$, $a_\mu^{cc,SD}(\text{conn.})$. We emphasize that due to not having a $t/a = 1$

data point with the oscillating contribution, the curvature is reduced relative to the true $\|\Delta a_\mu(\text{osc.})\|$ as it is a larger contribution at coarser spacings. For the light and strange contributions, we observe straightforwardly that the oscillating contribution falls off faster than the leading discretization in our continuum fits. For charm, this is not apparent for the physical ensembles used in this work. To resolve this, we have studied additional charm data generated on non-physical light quark ensembles [61], with lattice spacings of approximately 0.04 fm and 0.03 fm. With this extended dataset, we observe the oscillating contribution does indeed fall faster than the leading discretization terms in our continuum fit.

Appendix C: Covariance and Bayesian model averaging

Here we derive the formulas used to estimate covariance between different observables in the context of BMA. We follow the notation of Ref. [84]. This derivation is a simple generalization of the formula for the variance derived in that reference. Our derivation of the BMA statistical covariance matches a similar result from Ref. [109], which was not used in full in that analysis due to computational cost. To our knowledge, this is the first account of BMA systematic covariance due to shared use of EFT and EFT-inspired models across observables appearing in the literature.

We consider two observables a and b , which are specified over a joint space of N_M models $\{M_i\}$. The sample estimator of covariance between these two quantities is defined as

$$\text{Cov}[a, b] = \langle ab \rangle - \langle a \rangle \langle b \rangle, \quad (\text{C1})$$

where $\langle \dots \rangle$ denotes the expectation over the posterior distribution. Each expectation value can be expanded out as a weighted average over the space of models [84]:

$$\text{Cov}[a, b] = \sum_{i=1}^{N_M} \langle ab \rangle_i \text{pr}(M_i|D) - \sum_{i=1}^{N_M} \sum_{j=1}^{N_M} \langle a \rangle_i \langle b \rangle_j \text{pr}(M_i|D) \text{pr}(M_j|D), \quad (\text{C2})$$

where $\text{pr}(M_i|D)$ are the model weights as defined in Sec. III, and the expectation $\langle a \rangle_i$ denotes the expectation with respect to the specific model M_i . Next, we manipulate this formula to expose the individual model covariances $\text{Cov}_i[a, b]$ with respect to each model M_i :

$$\begin{aligned} \text{Cov}[a, b] &= \sum_{i=1}^{N_M} (\langle ab \rangle_i - \langle a \rangle_i \langle b \rangle_i) \text{pr}(M_i|D) \\ &\quad + \sum_{i=1}^{N_M} \langle a \rangle_i \langle b \rangle_i \text{pr}(M_i|D) - \sum_{i=1}^{N_M} \sum_{j=1}^{N_M} \langle a \rangle_i \langle b \rangle_j \text{pr}(M_i|D) \text{pr}(M_j|D) \end{aligned} \quad (\text{C3})$$

$$= \sum_{i=1}^{N_M} \text{Cov}_i[a, b] \text{pr}(M_i|D) + \sum_{i=1}^{N_M} \langle a \rangle_i \langle b \rangle_i \text{pr}(M_i|D) - \langle a \rangle \langle b \rangle. \quad (\text{C4})$$

Similar to the analogous formula for the variance, the first term represents a weighted average of the “statistical covariance” between a and b within each of the models, while the second two terms together encode a “systematic covariance” over the space of models. Note that the “statistical covariance” also includes correlations from the use of shared parameters (*e.g.*, w_0 (fm), w_0/a , Z_V).

The formula in Eq. (C4) is fully general, but in the present context we are mainly interested in using it for the combination of different components of a_μ . Since these components are produced in independent analyses, estimating the joint probability distribution $\text{pr}(M_i|D)$ across the model spaces for multiple observables is impractical, even via global bootstrap. To simplify the calculation, we assume the model spaces for different observables are independent as a first approximation. As shown in Appendix C1, this assumption is equivalent to neglecting the BMA systematic covariance but allows for the full determination of the statistical (and parametric) covariance. In Appendix C2, we revisit the systematic covariance and provide a conservative estimate for the primary source of systematic correlations in this analysis, namely that from shared EFT and EFT-inspired finite volume models.

1. Statistical covariance

Consider the case where the joint model space $\{M_i\}$ decomposes into the direct product of $\{M_m^A\}$ and $\{M_n^B\}$, where the models in $\{M_m^A\}$ are used only to determine a and likewise for $\{M_n^B\}$ and b . To be explicit, a (b) is specified over a space of N_{MA} (N_{MB}) models in $\{M_m^A\}$ ($\{M_n^B\}$), and thus there are $N_M = N_{MA}N_{MB}$ joint models in $\{M_i\} = \{M_{m_i}^A\} \times \{M_{n_i}^B\}$. The double subscripts on “ m_i ” and “ n_i ” denote the two models chosen from $\{M_m^A\}$ and $\{M_n^B\}$ which together comprise the joint model M_i ; note that multiple copies of each model from M_m^A or M_n^B appear in the joint space N_{MB} and N_{MA} times, respectively.

Now assume the models in each space are independent. With this assumption, the model weights defined on $\{M_i\}$ factorize into those defined on each set of models $\{M_{m_i}^A\}$ and $\{M_{n_i}^B\}$, *i.e.*,

$$\text{pr}(M_i|D) = \text{pr}(M_{m_i}^A|D) \text{pr}(M_{n_i}^B|D). \quad (\text{C5})$$

Using the fact that a depends only on models in $\{M_m^A\}$ and similarly for b and $\{M_n^B\}$, it is straightforward to show that in this case, the “systematic covariance” terms in Eq. (C4) cancel exactly, and we are left with a simple average over statistical covariances:

$$\text{Cov}^{\text{stat}}[a, b] = \sum_{m=1}^{N_{MA}} \sum_{n=1}^{N_{MB}} \text{Cov}_{mn}[a, b] \text{pr}(M_m^A|D) \text{pr}(M_n^B|D). \quad (\text{C6})$$

The individual model weights for M_m^A and M_n^B are estimated using the BAIC within each separate analysis, while the statistical covariances are estimated using bootstrap, as described in the text.

2. Systematic covariance

Model independence, which leads to zero model-systematic covariance, is a reasonable assumption for most sources of systematic error between most observables; however, the shared use of EFT and EFT-inspired models among different observables may violate this assumption and lead to non-negligible systematic correlation between these observables. Correlations associated with M_π corrections are negligible since Δ_{M_π} is small in any case where these corrections are applied. TB corrections do not lead to correlations as they are used only in the final results for one observable, namely $a_\mu^{\text{W}}(\text{disc.})$. In contrast, FV corrections do lead to large systematic errors in multiple observables. Here, we derive a

TABLE XII. Correlation matrix for the individual contributions computed in this work in the short-distance window SD.

	$a_\mu^{ll}(\text{conn.})$	$a_\mu^{ss}(\text{conn.})$	$a_\mu^{cc}(\text{conn.})$	$a_\mu(\text{disc.})$	$\Delta a_\mu^{ud}(\text{SIB, conn.})$	$\Delta a_\mu^{ud}(\text{SIB, disc.})$
$a_\mu^{ll}(\text{conn.})$	1.00	0.09	-0.05	-0.09	0.00	-0.00
$a_\mu^{ss}(\text{conn.})$	0.09	1.00	0.26	0.13	-0.03	0.01
$a_\mu^{cc}(\text{conn.})$	-0.05	0.26	1.00	0.30	-0.01	0.01
$a_\mu(\text{disc.})$	-0.09	0.13	0.30	1.00	-0.01	0.03
$\Delta a_\mu^{ud}(\text{SIB, conn.})$	0.00	-0.03	-0.01	-0.01	1.00	0.00
$\Delta a_\mu^{ud}(\text{SIB, disc.})$	0.00	0.01	0.01	0.03	0.00	1.00

conservative upper bound on the systematic covariance associated with the shared use of model-based FV corrections.

As in Appendix C1, assume the two observables a and b come from different sets of models. As argued above, the systematic covariance of interest entirely consists of that which comes from FV corrections, *i.e.*,

$$\text{Cov}^{\text{sys}}[a, b] = \text{Cov}^{\text{FV}}[a, b]. \quad (\text{C7})$$

In the current context, this covariance cannot be determined exactly as the joint model probabilities $\text{pr}(M_i|D)$ are too cumbersome to compute. Recall, however, that the covariance matrix is diagonally dominant, which means

$$|\text{Cov}^{\text{FV}}[a, b]| \leq \sigma_a^{\text{FV}} \sigma_b^{\text{FV}}, \quad (\text{C8})$$

where the variances are evaluated in the usual way including appropriate factors of the model weights in each subset,

$$\sigma_a^{\text{FV}} = \sqrt{\sum_{k=1}^{N_{S_{\text{FV}}^A}} \langle a \rangle_{S_{\text{FV},k}^A}^2 \text{pr}(S_{\text{FV},k}^A|D) - \langle a \rangle_{\text{FV}}^2}, \quad (\text{C9})$$

with $\text{pr}(S_{\text{FV},k}^A|D)$ as defined in Eq. (3.13) and

$$\langle a \rangle_{\text{FV}} = \sum_{k=1}^{N_{S_{\text{FV}}^A}} \langle a \rangle_{S_{\text{FV},k}^A} \text{pr}(S_{\text{FV},k}^A|D), \quad (\text{C10})$$

$$\langle a \rangle_{S_{\text{FV},k}^A} = \frac{1}{\text{pr}(S_{\text{FV},k}^A|D)} \sum_{M_m^A \in S_{\text{FV},k}^A} \langle a \rangle_m \text{pr}(M_m^A|D), \quad (\text{C11})$$

and similarly for b . For emphasis, the subsets $\{S_{\text{FV},k}^A\}$ partition the model space $\{M_m^A\}$ for a single observable into subsets (one for each FV model), which is distinct from the factorization of the joint model space for two observables as $\{M_i\} = \{M_{m_i}^A\} \times \{M_{n_i}^B\}$. Note that in most cases $\langle a \rangle_{\text{FV}} = \langle a \rangle$ as defined in Eq. (3.10); the only exception is for $a_\mu^{\text{W}}(\text{disc.})$, where we average only over the variations without TB corrections, to disentangle these two effects.

TABLE XIII. Correlation matrix for the individual contributions computed in this work in the intermediate-distance window W.

	$a_\mu^{ll}(\text{conn.})$	$a_\mu^{ss}(\text{conn.})$	$a_\mu^{cc}(\text{conn.})$	$a_\mu(\text{disc.})$	$\Delta a_\mu^{ud}(\text{SIB, conn.})$	$\Delta a_\mu^{ud}(\text{SIB, disc.})$
$a_\mu^{ll}(\text{conn.})$	1.00	0.63	0.59	0.09	0.32	0.10
$a_\mu^{ss}(\text{conn.})$	0.63	1.00	0.86	0.05	0.00	0.16
$a_\mu^{cc}(\text{conn.})$	0.59	0.86	1.00	0.05	0.00	0.15
$a_\mu(\text{disc.})$	0.09	0.05	0.05	1.00	0.08	0.08
$\Delta a_\mu^{ud}(\text{SIB, conn.})$	0.32	0.00	0.00	0.08	1.00	0.01
$\Delta a_\mu^{ud}(\text{SIB, disc.})$	0.10	0.16	0.15	0.08	0.01	1.00

In summary, what we have shown is

$$\text{Cov}[a, b] = \text{Cov}^{\text{stat}}[a, b] + \text{Cov}^{\text{syst}}[a, b] \quad (\text{C12})$$

$$= \text{Cov}^{\text{stat}}[a, b] + \text{Cov}^{\text{FV}}[a, b] \quad (\text{C13})$$

$$\leq \text{Cov}^{\text{stat}}[a, b] + |\text{Cov}^{\text{FV}}[a, b]| \quad (\text{C14})$$

$$\leq \text{Cov}^{\text{stat}}[a, b] + \sigma_a^{\text{FV}} \sigma_b^{\text{FV}}. \quad (\text{C15})$$

$\text{Cov}^{\text{stat}}[a, b]$ is as defined in Eq. (C6), and the additional term is used to account for the systematic correlations between $a_\mu^{ll, W}(\text{conn.})$, $a_\mu^W(\text{disc.})$, and $\Delta a_\mu^{ud, W}(\text{SIB, conn.})$. We conservatively assume that the covariance between our observables saturates this bound; this can be thought of as equivalent to assuming 100% correlation between observables for the systematic error due to FV model variation.

3. Correlation matrices

Using this formalism, our correlation matrices for the SD and W windows are given in Tables XII and XIII, respectively.

-
- [1] B. Abi *et al.* (Muon $g - 2$), *Phys. Rev. Lett.* **126**, 141801 (2021), [arXiv:2104.03281 \[hep-ex\]](#).
 - [2] D. P. Aguillard *et al.* (Muon $g - 2$), *Phys. Rev. Lett.* **131**, 161802 (2023), [arXiv:2308.06230 \[hep-ex\]](#).
 - [3] M. Abe *et al.*, *PTEP* **2019**, 053C02 (2019).
 - [4] J-PARC muon $g - 2$ /EDM experiment, <https://g-2.kek.jp/>.
 - [5] T. Aoyama *et al.*, *Phys. Rept.* **887**, 1 (2020), [arXiv:2006.04822 \[hep-ph\]](#).
 - [6] G. Colangelo *et al.*, in *Snowmass 2021*, edited by M. Peskin (2022) [arXiv:2203.15810 \[hep-ph\]](#).
 - [7] F. V. Ignatov *et al.* (CMD-3), *Phys. Rev. D* **109**, 112002 (2024), [arXiv:2302.08834 \[hep-ex\]](#).
 - [8] S. Borsanyi *et al.* (BMW), *Nature* **593**, 51 (2021), [arXiv:2002.12347 \[hep-lat\]](#).
 - [9] C. Aubin, T. Blum, M. Golterman, and S. Peris, *Phys. Rev. D* **106**, 054503 (2022), [arXiv:2204.12256 \[hep-lat\]](#).
 - [10] C. Alexandrou *et al.* (Extended Twisted Mass), *Phys. Rev. D* **107**, 074506 (2023), [arXiv:2206.15084 \[hep-lat\]](#).

- [11] M. Cè *et al.*, *Phys. Rev. D* **106**, 114502 (2022), [arXiv:2206.06582 \[hep-lat\]](#).
- [12] A. Bazavov *et al.* (Fermilab Lattice, HPQCD, MILC), *Phys. Rev. D* **107**, 114514 (2023), [arXiv:2301.08274 \[hep-lat\]](#).
- [13] T. Blum *et al.* (RBC, UKQCD), *Phys. Rev. D* **108**, 054507 (2023), [arXiv:2301.08696 \[hep-lat\]](#).
- [14] A. Boccaletti *et al.*, (2024), [arXiv:2407.10913 \[hep-lat\]](#).
- [15] T. Blum *et al.* (RBC, UKQCD), [arXiv:2410.20590 \[hep-lat\]](#) (2024).
- [16] S. Spiegel and C. Lehner, [arXiv:2410.17053 \[hep-lat\]](#) (2024).
- [17] D. Bernecker and H. B. Meyer, *Eur. Phys. J. A* **47**, 148 (2011), [arXiv:1107.4388 \[hep-lat\]](#).
- [18] T. Blum, P. A. Boyle, V. Gülpers, T. Izubuchi, L. Jin, C. Jung, A. Jüttner, C. Lehner, A. Portelli, and J. T. Tsang (RBC, UKQCD), *Phys. Rev. Lett.* **121**, 022003 (2018), [arXiv:1801.07224 \[hep-lat\]](#).
- [19] G. Wang, T. Draper, K.-F. Liu, and Y.-B. Yang (χ QCD), [arXiv:2204.01280 \[hep-lat\]](#) (2022).
- [20] T. Blum, *Phys. Rev. Lett.* **91**, 052001 (2003), [arXiv:hep-lat/0212018](#).
- [21] A. Kurz, T. Liu, P. Marquard, and M. Steinhauser, *Phys. Lett. B* **734**, 144 (2014).
- [22] E. Balzani, S. Laporta, and M. Passera, *Phys. Lett. B* **834**, 137462 (2022), [arXiv:2112.05704 \[hep-ph\]](#).
- [23] E. Balzani, S. Laporta, and M. Passera, *Phys. Lett. B* **858**, 139040 (2024), [arXiv:2406.17940 \[hep-ph\]](#).
- [24] A. V. Nesterenko, *J. Phys. G* **49**, 055001 (2022), [Addendum: *J.Phys.G* 50, 029401 (2022)], [arXiv:2112.05009 \[hep-ph\]](#).
- [25] B. Chakraborty, C. T. H. Davies, J. Koponen, G. P. Lepage, and R. S. Van de Water (Fermilab Lattice, HPQCD, MILC), *Phys. Rev. D* **98**, 094503 (2018), [arXiv:1806.08190 \[hep-lat\]](#).
- [26] C. Aubin *et al.* (HPQCD, MILC), *Phys. Rev. D* **70**, 031504 (2004), [arXiv:hep-lat/0405022](#).
- [27] C. Aubin, C. Bernard, C. E. DeTar, J. Osborn, S. Gottlieb, E. B. Gregory, D. Toussaint, U. M. Heller, J. E. Hetrick, and R. Sugar (MILC), *Phys. Rev. D* **70**, 114501 (2004), [arXiv:hep-lat/0407028](#).
- [28] A. Bazavov *et al.* (Fermilab Lattice, MILC), *Phys. Rev. D* **90**, 074509 (2014), [arXiv:1407.3772 \[hep-lat\]](#).
- [29] C. Patrignani *et al.* (Particle Data Group), *Chin. Phys. C* **40**, 100001 (2016).
- [30] S. Navas *et al.* (Particle Data Group), *Phys. Rev. D* **110**, 030001 (2024).
- [31] A. Bazavov *et al.* (Fermilab Lattice, MILC), *Phys. Rev. D* **98**, 074512 (2018), [arXiv:1712.09262 \[hep-lat\]](#).
- [32] Y. Aoki *et al.* (Flavour Lattice Averaging Group (FLAG)), [arXiv:2411.04268 \[hep-lat\]](#) (2024).
- [33] M. Gell-Mann, R. J. Oakes, and B. Renner, *Phys. Rev.* **175**, 2195 (1968).
- [34] S. Basak *et al.* (MILC), *Phys. Rev. D* **99**, 034503 (2019), [arXiv:1807.05556 \[hep-lat\]](#).
- [35] Y. Aoki *et al.* (Flavour Lattice Averaging Group), *Eur. Phys. J. C* **82**, 869 (2022), [arXiv:2111.09849 \[hep-lat\]](#).
- [36] S. Borsanyi *et al.* (BMW), *JHEP* **09** (2012), 010, [arXiv:1203.4469 \[hep-lat\]](#).
- [37] A. Bazavov *et al.*, *PoS LATTICE2023*, 292 (2024), [arXiv:2401.06522 \[hep-lat\]](#).
- [38] R. J. Dowdall, C. T. H. Davies, G. P. Lepage, and C. McNeile (HPQCD), *Phys. Rev. D* **88**, 074504 (2013), [arXiv:1303.1670 \[hep-lat\]](#).
- [39] C. T. H. Davies *et al.* (Fermilab Lattice, HPQCD, MILC), *Phys. Rev. D* **101**, 034512 (2020), [arXiv:1902.04223 \[hep-lat\]](#).
- [40] A. Bazavov *et al.* (Fermilab Lattice, MILC), *Phys. Rev. D* **107**, 094516 (2023), [arXiv:2212.12648 \[hep-lat\]](#).

- [41] E. Follana, Q. Mason, C. Davies, K. Hornbostel, G. P. Lepage, J. Shigemitsu, H. Trotter, and K. Wong (HPQCD), *Phys. Rev. D* **75**, 054502 (2007), [arXiv:hep-lat/0610092](#).
- [42] K. Symanzik, *Nucl. Phys. B* **226**, 205 (1983).
- [43] M. Lüscher and P. Weisz, *Commun. Math. Phys.* **97**, 59 (1985), [Erratum: *Commun. Math. Phys.* **98**, 433 (1985)].
- [44] M. Lüscher and P. Weisz, *Phys. Lett. B* **158**, 250 (1985).
- [45] M. G. Alford, W. Dimm, G. P. Lepage, G. Hockney, and P. B. Mackenzie, *Phys. Lett. B* **361**, 87 (1995), [arXiv:hep-lat/9507010](#).
- [46] A. Hart, G. M. von Hippel, and R. R. Horgan (HPQCD), *Phys. Rev. D* **79**, 074008 (2009), [arXiv:0812.0503 \[hep-lat\]](#).
- [47] G. P. Lepage and P. B. Mackenzie, *Phys. Rev. D* **48**, 2250 (1993), [arXiv:hep-lat/9209022](#).
- [48] A. Bazavov *et al.* (MILC), *Phys. Rev. D* **82**, 074501 (2010), [arXiv:1004.0342 \[hep-lat\]](#).
- [49] A. Bazavov *et al.* (MILC), *Phys. Rev. D* **87**, 054505 (2013).
- [50] N. Miller *et al.*, *Phys. Rev. D* **103**, 054511 (2021), [arXiv:2011.12166 \[hep-lat\]](#).
- [51] B. Chakraborty *et al.* (Fermilab Lattice, HPQCD, MILC), *Phys. Rev. Lett.* **120**, 152001 (2018), [arXiv:1710.11212 \[hep-lat\]](#).
- [52] B. Chakraborty, C. T. H. Davies, G. C. Donald, J. Koponen, and G. P. Lepage (HPQCD), *Phys. Rev. D* **96**, 074502 (2017), [arXiv:1703.05552 \[hep-lat\]](#).
- [53] D. Hatton, C. T. H. Davies, G. P. Lepage, and A. T. Lytle (HPQCD), *Phys. Rev. D* **100**, 114513 (2019), [arXiv:1909.00756 \[hep-lat\]](#).
- [54] S. Collins, G. Bali, and A. Schäfer, *PoS LATTICE2007*, 141 (2007), [arXiv:0709.3217 \[hep-lat\]](#).
- [55] G. S. Bali, S. Collins, and A. Schäfer, *Comput. Phys. Commun.* **181**, 1570 (2010), [arXiv:0910.3970 \[hep-lat\]](#).
- [56] T. A. DeGrand and S. Schaefer, *Comput. Phys. Commun.* **159**, 185 (2004), [arXiv:hep-lat/0401011](#).
- [57] L. Giusti, P. Hernandez, M. Laine, P. Weisz, and H. Wittig, *JHEP* **04** (2004), 013, [arXiv:hep-lat/0402002](#).
- [58] T. Blum, T. Izubuchi, and E. Shintani, *Phys. Rev. D* **88**, 094503 (2013), [arXiv:1208.4349 \[hep-lat\]](#).
- [59] S. Yamamoto, C. DeTar, A. X. El-Khadra, C. McNeile, R. S. Van de Water, and A. Vaquero (Fermilab Lattice, HPQCD, MILC), *PoS LATTICE2018*, 322 (2019).
- [60] S. Yamamoto, *Computation of the Quark-line Disconnected Part of the Hadronic Vacuum Polarization of the Muon*, *Ph.D. thesis*, The University of Utah (2019).
- [61] D. Hatton, C. T. H. Davies, B. Galloway, J. Koponen, G. P. Lepage, and A. T. Lytle (HPQCD), *Phys. Rev. D* **102**, 054511 (2020), [arXiv:2005.01845 \[hep-lat\]](#).
- [62] C. Aubin, T. Blum, P. Chau, M. Golterman, S. Peris, and C. Tu, *Phys. Rev. D* **93**, 054508 (2016), [arXiv:1512.07555 \[hep-lat\]](#).
- [63] J. Bijnens and J. Releforts, *JHEP* **12** (2017), 114, [arXiv:1710.04479 \[hep-lat\]](#).
- [64] C. Aubin, T. Blum, M. Golterman, and S. Peris, *Phys. Rev. D* **102**, 094511 (2020), [arXiv:2008.03809 \[hep-lat\]](#).
- [65] C. Aubin, T. Blum, C. Tu, M. Golterman, C. Jung, and S. Peris, *Phys. Rev. D* **101**, 014503 (2020), [arXiv:1905.09307 \[hep-lat\]](#).
- [66] B. Chakraborty, C. T. H. Davies, P. G. de Oliveira, J. Koponen, G. P. Lepage, and R. S. Van de Water (HPQCD), *Phys. Rev. D* **96**, 034516 (2017), [arXiv:1601.03071 \[hep-lat\]](#).
- [67] G. J. Gounaris and J. J. Sakurai, *Phys. Rev. Lett.* **21**, 244 (1968).

- [68] M. Lüscher, *Nucl. Phys. B* **364**, 237 (1991).
- [69] M. Lüscher, *Nucl. Phys. B* **354**, 531 (1991).
- [70] L. Lellouch and M. Lüscher, *Commun. Math. Phys.* **219**, 31 (2001), [arXiv:hep-lat/0003023](#).
- [71] C. J. D. Lin, G. Martinelli, C. T. Sachrajda, and M. Testa, *Nucl. Phys. B* **619**, 467 (2001), [arXiv:hep-lat/0104006](#).
- [72] H. B. Meyer, *Phys. Rev. Lett.* **107**, 072002 (2011), [arXiv:1105.1892 \[hep-lat\]](#).
- [73] A. Francis, B. Jäger, H. B. Meyer, and H. Wittig, *Phys. Rev. D* **88**, 054502 (2013), [arXiv:1306.2532 \[hep-lat\]](#).
- [74] M. Della Morte, A. Francis, V. Gülpers, G. Herdoíza, G. von Hippel, H. Horch, B. Jäger, H. B. Meyer, A. Nyffeler, and H. Wittig, *JHEP* **10** (2017), 020, [arXiv:1705.01775 \[hep-lat\]](#).
- [75] M. T. Hansen and A. Patella, *JHEP* **10** (2020), 029, [arXiv:2004.03935 \[hep-lat\]](#).
- [76] G. P. Lepage *et al.*, *Nucl. Phys. B Proc. Suppl.* **106**, 12 (2002), [arXiv:hep-lat/0110175](#).
- [77] B. Chakraborty *et al.* (HPQCD), *Phys. Rev. D* **91**, 054508 (2015), [arXiv:1408.4169 \[hep-lat\]](#).
- [78] T. Van Ritbergen, J. A. M. Vermaseren, and S. A. Larin, *Phys. Lett. B* **400**, 379 (1997), [arXiv:hep-ph/9701390](#).
- [79] M. Czakon, *Nucl. Phys. B* **710**, 485 (2005), [arXiv:hep-ph/0411261](#).
- [80] M. F. Zoller, *JHEP* **2016**, 118, [arXiv:1608.08982 \[hep-ph\]](#).
- [81] M. Della Morte, R. Sommer, and S. Takeda, *Phys. Lett. B* **672**, 407 (2009), [arXiv:0807.1120 \[hep-lat\]](#).
- [82] M. Cè, T. Harris, H. B. Meyer, A. Toniato, and C. Török, *JHEP* **12**, 215, [arXiv:2106.15293 \[hep-lat\]](#).
- [83] R. Sommer, L. Chimirri, and N. Husung, *PoS LATTICE2022*, 358 (2023), [arXiv:2211.15750 \[hep-lat\]](#).
- [84] W. I. Jay and E. T. Neil, *Phys. Rev. D* **103**, 114502 (2021), [arXiv:2008.01069 \[stat.ME\]](#).
- [85] E. T. Neil and J. W. Sitison, *Phys. Rev. D* **109**, 014510 (2024), [arXiv:2208.14983 \[stat.ME\]](#).
- [86] S. Borsanyi *et al.* (BMW), *Science* **347**, 1452 (2015), [arXiv:1406.4088 \[hep-lat\]](#).
- [87] E. Berkowitz *et al.*, [arXiv:1704.01114 \[hep-lat\]](#) (2017).
- [88] C. C. Chang *et al.*, *Nature* **558**, 91 (2018), [arXiv:1805.12130 \[hep-lat\]](#).
- [89] E. T. Neil and J. W. Sitison, *Phys. Rev. E* **108**, 045308 (2023), [arXiv:2305.19417 \[stat.ME\]](#).
- [90] K. A. Bollen and R. A. Stine, *Sociological Methods & Research* **21**, 205 (1992), <https://doi.org/10.1177/0049124192021002004>.
- [91] G. Lepage, C. Gohlke, and D. Hackett, [gplepage/gvar v11.10](#) (2022).
- [92] A. Bazavov *et al.* (Fermilab Lattice, MILC), *Phys. Rev. D* **93**, 113016 (2016), [arXiv:1602.03560 \[hep-lat\]](#).
- [93] M. Golterman, K. Maltman, and S. Peris, *Phys. Rev. D* **95**, 074509 (2017), [arXiv:1701.08685 \[hep-lat\]](#).
- [94] M. Golterman, K. Maltman, and S. Peris, *EPJ Web Conf.* **175**, 06010 (2018), [arXiv:1710.10512 \[hep-lat\]](#).
- [95] R. V. Harlander and M. Steinhauser, *Comput. Phys. Commun.* **153**, 244 (2003), [arXiv:hep-ph/0212294](#).
- [96] S. Borsanyi *et al.* (Budapest-Marseille-Wuppertal), *Phys. Rev. Lett.* **121**, 022002 (2018), [arXiv:1711.04980 \[hep-lat\]](#).
- [97] K. G. Chetyrkin and A. Maier, *Nucl. Phys. B* **844**, 266 (2011), [arXiv:1010.1145 \[hep-ph\]](#).
- [98] E. C. Poggio, H. R. Quinn, and S. Weinberg, *Phys. Rev. D* **13**, 1958 (1976).
- [99] W. Melnitchouk, R. Ent, and C. Keppel, *Phys. Rept.* **406**, 127 (2005), [arXiv:hep-ph/0501217](#).
- [100] A. Bazavov *et al.* (Fermilab Lattice, MILC, TUMQCD), *Phys. Rev. D* **98**, 054517 (2018).

- [101] D. Hatton, C. T. H. Davies, J. Koponen, G. P. Lepage, and A. T. Lytle (HPQCD), *Phys. Rev. D* **103**, 054512 (2021), [arXiv:2101.08103 \[hep-lat\]](#).
- [102] G. Benton, D. Boito, M. Golterman, A. Keshavarzi, K. Maltman, and S. Peris, [arXiv:2411.06637 \[hep-ph\]](#) (2024).
- [103] S. Kuberski, M. Cè, G. von Hippel, H. B. Meyer, K. Ottnad, A. Risch, and H. Wittig, *JHEP* **03**, 172, [arXiv:2401.11895 \[hep-lat\]](#).
- [104] C. Lehner and A. S. Meyer, *Phys. Rev. D* **101**, 074515 (2020).
- [105] G. Benton, D. Boito, M. Golterman, A. Keshavarzi, K. Maltman, and S. Peris, *Phys. Rev. Lett.* **131**, 251803 (2023), [arXiv:2306.16808 \[hep-ph\]](#).
- [106] M. Hoferichter, G. Colangelo, B.-L. Hoid, B. Kubis, J. R. de Elvira, D. Schuh, D. Stamen, and P. Stoffer, *Phys. Rev. Lett.* **131**, 161905 (2023), [arXiv:2307.02532 \[hep-ph\]](#).
- [107] C. T. H. Davies *et al.* (Fermilab Lattice, MILC, HPQCD), *Phys. Rev. D* **106**, 074509 (2022), [arXiv:2207.04765 \[hep-lat\]](#).
- [108] G. Colangelo, A. X. El-Khadra, M. Hoferichter, A. Keshavarzi, C. Lehner, P. Stoffer, and T. Teubner, *Phys. Lett. B* **833**, 137313 (2022), [arXiv:2205.12963 \[hep-ph\]](#).
- [109] M. Davier, Z. Fodor, A. Gerardin, L. Lellouch, B. Malaescu, F. M. Stokes, K. K. Szabo, B. C. Toth, L. Varnhorst, and Z. Zhang, *Phys. Rev. D* **109**, 076019 (2024), [arXiv:2308.04221 \[hep-ph\]](#).
- [110] G. Benton, D. Boito, M. Golterman, A. Keshavarzi, K. Maltman, and S. Peris, *Phys. Rev. D* **109**, 036010 (2024), [arXiv:2311.09523 \[hep-ph\]](#).
- [111] A. Keshavarzi, D. Nomura, and T. Teubner, *Phys. Rev. D* **101**, 014029 (2020).
- [112] M. Davier, A. Hoecker, B. Malaescu, and Z. Zhang, *Eur. Phys. J. C* **80**, 241 (2020), [Erratum: *Eur. Phys. J. C* **80**, 410 (2020)].
- [113] Y. Lin, A. S. Meyer, C. Hughes, A. S. Kronfeld, J. N. Simone, and A. Strelchenko (Fermilab Lattice), *Phys. Rev. D* **103**, 034501 (2021).
- [114] S. Lahert, C. DeTar, A. X. El-Khadra, S. Gottlieb, A. S. Kronfeld, and R. S. Van de Water, [arXiv:2409.00756 \[hep-lat\]](#) (2024).
- [115] N. Kawamoto and J. Smit, *Nucl. Phys. B* **192**, 100 (1981).
- [116] H. S. Sharatchandra, H. J. Thun, and P. Weisz, *Nucl. Phys. B* **192**, 205 (1981).
- [117] S. Naik, *Nucl. Phys. B* **316**, 238 (1989).
- [118] C. van den Doel and J. Smit, *Nucl. Phys. B* **228**, 122 (1983).